BERGISCHE UNIVERSITÄT WUPPERTAL

Development of Lightweight Support Structures for the ATLAS Detector at the Large Hadron Collider

Dissertation
zur Erlangung des akademischen Grades
Doktor-Ingenieur (Dr.-Ing.)

in der

Fakultät für Maschinenbau und Sicherheitstechnik

der

Bergischen Universität Wuppertal

vorgelegt von

Mukundan Srinivasan

aus Chennai, Indien

Tag der mündlichen Prüfung : 19.12.2016

Die Dissertation kann wie folgt zitiert werden:

urn:nbn:de:hbz:468-20170228-114455-4

[http://nbn-resolving.de/urn/resolver.pl?urn=urn%3Anbn%3Ade%3Ahbz3A468-20170228-114455-2]

Abstract

An investigation towards the development of the novel local support structure of the pixel detector (within the ATLAS* experiment) completely based on carbon is presented. The work involves the investigation of the role of the diamond powder (DP) in enhancing the out of plane thermal conductivity ($K_\perp$), the elastic and the failure behaviour of the composites. Finite element based micromechanical modelling and steady state thermal conductivity measurements were performed and an improvement in the out of plane thermal conductivity by a factor of 2.3 and of 2.8 for the standard modulus and the high modulus carbon fibre composite filled with diamond powder resin were observed. Numerical investigations were performed to predict the elastic properties of the diamond powder enhanced woven composites. The failure behaviour of the diamond powder filled composites were evaluated by the progressive damage modelling technique.

Three new support structure designs (with a length of $750\,\mathrm{mm}$) were developed with a diamond powder enhanced carbon fibre pipe for cooling, out of which two support structure designs namely Iso-Graphite and the Stiffener stave were realistic in terms of production. Finite element modelling for both the designs were performed to evaluate the natural frequencies, heat transfer and deformations by the static and thermomechanical loading. The highlights of both the designs are their reduced material budget. The thermal and the mechanical behaviour were well within the requirements. Prototypes for the Iso-Graphite stave with and without diamond powder filled carbon fibre pipes were developed. Furthermore, the Iso-Graphite stave design was extended for the two innermost detector layers with a length of $1500\,\mathrm{mm}$. The staves of both layers were connected with a stiff composite structure which showed an excellent structural, thermal and thermomechanical behaviour.

---

*ATLAS (A Toroidal LHC ApparatuS) is one of the particle detector experiment constructed at the Large Hadron Collider (LHC) at CERN (the European Organization for Nuclear Research) in Switzerland

Kurzfassung

Die Entwicklung neuartiger Trägerstukturen für den Pixeldetektor, innerhalb des ATLAS Experimentes die ausschließlich aus Kohlefaser bestehen wird in dieser Arbeit dargestellt. Dies beinhaltet unter anderem die Untersuchung der thermischer Leitfähigkeit und welchen Einfluss Diamantpulver auf die elastischen Eigenschaften von Verbundwerkstoffen nehmen kann. Finite Element basierte mikromechanische Modellierung und thermische Leitfähigkeit Untersuchungen durch die Ebene wurde durchgeführt und weiter entwickelt. Bei der thermischen Leitfähigkeit wurde für hoch modulige Fasern eine Steigerung von 2,3 bis 2,8 beobachtet. Nummerische Untersuchungen wurden durchgeführt, damit die elastischen Eigenschaften für gewebte Verbundwerkstoffe prognostiziert werden können. Das Versagensverhalten von Faserverbundwerkstoffen gefüllt mit Diamantpulver wurden mit der progressive damage modelling technique ausgewertet.

Drei unterschiedliche Trägerstrukturen, mit einer Länge von 750mm, wurden entwickelt. In diesen Strukturen ist eine Carbonpipe für die Kühlung verbaut. Die Matrix der Pipe ist mit Diamantpulver angereichert. Zwei der entwickelten Trägerstrukturen, Iso-Graphit und Stiffener Stave, sind aber nur herstellbar. Finite Element Berechnungen wurden für diese Modelle durchgeführt und ausgewertet. Es wurden die Eigenfrequenz, Wärmeleitfähigkeit sowie die Deformation in Bezug auf statische und thermomechanische Belastung durchgeführt. Der Vorteil dieser zwei Strukturen ist die Reduzierung der eingesetzten Masse. Die Vorgegebenen Anforderungen erfüllen beide Strukturen. Prototypen für den Iso-Graphite Stave wurden entwickelt dabei wurden Prototypen mit und ohne Diamantpulver hergestellt. Darüber hinaus wurde das Design auf eine Gesamtlänge auf 1500mm erweitert für die zwei innersten Lagen im Detektor. Die Lagen werden mit einer steifen Verbundstruktur verbunden. Diese zeig hervorragende Eigenschaften in Bezug auf thermische und thermomechanisches Lasten.

Acknowledgements

Contents

List of Abbreviations

Acronyms

ALICE   A Large Ion Collider Experiment

ASTM   American Society for Testing and Materials

ATLAS   A Toroidal LHC ApparatuS

CAD   Computer Aided Design

CB   Carbon Black

CERN   The European Organization for Nuclear Research

CF   Carbon Fibre

CFRP   Carbon Fibre Reinforced Plastic

CLT   Classical Lamination Theory

CMS   Compact Muon Solenoid Experiment

CNFs   Carbon Nanofibres

CNTs   Carbon Nano Tubes

CTE   Coefficient of Thermal Expansion

DP   Diamond Powder

FEM   Finite Element Method

GFRP   Glass Fibre Reinforced Plastic

GNPs   Graphene Nanoparticles

HL-LHC   High Luminosity Large Hadron Collider

IBL   The Insertable B-Layer

LHC   Large Hadron Collider

MP   Mesophase Pitch

MWNTs   Multi Walled Nanotubes

OHT   Open Hole Tension

PAN   Polyacrylonitrile

PBC   Periodic Boundary Conditions

PEEK   Polyether Ether Ketone

PTFE   Polytetrafluoroethylene

RTM   Resin Transfer Moulding

RVE   Representative Volume Element

SCT   Semi-Conductor Tracker

SEM   Scanning Electron Microscopy

SWNTs   Single Walled Nanotubes

T300   Standard Modulus Carbon Fibre

TFM   Thermal Figure of Merit

TRT   Transition Radiation Tracker

VARTM   Vacuum Assisted Resin Transfer Moulding

VGCF	Vapour Grown Carbon Fibre
VGCNFs	Vapour Grown Carbon Nanofibres
YS90A	High Modulus Carbon Fibre

Symbols related to Physics

σ	Cross-Section of the Particle
N	Number of Events
t	Time
L	Luminosity
ϕ	Angle to Measure the Coverage of the Charged Particles
q	Charge
$\boldsymbol{B}$	Magnetic Field
$\boldsymbol{E}$	Electric Field
$\boldsymbol{v}$	Velocity
X/X_0	Total number of radiation length (expressed in %)
O	Beam Axis
R	Barrel Layer Radius
I	Sensor Width
α	Tilt Angle
n	Stave Number on the Layer

Symbols related to Mechanical Engineering

P	Heat Flux or Input Power
ΔT	Temperature Difference
[M]	Mass Matrix
[C]	Damping matrix
[K]	Stiffness matrix
$\{\ddot{u}\}$	Acceleration Vector
$\{\dot{u}\}$	Velocity Vector
$\{u\}$	Displacement Vector
ω	Circular Natural Frequency
$\{\phi\}$	Mode Shape
ρ	Density
$K_\perp$	Out of Plane Thermal Conductivity
Q	Calculated Heat Flux
p_c	Percolation Threshold
p	Total Filler Content

$\langle\sigma\rangle_\Omega$ Volume Average Stress Tensor Field

$\langle\epsilon\rangle_\Omega$ Volume Average Strain Tensor Field

$\langle\sigma\rangle$ Total Averaged Stress Tensor

$\langle\epsilon\rangle$ Total Averaged Strain Tensor

V_m Volume Fraction of the Matrix

V_f Volume Fraction of the Fibre

E Elastic Modulus

G Shear Modulus

ν Poisson Ratio

τ Shear Stress

γ Shear Strain

X_T Tensile Strength in the Fibre Direction

Y_T Tensile Strength in the Transverse Direction

X_C Compressive Strength in the Fibre Direction

Y_C Compressive Strength in the Transverse Direction

G_{IC} Mode I Fracture Toughness

G_{IIC} Mode II Fracture Toughness

σ_n Nominal Stress in the Pure Normal Mode

σ_s Nominal Stress in the First Shear Direction

σ_t Nominal Stress in the Second Shear Direction

σ_{I0} Interlaminar Normal Stresses

σ_{II0} Interlaminar Shear Stresses

1 Introduction

In modern physics, there is no such thing as "nothing", even in perfect vacuum pairs of virtual fundamental particles are constantly being created and destroyed. Though they cannot be directly observed, the effects they create are quite real [1]. The stable material and the atoms, which are the building blocks of everything on Earth consists of Protons, Neutrons and Electrons. Protons and Neutrons are described as composite particles made from quarks [2]; the electron as a quark is fundamental within the so called Standard Model of particle physics. This is a theory (developed since the mid 1960s) of fundamental subatomic particles and their interactions. Since the formulation of the Standard Model, additional fundamental particles like heavy quarks, the heavy tau lepton and its neutrino, the gluon, W and Z bosons and more recently the Higgs boson (genuinely predicted by the Standard Model) were discovered. The Standard Model very precisely describes the known matter and its interactions [2].

Scientists (Astrophysicists) have found that the ordinary matter makes only 4% of the universe. There must be additional dark matter [3] which accounts for 23% of the universe while the remaining 73% account for the dark energy, which is a repulsive energy that drives the galaxies apart [3]. Important questions that remain unclear to the scientific society are the dark matter and the dark energy. Dark matter particles should be massive and therefore do not travel with the speed of light. They seem not to interact with ordinary matter except that they seem to be gravitationally attractive [3]. The deepest puzzles of the particle physics is, that there is no candidate for dark matter particles within the Standard Model of particle physics.

There are furthermore theoretical and conceptual open questions in the Standard Model (like the enormous spread of the particle masses) which await scientific answers. Research towards the dark matter (and others) are the modern day's physics question and an understanding about them is fundamental towards understanding the universe.

The experiments at the Large Hadron Collider (LHC) built at the European Organisation for Nuclear Research (CERN) intend to search for a better understanding of the Standard Model and also for new particles in view of the above mentioned questions. There are, however, challenges. Heavy particles cannot be produced on demand. In high energy interactions, all the particles are produced at random, each with its own probability given by nature.

Considering dimensional reasons, this probability falls of at least as an inverse square of mass. Therefore the heavy particles are rarely produced among an overwhelming background of lighter particles. The only chance is to produce as many events as possible (i.e large luminosity† is needed) and then filter for the interesting heavy particles.

---

†Luminosity (L) measures the ability of an accelerator to produce events.
$L = \frac{1}{\sigma}\frac{dN}{dt}$; L is the ratio of the number of events detected (N) in a certain time (t) to the production cross-section of the particles (σ)

This fact has severe consequences for the experiments. The accelerator (LHC) has to produce as many interactions as possible at highest energy which is what the High Luminosity LHC (HL-LHC) shall provide beyond 2025. In consequence, the total rate of the particles crossing the detector's inner layers is enormous, leading likely to radioactive activation of the material.

The inner detector layers must therefore be made predominantly from light nuclei (like hydrogen, carbon) which are least affected. Another advantage of the light nuclei materials is that, they have a large radiation length[‡]. Therefore they show least electromagnetic interactions with the passing particles thereby disturbing the particle tracks only little and allowing most precise measurements of the particle trajectories.

The detector's support structures must therefore

1. contain least materials as possible,

2. be built from light materials,

3. be precise, reliable for long term operation and capable to withstand high radiation dosage.

Carbon fibre reinforced composite material appears as the choice for the support structure of the innermost detector (within the ATLAS experiment) as it would experience higher particle flow due to its close proximity to the interaction point. The investigation of the material properties and the development of the lightweight local support structures of the pixel detector within the ATLAS experiment which would be operational at the HL-LHC is the objective of this thesis.

[‡]Radiation length is related to the energy loss of high energy-electromagnetic particles interacting with a material.

1.1   The Large Hadron Collider

The Large Hadron Collider (LHC) built by European Organization for Nuclear Research (CERN) aims to test the predictions of different theories of high energy physics and to explore towards supersymmetry, dark matter, dark energy and the physics beyond the Standard Model [4]. The LHC lies in a tunnel 27 km in circumference as deep as 175 metres beneath the Franco-Swiss border near Geneva, Switzerland (Figure 1 §).

FIGURE 1: The Large Hadron Collider (LHC) §

The aim of the collider is to smash protons moving at almost the speed of light into each other and so recreate conditions a tiny fraction of a second after the big bang. During the collisions the kinetic energy is converted to mass, showers from new massive particles are created. The new particles are highly unstable and quickly decay into other particles. Four massive detectors (namely ATLAS, ALICE, CMS, LHCb) placed within the LHC are designed to detect these showers of new particles coming out of the collisions. In 2012, ATLAS and CMS observed the existence of the elusive Higgs boson [5], which is an elementary particle in the Standard Model. It interacts with other particles, thus "slowing" them down and effectively giving them mass [6].

---

§http://people.physics.tamu.edu/kamon/research/refColliders/LHC/LHC_is_back.html

1.2 ATLAS Detector

ATLAS is a general purpose particle physics experiment at the LHC (Figure 2). The experiment is designed to take advantage of the unprecedented energy available at the LHC and observe phenomena that involve highly massive particles. It might shed light on new theories of particle physics beyond the Standard Model.
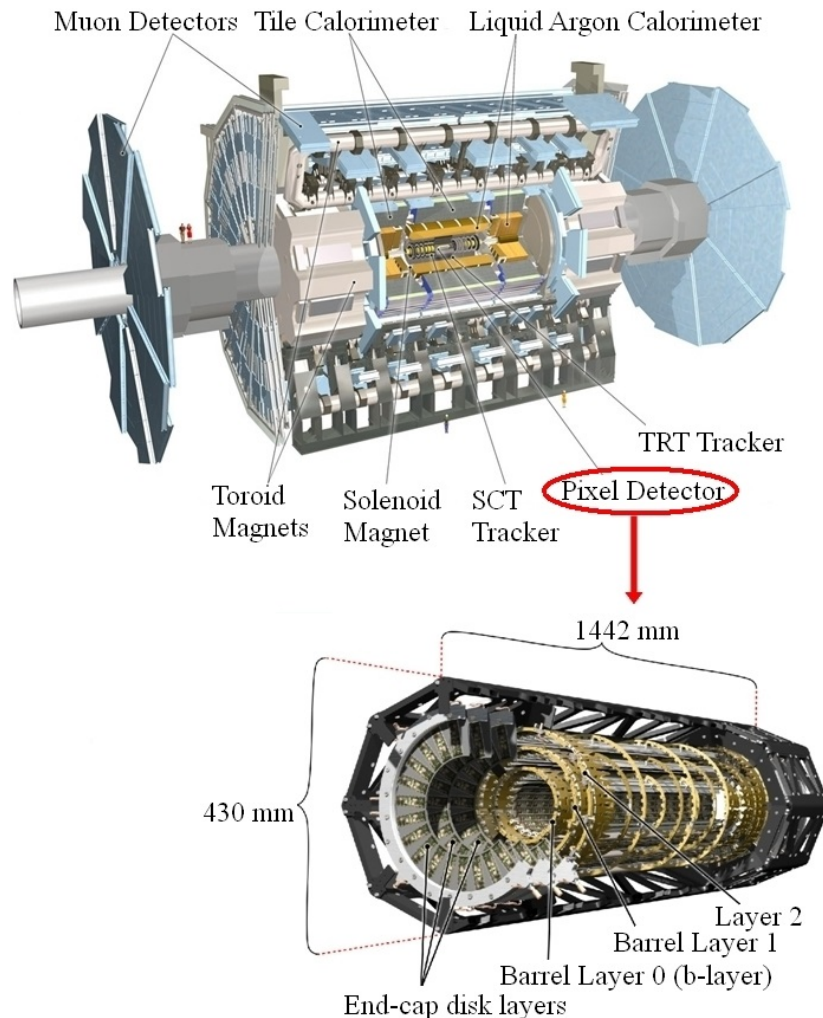
FIGURE 2: Pixel detector within the ATLAS experiment [7]

ATLAS [7] is 46 metres long, 25 metres in diameter, and weighs about 7000 tonnes. It consists of a series of large concentric cylinders (Figure 2) around the interaction point, where the proton beams from the LHC collide. It can be divided into four major parts: the Inner Detector (Pixel, SCT, TRT), the calorimeters, the muon spectrometer and the magnet systems. Each of these is in turn are made of multiple layers. The calorimeters measure the energy of stopped particles, and the muon system makes additional measurements of highly penetrating muons (The muon is a subatomic particle which is unstable with a mean lifetime of only $2.2\,\mu s$). Two magnet systems bend charged particles in the Inner Detector and the Muon Spectrometer, allowing their momenta to be measured [4]. The cylinders are closed by corresponding end covers (caps) in the front and backward regions.

The pixel detector is the innermost part of the ATLAS detector installed in LHC (Figure 2). The basic structure of the detector consists of a barrel section with three coaxial layers of local support structures and two disk sections each containing three disks. Each barrel layer consists of a cylindrical turbine-like sequence of the local support structures (staves) supported on a shell cylinder. The basic function of the pixel detector is to track the charged particles by detecting their interaction with the silicon chip materials at discrete points, revealing information about the particle trajectories and their momenta. When protons of both LHC beams interact in the centre of the detector, different particles with a broad range of energies are produced and then measured by the ATLAS detector. This should allow to reconstruct the properties of any (new) physical process or particle produced in these interactions. An upgrade of ATLAS for the HL-LHC is intended to ensure this capability even with strongly increased particle flux.

1.3   Insertable B-Layer (IBL)

The Insertable B-Layer (IBL) is a sub-detector that has been placed into the centre of ATLAS detector. It is a fourth layer of the pixel detector in between a new smaller beam pipe and the so called inner pixel layer (B-layer)[8]. It has been placed to cope with the increasing performance of the LHC after 2015. IBL is explained in detail in this thesis in order to illustrate the needs of future pixel detectors. Figure 3 [¶] shows the IBL while being installed within the detector where the staves are covered within Kapton® film [‖].
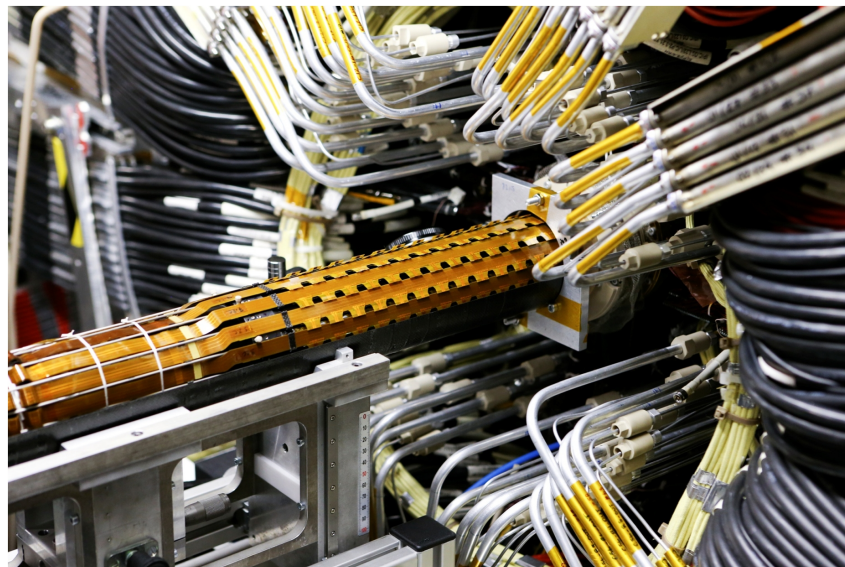
FIGURE 3: Insertable B Layer (IBL) during the installation into the detctor [¶]

[¶]http://home.cern/about/updates/2014/05/new-subdetector-atlas

[‖]Kapton® is a polyimide film developed by DuPont™ has the ability to maintain its excellent physical, electrical, and mechanical properties over a wide temperature range. http://www.dupont.com/content/dam/dupont/products-and-services/membranes-and-films/polyimde-films/documents/DEC-Kapton-summary-of-properties.pdf

The IBL within the detector will maintain the physics performance with increased luminosity. It is the first point of detection of particles produced during high-energy collisions. The principal motivations of the IBL are towards the improvements of tracking robustness, precision and operation under the high radiation environment.

The IBL electronic modules comprise of the actual pixel detector and the corresponding electronics. These parts are bump-bonded and almost homogeneously dissipate heat loss. The IBL local support structure (stave) is approximately 750 mm long (active area). It is designed to support and cool the detector electronics (Pixel detector and chip modules).

The width of the stave is $18.8\,\mathrm{mm}$. This width is considered since each stave will host a double chip module with a single sensor of $20 \times 40\ \mathrm{mm}^2$. The task of the stave is to hold the detector modules in position with high accuracy (precision), minimizing the deformation induced by the cooling. The sensor electronics are mounted on top of a carbon fibre composite laminate called as "Face plate". The electronics produces a relevant amount of heat ($0.7\,\mathrm{W\,cm^{-2}}$). The heat has to be efficiently dissipated in order to keep the pixel sensors at a temperature below $0°\mathrm{C}$ needed to minimize the radiation damage.

An evaporative CO_2 boiling system to remove the power dissipated by the sensors is incorporated in the support (Figure 4). This must be done with lightweight materials having a large radiation length so that the distortion of the tracks of charged particles is reduced. Different materials used within the stave are shown in Figure 4. Carbon fibre reinforced composite laminate called "Omega" is glued on the bottom of the stave for adding stiffness and stability.
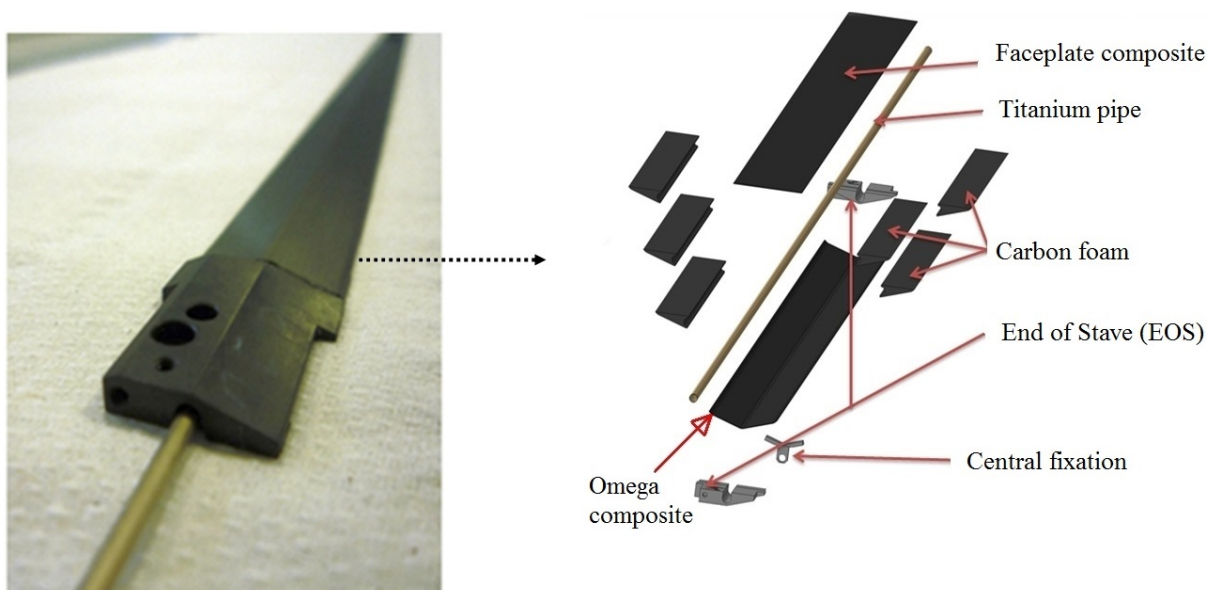
FIGURE 4: Different materials within the stave [8]

The thermal contact is made through highly thermal conductive light carbon foam in order to maintain the sensor temperature sufficiently low. This limits the leakage currents in the silicon and hence the thermal run-away. The stave's cooling is provided by the titanium pipe which is robust in terms of thermal performance and tightness towards leakage and pressure.

The cooling pipe has to withstand a maximum design pressure of $150\,\mathrm{bar}$. The manufacturing procedures of the IBL stave are shown in Figure 5, where the prepreg unidirectional carbon fibre composite (K13C/RS3) with a layup of $[0/90/0]$ are used for producing the face plate and the omega. Titanium pipes with an outer diameter of $1.7\,\mathrm{mm}$ and an inner diameter of $1.5\,\mathrm{mm}$ are used.

Six blocks of carbon foam are machined. The end block which works as the end of the stave for fixation and positioning are made with carbon fibre enhanced PEEK material. The same material is used for building the central fixation (central support). The foam blocks, the titanium pipe and the omega are assembled together after which the foam blocks are milled. The face plate and the central support are then glued to the structure.
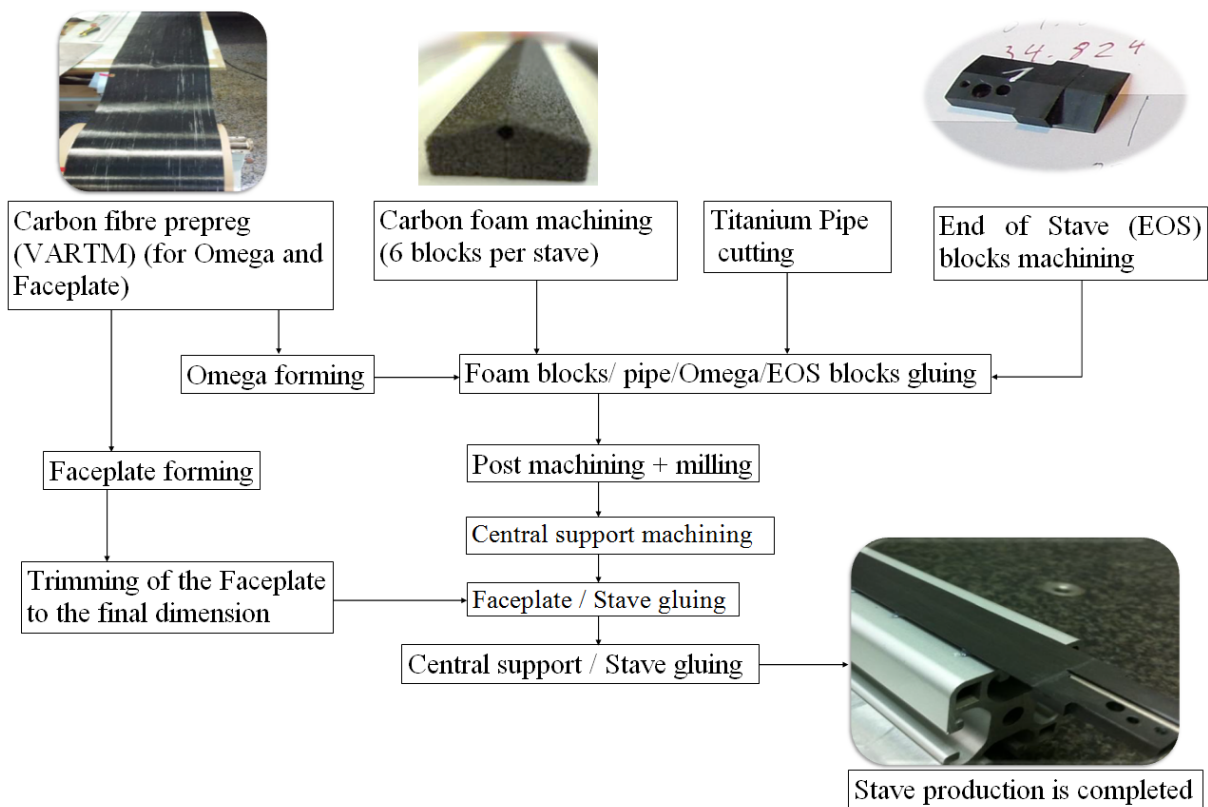
FIGURE 5: Manufacturing Procedure for Producing the IBL Stave [8]

1.4 Arrangement of Staves

Normally, the staves are arranged around the beam-pipe with a tilt angle allowing for an azimuthal overlap of staves. This is to ensure a complete coverage of charged particles in ϕ (Figure 6) and also to compensate for the Lorentz angle in the magnetic field of the ATLAS detector. In this context, the IBL is shown as an example in Figure 6, where 14 staves are tilted with an angle of $14°$ and $\phi = 25.714°$. In order to compensate for the Lorentz angle, the staves are tilted. The tilt is used as overlap distance. The average radial distance of the sensitive area from the beam pipe is $33\,\mathrm{mm}$ whereas the total envelope of the IBL in radius (R) is between $31\,\mathrm{mm}$ and $40\,\mathrm{mm}$ [10]. Figure 6 shows the explanation of the IBL structure in the $R - \phi$ plane, where the distance CM is called the overlap. This distance represents the number of pixels which would be hit in both the sensors by a high energy particle in the transverse plane. The overlap is mandatory for a correct alignment of the full detector [11] (Figure 6). More details on the tilt angle and overlap can be found in [11].
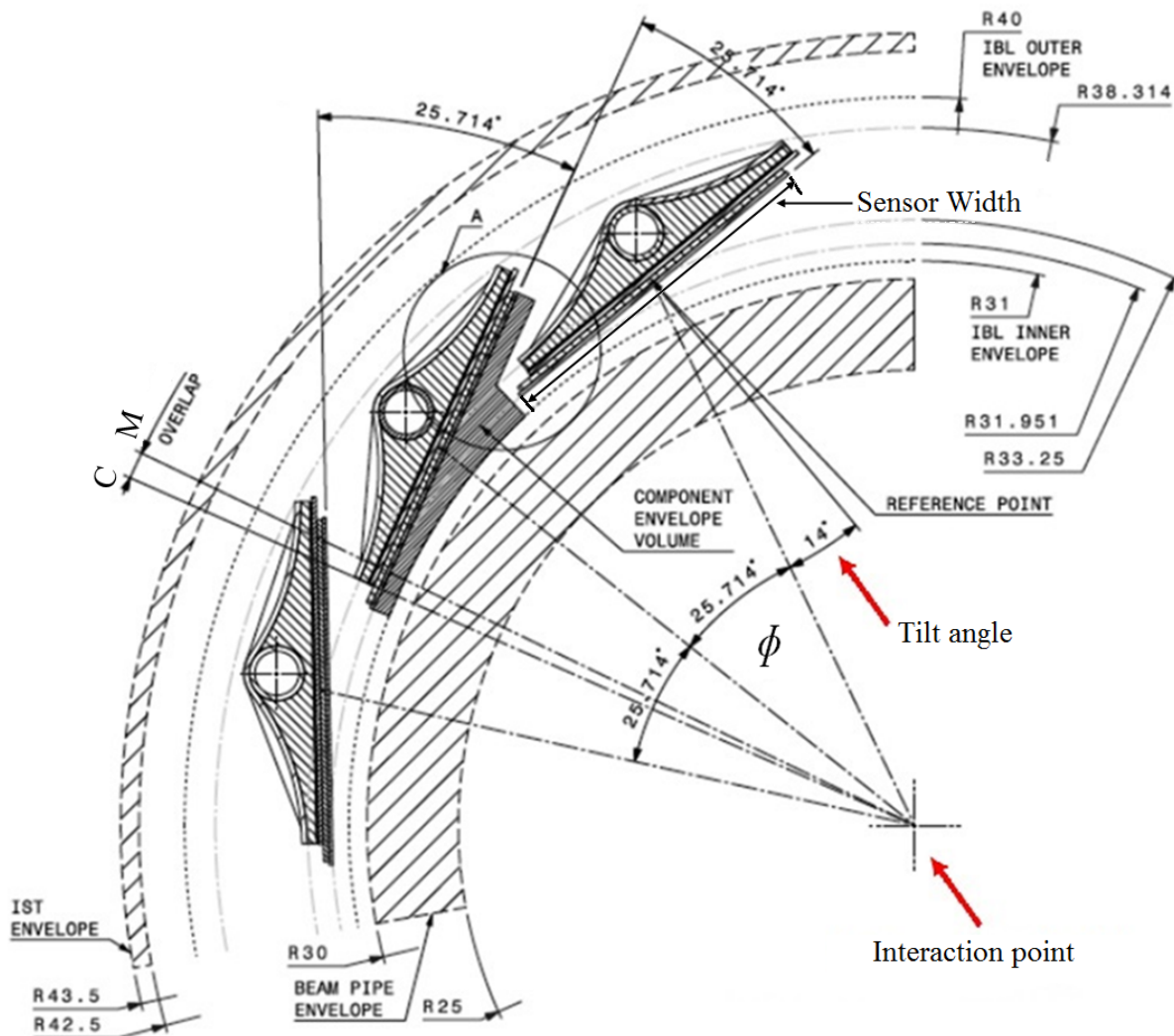
FIGURE 6: Arrangement of IBL staves and a description of the overlap [9]

2 Introduction to the Specifications, Aims and Objectives of the Thesis

2.1 An Overview of the Parameters of the Stave

2.2 Thermal Figure of Merit

The thermal Figure of Merit (TFM) represents an equivalent conductive thermal resistance of the stave (Figure 7) [12]. It is the thermal global effect of the parts interposed between the electronics (modules/sensors) and the inner surface of the cooling pipe. Here the power exchange takes place through the convection transfer to the boiling coolant fluid CO_2 at around - 40°C.
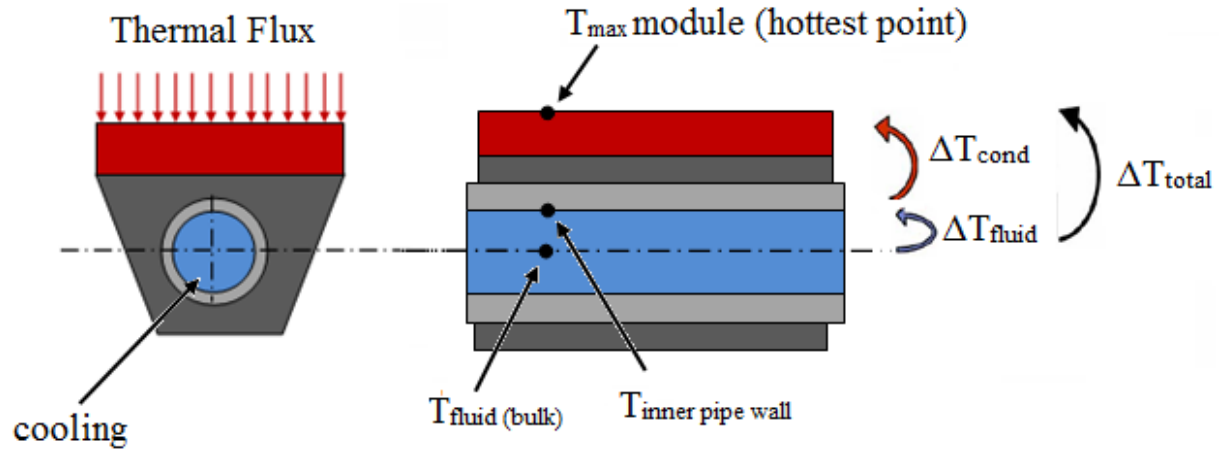
FIGURE 7: Schematic representation of the stave thermal figure of merit [12]

The exchange is roughly constant along the stave (Figure 7) [12] and it is explained in the equation below:

$$F_{TFM} = \frac{\Delta T_{total}}{q} \tag{2.1}$$

where, F_{TFM} is the total thermal figure of merit measured in $°C\,cm^2\,W^{-1}$. q is the heat flux which is measured in $W\,cm^{-2}$ and ΔT_{total} is the temperature difference between the cooling fluid and the pixel electronics (measured in °C). ΔT_{total} is given by sum of the following contributions:

$$\Delta T_{total} = \Delta T_{electronics} + \Delta T_{fluid} + \Delta T_{cond} \tag{2.2}$$

where, $\Delta T_{electronics}$ is the temperature difference defined across the sensors, the stave-electronics thermal adhesive and the bump-bonding. It is driven essentially by the thermal conductivity of the glue.

ΔT_{fluid} is defined due to the fluid thermal convective contribution which is the temperature difference between the fluid (bulk) and the pipe inner surface.

ΔT_{cond} is the temperature difference across the stave solid materials, driven essentially by the thermal conductivity of the material.

2.2.1   Conductive Thermal Figure of Merit of the Stave (Without Electronics)

The influence of the $\Delta T_{electronics}$ and ΔT_{fluid} are not considered in this thesis, since they could only be measured from the experimental testing. This research concern only towards the calculation of ΔT_{cond} from the inner surface of the cooling pipe upto the stave section. The formulation of the global stave conductive effect which is a measure of the stave conductive thermal resistance can be expressed as :

$$S_{TFM} = \frac{\Delta T_{cond}}{q} \tag{2.3}$$

where, S_{TFM} is the thermal figure of merit of the stave without the electronics and it is also measured in $°C \, cm^2 \, W^{-1}$. A good stave should have a low thermal figure of merit. The value of the input load from the electronics which is the heat flux is equal to $0.72 \, W \, cm^{-2}$ and the temperature of the pipe inner surface is equal to $0 \, °C$.

2.3   Radiation Length

When a charged particle penetrates in matter, it will interact with the electrons and nuclei present in the material through the electromagnetic force. Collisions of the charged particle with the nucleus will cause them to change direction as shown in Figure 8 [13]. A small amount of the particle's energy is lost in each of a large number of collisions with the electrons along its trajectory.
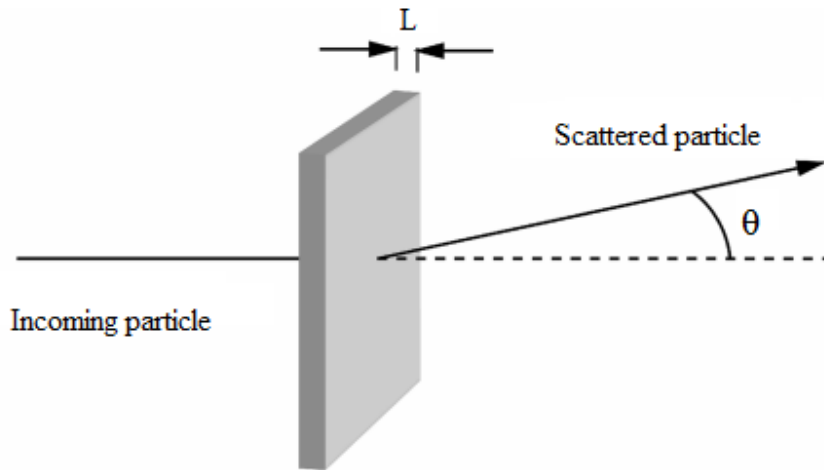
FIGURE 8: Representation of a charged particle penetrating a material [13]

The properties of a material with respect to the electromagnetic interaction can be approximated by the term "radiation length (X_0)" (Equation 2.4)

$$X_0 \approx \frac{716.4 \cdot A}{Z(Z+1) \ln \dfrac{287}{\sqrt{Z}}} \quad g \, cm^{-2} \tag{2.4}$$

These interactions depend on the atomic number Z and atomic weight A (Equation 2.4). The bigger the radiation length of the material, the more it is transparent to the radiation. The name radiation length is misleading. Actually it is the matter density times its thickness. This is also referred to as an area density (Equation 2.5) :

$$X = \rho \cdot s \tag{2.5}$$

where ρ is the density in $\mathrm{g\,cm^{-3}}$ and s is the path length expressed in cm. The overall effect should be proportional to the number of atoms seen by a particle.

In case a structure consists of several materials (Figure 9) with different radiation length, the individual contributions add as follows:

The total number of radiation length (N) is the sum of the contribution of different materials (i) in a structure.

$$N = \frac{d_1 \rho_1}{X_1} + \frac{d_2 \rho_2}{X_2} + ... \frac{d_i \rho_i}{X_i} = N_1 + N_2 .... N_i \tag{2.6}$$

where N specifies the overall effect of the structure (Figure 9) traversed by a particle. N is most often specified in %.

Thickness of the structure $d_0 = d_1 + d_2$
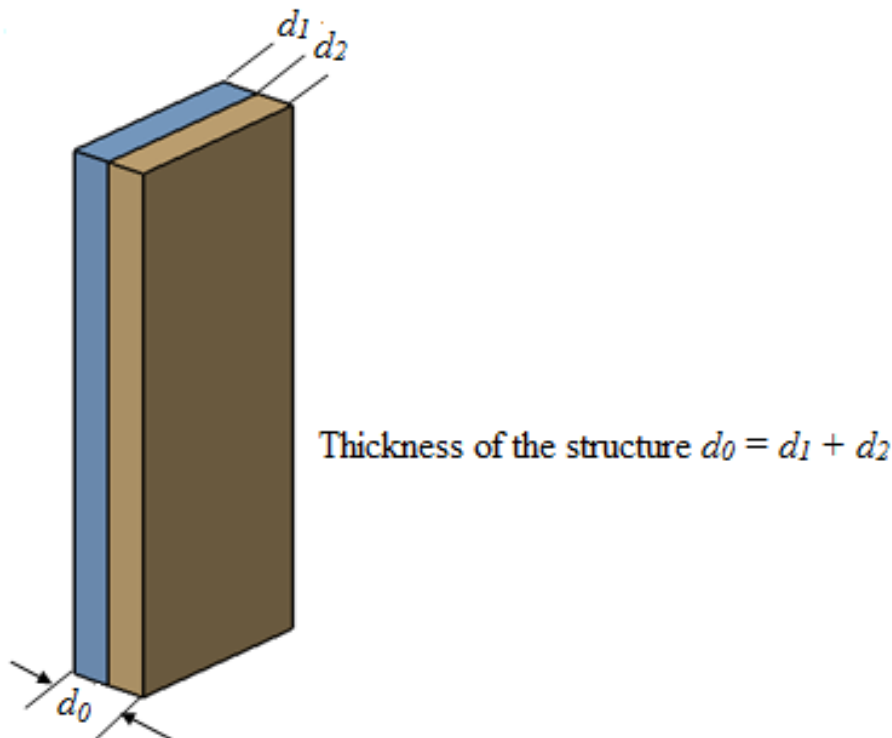
FIGURE 9: Representation of a structure for calculation of total number of radiation length based on the thickness [14]

A general objective of the stave design is to reduce the total number of radiation length of the stave.

2.4   Quasi-Static Load Conditions

Finite element modelling based quasi-static analysis is carried out to determine the behaviour and the deformation of the stave when it is subjected to:

- **Deformation due to the thermal cool down**

  A fixed temperature decrement ΔT = - 60 °C. The ΔT value of - 60 °C is determined by the difference between the hypothetical minimum temperature of the cooling fluid in the pipes (- 40 °C) and the environment temperature, assumed to be 20 °C.

- **Deformation due to the gravity**

  Gravity loads consist of the weights of the stave itself and of all other material and parts permanently attached to the stave.

- **Deformation due to the pressure**

  Deformation due to pressure load is calculated with the carbon fibre pipe subjected to an expected maximum internal pressure of 150 bar.

2.5   Eigenvalue Analysis

Eigenvalue analysis is carried out to determine the natural frequencies and the mode shapes of the stave without considering damping. This will indicate how the stave would respond to dynamic loading. The most relevant result to evaluate, would be the first vibration mode. The requirement for the minimum resonant frequency of the stave should be $> 50\,\mathrm{Hz}$, as it is very important to have a value significantly bigger than the frequency of the electronic power supply.

For all the above load cases, the stave is subjected to the boundary condition as shown in Figure 10 where both the ends of the stave are fully constrained and a middle support allows the stave to slide in the longitudinal direction.
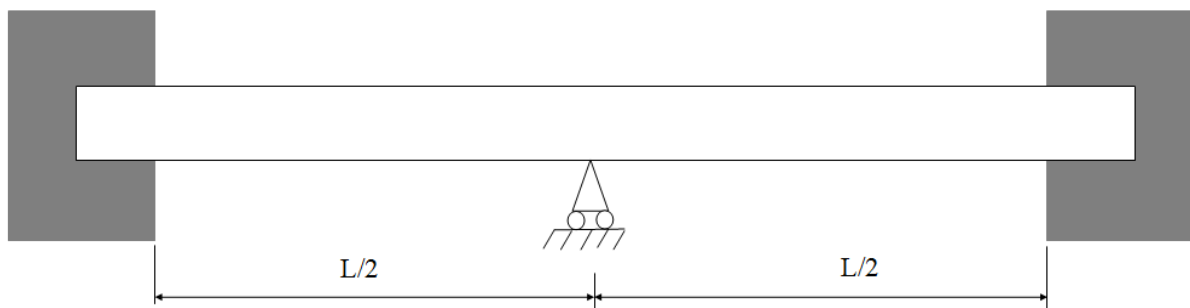
FIGURE 10: Schematic representation of boundary condition for thermomechanical load conditions

2.6 Research Motivation

New technologies should be developed so that the support structures can survive harsh radiation at the HL-LHC. The layout of the detector is an input to the stave design. Figure 11 shows the tentative radial positions of the so called Innermost and Outermost detector layers. The Innermost layer L0 stave is proposed to be mounted with a double chip module of 20×40 mm^2. The stave in the layer L1 as well as staves of the outermost layers is proposed to be mounted with quad modules of 40×40 mm^2. The heat generated by the sensor electronics must be dissipated effectively and this must be done with lightweight materials. New stave designs must be developed by considering these constraints and satisfying the requirements as listed in Table 1. The most relevant requirements are, stability, thermal performance and material budget. The development of stave designs completely based on carbon is the main focus of this thesis. The parameters shown in Table 1 have already been explained in sections 2.2 - 2.5. The innermost layers L0 and L1 (Tables 1, 2 and Figure 11) are the only focus of this thesis.

| Innermost layers | L0 ≈ 39 mm |
| | L1 ≈ 78 mm |

Outermost layers	L2 ≈ 160 mm
	L3 ≈ 200 mm
	L4 ≈ 300 mm
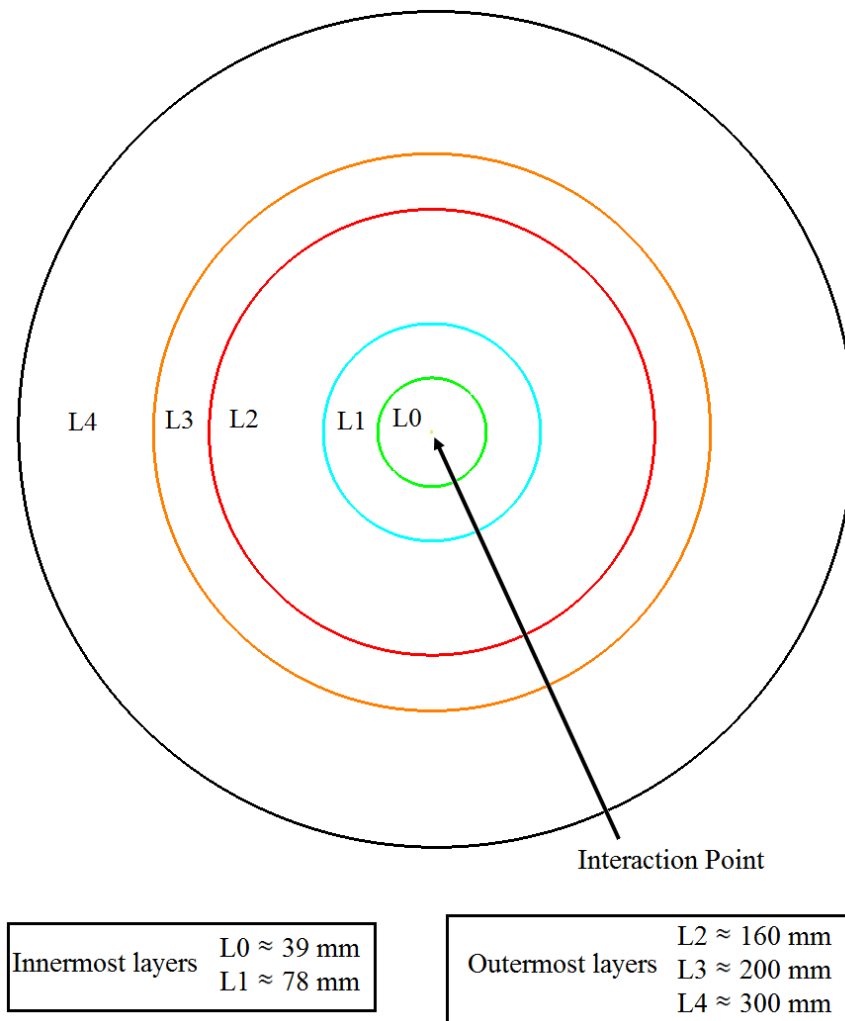
FIGURE 11: Schematic representation of the detector layers based on their radial position

Parameters of the stave	Performance of existing IBL stave [8]	Requirements for new stave (Layers L0 and L1) [15]
Conductive Thermal Figure of Merit	$15\,°C\,cm^2\,W^{-1}$	$< 15\,°C\,cm^2\,W^{-1}$
Deformation due to Gravity	$150\,\mu m$	$< 100\,\mu m$
Deformation due to Thermal Cool Down	$150\,\mu m$	$< 100\,\mu m$
Deformation due to Pressure	$150\,\mu m$	$< 100\,\mu m$
Minimum Resonant Frequency	$> 50\,Hz$	$> 50\,Hz$
Stave X/X_0 (without electronics)	$0.6\,\%$	$< 0.5\,\%$

TABLE 1: Design requirements for the stave within the HL-LHC

Detector	Width of the stave	Length of the stave
Innermost Layer L0	$20\,mm$	$750\,mm$
Innermost Layer L1	$40\,mm$	$1500\,mm$
Outermost Layers L2, L3 and L4	$40\,mm$	$1500\,mm$

TABLE 2: Stave design data for the innermost and outermost layers

2.7   Problem Statement

Advanced thermal stability systems envisioned for the local support structures of the pixel detectors used in high energy physics require rapid dissipation of heat away from the sensor electronics (pixel modules). Current (IBL) support structure's cooling is provided by titanium pipes. Metallic materials are in principle good option for the module (electronics) thermal management. However, titanium poses a problem of the Coefficient of Thermal Expansion (CTE) mismatch between different materials. Moreover, they have a shorter radiation length. This initiates the search for alternative materials.

Carbon fibre reinforced composites are good alternatives and are distinguished by low density, high strength, rigidity, excellent damping properties and lower CTE. To minimize the temperature non-uniformities over the pixel electronics and the temperature gradient between the pixel electronics and the coolant, the material of the stave in contact with the pixel electronics has to have a good in plane as well as through the thickness thermal conductivity. Carbon fibres have high in-plane thermal conductivity, however in the out of plane direction, the thermal conductivity of carbon fibre reinforced composite is no more than 1 W/mK due to the laminate structure [16] as polymeric resins are insulators. The high in-plane thermal conductivity promotes heat spreading, lower out of plane thermal conductivity hinders heat removal in the out

of plane direction.

Textile composites are the promising new class of composites finding their applications in aerospace, automotive and manufacturing industries as they possess exceptionally high ratios of strain to failure in tension, compression or impact load as compared to traditional unidirectional prepreg composites [17]. Woven fabric composite laminates offer a number of attractive properties compared to their unidirectional tape counterparts such as lower production costs, better drapability (the ability of a fabric to conform to a complex surface), good resistance to fracture and transverse rupture due to weaving resistance and high impact strength [18]. Although the mechanical properties are not as good as those of their non-woven counterparts, they still offer reasonable specific stiffness and strength with particularly good impact and energy absorption characteristics [19].

Fillers are materials that are added to a polymer formulation in order improve their properties. In recent years, the fillers have been applied to compensate the low out of plane thermal conductivity and the premature failure of the composite. Polymer matrices are usually filled with the thermally conductive fillers like graphene, carbon nano-tubes (CNTs), carbon black (CB), vapour grown carbon nano-fibres (VGNFs), aluminium nano-particles, diamond powder (DP). Graphene, CNTs and VGNFs are relatively expensive and they have higher properties only in the axial direction. The current cost of 50×50 cm mono-layer graphene thin film on copper foil is \$263 and on PET is \$819. At the same time, 5-8 nm thick graphene nanoplatelets are being sold by XG Sciences at \$219 to \$229 per kg [20]. Currently, bulk purified multiwalled carbon nano-tubes (MWCNTs) are sold for less than \$100 per kg, which is 1- to 10-fold greater than commercially available carbon fibre [21]. There are several technical and non-technical obstacles with CNTs such as controlling their orientation during dispersion, complex fabrication process, environmental concerns [22]. The use of expensive conductive fillers are not cost effective considering their technical obstacles.

In comparison, diamond is one of the hardest known natural material and it is a good conductor of heat. It is isotropic in nature and does not require special fabrication technique for dispersing them as powder. 10 grams of DP with size from 0.5 - $1\,\mu m$ are being sold at $0.55€$ by AB Industrial Diamonds, Germany. Considering the benefits of diamond and a promising possibility as filler in composites, an understanding about their relative behaviour is necessary. The application of DP filler towards the thermal, elastic and failure behaviour (tensile and flexural) of composites are one of the focus of this thesis. The properties of DP enhanced composites would directly influence the development and analysis of novel support structure designs.

2.8   Aims and Objectives

The aims and objectives of this research are

1. To investigate the synergistic effect of the diamond powder filler incorporation towards the out of plane thermal conductivity of the standard modulus (T300) and high modulus (YS90A) woven fabric composites (numerical and experimental).

2. To predict the elastic properties of the epoxy-diamond powder matrix through the homogenisation method and to develop the micromechanical unit cell model to predict the elastic properties of the diamond powder filled woven T300 and YS90A fabric composites.

3. To develop finite element based simulation models in order to evaluate the tensile and the flexural behaviour of the diamond powder filled T300 and YS90A woven composites through the progressive damage modelling.

4. To develop the novel local support structure (stave) designs for the innermost detector layers with improved thermal, thermomechanical behaviour along with the reduction of the total radiation length of the stave.

5. To use the simulation models for improving different stave concepts.

6. To build the prototypes of the realistic stave designs along with the possible experiments on prototypes in order to compare the numerical results.

2.9   Contents of this Thesis

This PhD thesis is constructed into eight chapters and the work flow is shown in Figure 12. In Chapter 1, an introduction and a general overview about the LHC and the ATLAS experiment have been presented. Chapter 2 explains the general parameters of the stave. The research motivation, problem statement, aims and objective of this research have also been elaborated. In Chapter 3, a literature review related to the standard modulus and the high modulus carbon fibres, thermal and mechanical behaviour of composites are presented.

Chapter 4 has been split in two parts, the first part elaborates the role of diamond powder filler towards the out of plane thermal conductivity of composites. Micromechanical modelling with randomly generated microstructures of various fractions for predicting the out of plane thermal conductivity ($K_\perp$) are discussed. Experimental investigation to study the role of diamond powder in enhancing the $K_\perp$ of the standard modulus and high modulus composites are also presented. Second part of this chapter concerns towards the elastic and the failure behaviour. Numerical prediction of the elastic properties of the epoxy-diamond powder matrix through the

homogenisation method are presented. Micromechanical unit cell models to predict the elastic properties of diamond powder filled woven fabric composites are detailed. Finite element based numerical models were developed to evaluate the failure behaviour of diamond powder filled woven composites under tensile and flexure through the progressive damage modelling technique.
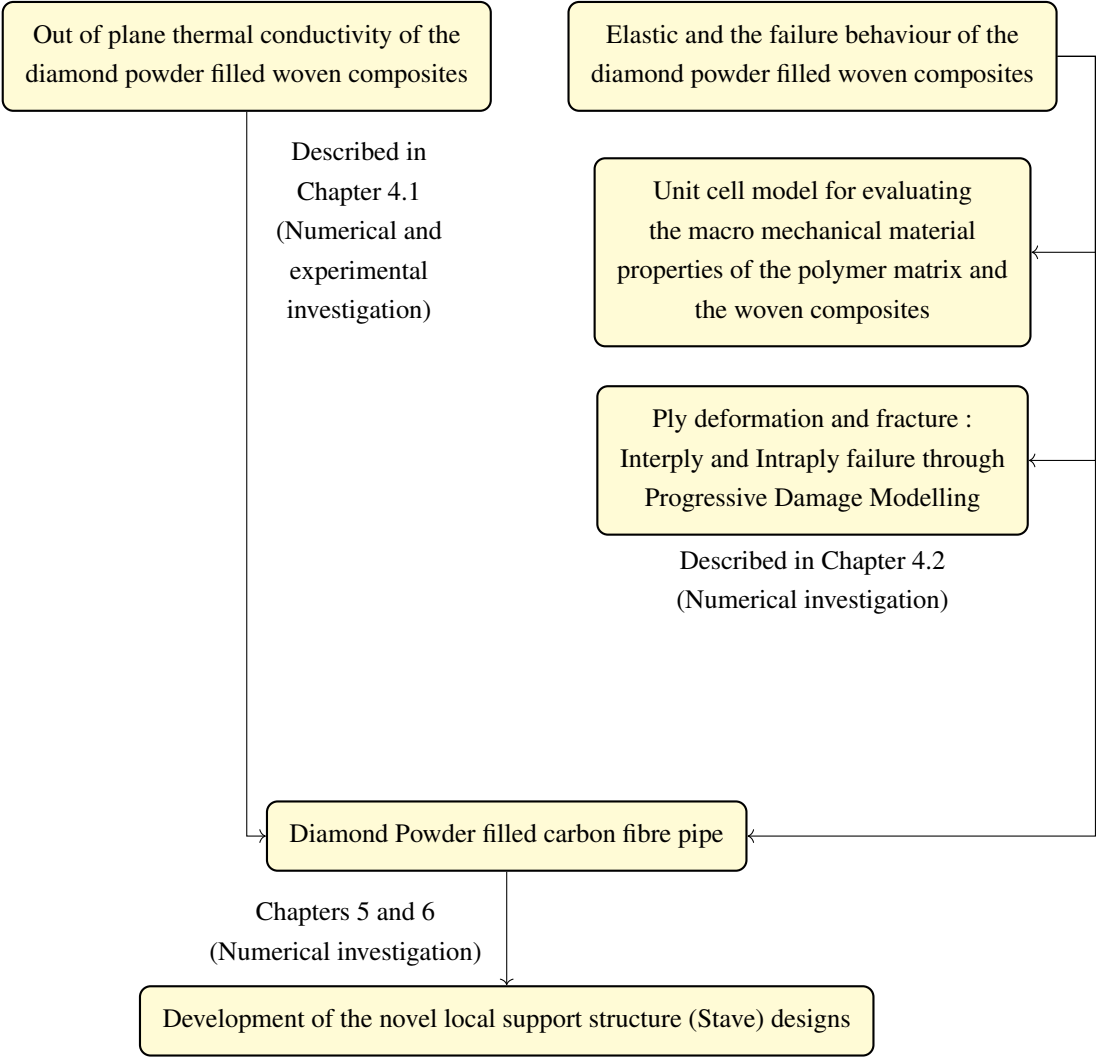
FIGURE 12: Work flow for development of new stave designs

Chapters 5 and 6 explains the development of the novel stave support structure designs with an enhanced thermal and thermomechanical performance through the finite element modelling and the development of the prototypes of the stave design have also been elaborated.

Total summary of results of this thesis along with conclusions have been included in Chapter 7 and the outlook for the future work have been discussed in Chapter 8.

3   Theory and the State of Art using Composite Materials

3.1   General Guide to Structural Composites

Composite materials are combinations of two or more different materials which work together to produce the properties that are superior to the properties of their own. Most composites consist of a bulk material which is a matrix and a reinforcement of some kind, added primarily to increase the strength and stiffness of the matrix. This reinforcement is usually in fibre form. The matrix material surrounds and supports the reinforcement materials by maintaining their relative positions.

3.1.1   Types of Matrix

Different types of resin are used in the composite industry and the majority of structural parts are made with polyester, vinylester and epoxy. Composites are divided into three main matrix groups [23]:

- **Polymer Matrix Composites (PMC)** : These materials use a polymer-based resin as the matrix, and a variety of fibres such as glass, carbon and aramid as the reinforcement. They are also known as Fibre Reinforced Plastics (FRP)

- **Metal Matrix Composites (MMC)** : These materials use a metal such as aluminium as the matrix, and reinforce it with fibres or particles such as silicon carbide.

- **Ceramic Matrix Composites (CMC)** : CMC are generally used in very high temperature environments, these materials use a ceramic as the matrix and reinforce it with short fibres or whiskers such as those made from silicon carbide and boron nitride. The ceramic tiles are widely used as a thermal protection in the space shuttles to overcome the heating during the entry into the earth's atmosphere.

3.1.2   Types of Fibre

1. Glass

The liquid glass is formed by blending the quarry products (like sand, limestone etc) at $1600\,°C$. The liquid is passed through micro-fine bushings and simultaneously cooled to produce glass fibre filaments from 5 - $24\,\mu m$ in diameter. The glass fibre is cheaper than other composite materials [23].

E-glass (Figure 13) has good electrical properties. It has high resistance to current flow [24] and it does not conduct electricity. E-glass is made from borosilicate glass.

C-glass (Figure 13) has the best resistance to chemical attack. They are mainly used in the form of surface tissue in the outer layer of laminates used in chemical, water pipes and tanks [23].

R, S or T glass (Figure 13) are the manufacturers trade names for equivalent fibres having higher

tensile strength and modulus than the E glass. They are mainly developed for aerospace and defence industries, and are used in some hard ballistic armour applications [23].

2. Aramid

Aramid fibre (Figure 13) is a man-made organic polymer (an aromatic polyamide) produced by spinning a solid fibre from a liquid chemical blend. They have high strength and low density giving very high specific strength. All grades of the aramid fibres have good resistance to impact and lower modulus grades are used extensively in ballistic applications [23].
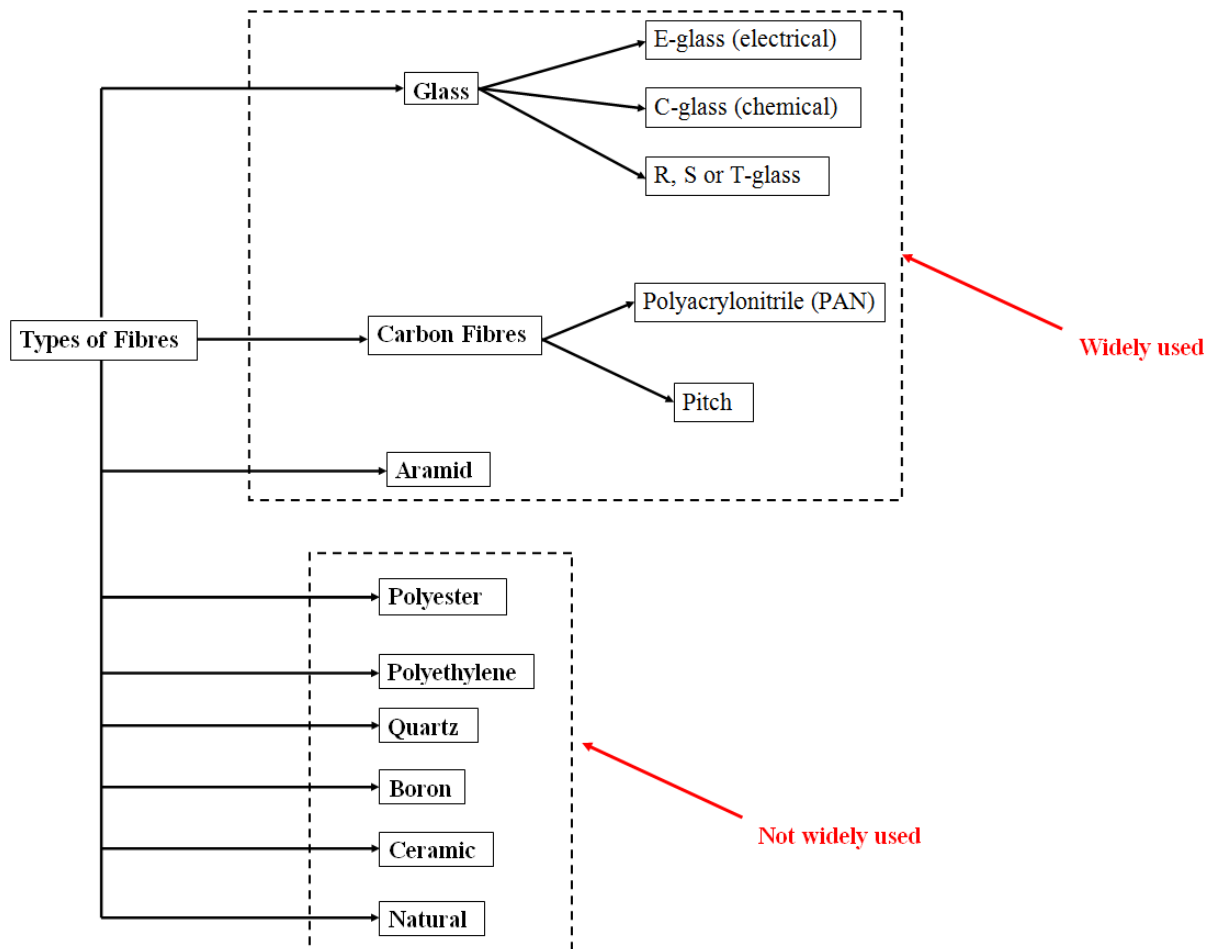
FIGURE 13: Different type of commercially available fibres

3. Polyacrylonitrile (PAN) and Pitch based Carbon Fibres

Fibres containing at least 92 wt% of carbon are called as carbon fibres, while the fibres containing at least 99 wt% of carbon are usually called as a graphite fibre [25]. The carbon fibres (Figure 13) are classified based on the raw material, product shape and material properties. In terms of the raw material, they are classified into the PAN based carbon fibre made from polyacrylonitrile (PAN) and the pitch based carbon fibre made from the pitch of petroleum or coal tar

[26]. Carbon fibres are very stiff and strong, 3 to 10 times stiffer than glass fibres. Advantages include its high strength and corrosion resistance. Disadvantages include its lower conductivity than other materials like aluminum.

3.1.3 Manufacturing Process of the Carbon Fibres

The only difference in the production of the pitch and the PAN based carbon fibres are the precursors** (Figure 14).
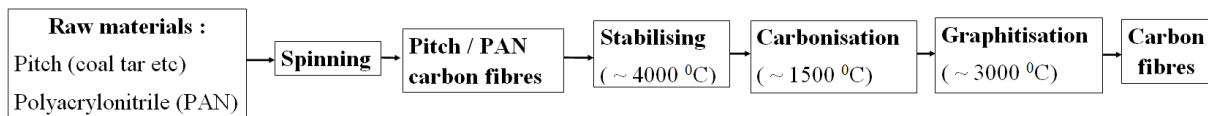
FIGURE 14: Difference in the process of the PAN and the pitch based carbon fibre manufacturing **

Most of the PAN based carbon fibres have a modulus $\approx$ 230 GPa and its highest modulus available in the market is about 600 GPa. The commercially marketed pitch based carbon fibres have a modulus of 50 to 950 GPa, thus the properties of the carbon fibres are widely varied depending on the raw material and are also classified based on the shape of the fibre which comes from the difference in the manufacturing process (Figure 14) [26].

The process of the production of carbon fibres begins with the heat treatment of raw materials. The melt spinning is the process of forming fibres through rapid cooling of a melt after which they are stabilised in order to cross link the fibres up to a stage where they could not be fused together [25]. They are then carbonised by heating the fibres to $\approx 1500\,^\circ$C without oxygen by which the crystalline carbon structures with a hexagonal shape without any impurities are formed [27, 28]. Then the graphitisation process is carried out by treating the fibres at $\approx 3000\,^\circ$C in order to improve the alignment and orientation of the crystalline regions along the fibre direction.

Since the graphite crystals are arranged parallel to the fibre axis, the pitch based carbon fibres have very high modulus, high thermal conductivity as they could diffuse the heat and also offer quick damping due to their high natural frequency. The pitch based carbon fibres lack high strength and are very expensive which is why the standard modulus PAN based carbon fibres are widely used due to their high strength to weight ratio, moderate stiffness and are also less expensive **.

**https://www.mrc.co.jp/dialead/english/pdf/2012062201.pdf

3.1.4   Elastic Properties of Fibres

The mechanical properties of the reinforcing fibres are considerably higher than those of the resin. The mechanical properties of the fibre/resin composite are therefore dominated by the contribution of the fibre to the composite.

The four main factors that govern the contribution of fibres are: [23]

1. **The basic mechanical properties of the fibre itself**. The basic elastic properties of the most commonly used fibres are given in Table 3.

Material Type	Tensile Strength (MPa)	Tensile Modulus (GPa)	Density ($g\,cm^{-3}$)
Carbon High Strength (HS)	3500	160 - 270	1.8
Carbon Intermediate Modulus (IM)	5300	270 - 325	1.8
Carbon High Modulus (HM)	3500	325 - 440	1.8
Carbon Ultra High Modulus (UHM)	2000	440+	2.0
Aramid Low Modulus (LM)	3600	60	1.45
Aramid HM	3100	120	1.45
Aramid UHM	3400	180	1.47
Glass - E glass	2400	69	2.5
Glass - S glass	3450	86	2.5
Glass - quartz	3700	69	2.2
Aluminium Alloy (7020)	400	1069	2.7
Titanium	950	110	4.5

TABLE 3: Basic elastic properties of fibres and other engineering materials

2. **The interface between the fibre and resin**. The surface interaction of fibre and resin is controlled by the degree of bonding that exists between the two. This is heavily influenced by the treatment given to the fibre surface .

3. **The fibre volume fraction in the composite**. The amount of fibre in the composite is largely governed by the manufacturing process. The reinforcing fabrics with closely packed fibres will give higher fibre volume fractions in a laminate than the fabrics made with coarser fibres. As a general rule, the stiffness and strength of a laminate will increase in proportion to the amount of fibre present. However, above about 60 - 70 %, the tensile stiffness and the laminates's strength may continue to increase to reach a peak and then will decrease due to the lack of sufficient resin to hold the fibres together properly .

4. **The orientation of the fibres in the composite**. The reinforcing fibres are designed to be loaded along their length. The anisotropic feature of the composites can be used to good advantage in designs, with the majority of fibres being placed along the orientation of the main load paths.

3.1.5   Important Styles of Fabric

The process begin with spooled unidirectional raw fibres packaged as continuous strands. An individual fibre is called a filament. Bundles of filaments are identified as tows, yarns, or rovings [24].

Unidirectional (UD)

The fibres in a unidirectional material (Figure 15) run in one direction and the strength and stiffness is only in the direction of the fibre. Pre-impregnated (prepreg) tape is an example of a unidirectional ply orientation. The fibre is typically impregnated with thermosetting resins. The most common method of manufacture is to draw collimated raw (dry) strands into the impregnation machine where hot melted resins are combined with the strands using heat and pressure. Tape products have high strength in the fibre direction and virtually no strength in the transverse direction. The fibres are held in place by the resin. Tapes have a higher strength in the fibre direction than woven fabrics [24].
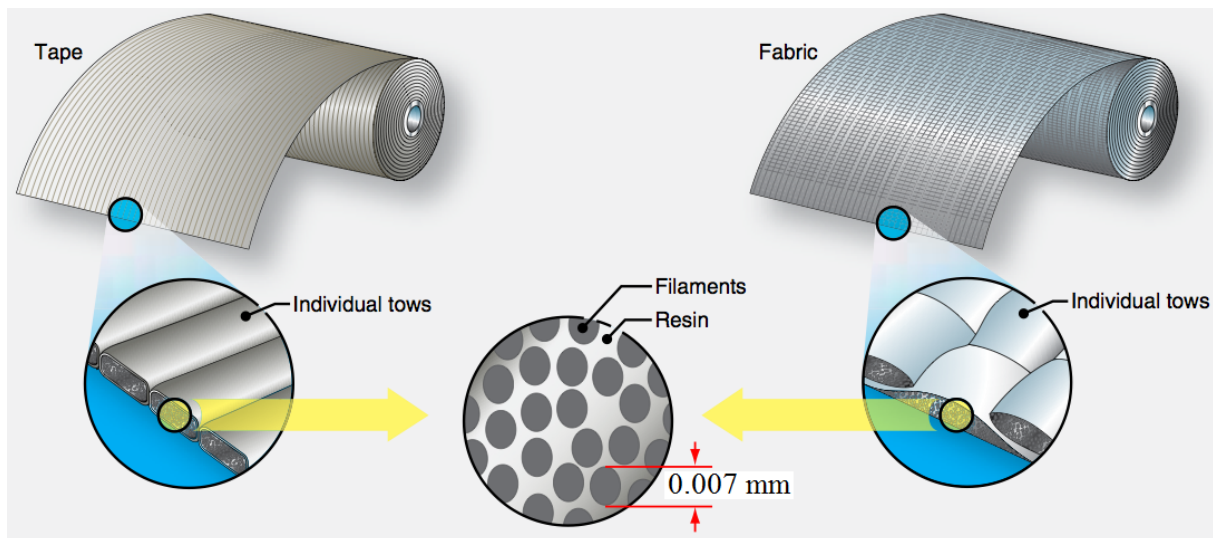
FIGURE 15: Unidirectional tape and woven fabrics [24]

Woven fabrics

Most fabric constructions offer more flexibility for layup of complex shapes than straight unidirectional tapes offer. Fabrics offer the option for the resin impregnation process. Generally, the fabrics used for the structural applications, use the fibres of same weight in both the warp (longitudinal) and weft (transverse) directions. Woven fabrics are usually the choice to save weight, minimizing resin void size, and maintaining fibre orientation during the fabrication process. Woven structural fabrics are usually constructed with reinforcement tows, strands, or yarns interlocking upon themselves with over/under placement during the weaving process [24]. The more common fabric styles are plain, twill and satin weaves (Figure 16).

Plain Weave   2/2 Twill Weave   Satin Weave
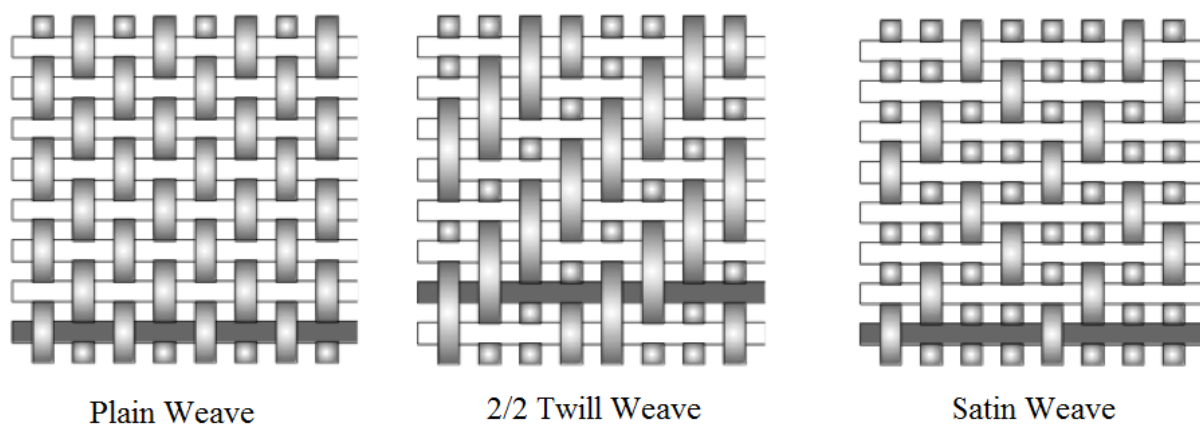
FIGURE 16: Different forms of the woven fabrics [23]

In the plain weave, each warp fibre passes alternately under and over each weft fibre. The fabric is symmetrical, with good stability and reasonable porosity. However, it is the most difficult of the weaves to drape (Figure 16) and the high level of fibre crimp imparts relatively low mechanical properties compared with the other weave styles [23].

In the twill fabric, one or more warp fibres alternately weave over and under two or more weft fibres in a regular repeated manner (Figure 16). With reduced crimp, the fabric also has a smoother surface and slightly higher mechanical properties than plain weave fabric [23].

In the satin weaves such as 5 harness or 8 harness[††], the fibre bundles traverse both in warp and fill directions changing over/under position less frequently. The satin weaves have less crimp and are easier to distort than a plain weave (Figure 16) [23]. Satin weaves allow fibres to be woven in the closest proximity and can produce fabrics with a close tight weave. The asymmetry

---

[††]The harness number used in the designation (typically 4, 5 and 8) is the total number of fibres crossed and passed under, before the fibre repeats the pattern

causes one face of the fabric to have fibre running predominantly in the warp direction while the other face has fibres running predominantly in the weft direction.

3.1.6   Composites with Matrix Fillers - A Literature Review

3.1.6.1   Thermal Conductivity

PAN (Polyacrylonitrile) and Pitch based carbon fibres are typical reinforcing materials in polymer matrix composites with thermal conductivity in the range of 15 - 1100 $\text{W m}^{-1}\text{K}^{-1}$ in the fibre direction [29]. However, in the out of plane (through the thickness) direction, the thermal conductivity of carbon fibre reinforced composite is no more than 1 $\text{W m}^{-1}\text{K}^{-1}$ [16]. Most polymer resins are known to be thermal insulators.

One of the alternative approaches for improving the thermal conductivity of a polymeric material, polymer matrices are usually filled with the thermally conductive fillers and some of them are listed in Table 4 [30].

Filler Material	Thermal Conductivity ($\text{W m}^{-1}\text{K}^{-1}$)
Aluminum nitride	200-320
Silicon carbide	611
Diamond	1000-2000
Copper	400
SWCNT	≈ 6000
MWNT	≈ 3000
Graphite	600

TABLE 4: Thermal conductivity of conventional thermal conductive fillers [30]

Jeon et al. reported that the incorporation of functionalised graphite flakes into epoxy resin yielded a thermal conductivity of 1.53 $\text{W m}^{-1}\text{K}^{-1}$ at 10 wt% and a modulus of 1.03 GPa at 1 wt% [31]. Fusao et al. [32] prepared a polymer composite by impregnating the epoxy resin with a network like α-alumina pellet containing 54% volume fraction of α-alumina particles and achieved a thermal conductivity of 4.2 $\text{W m}^{-1}\text{K}^{-1}$.

Carbon based fillers like single- walled carbon nanotubes (SWNT), multi-walled carbon nanotubes (MWNT), vapor-grown carbon nanofibres (VCNFs) are being used as fillers for developing thermally conductive resins[33, 34, 35] and recently Yang et al. observed no detectable change in the thermal conductivity of vapour grown carbon nanofibre (VGCNF) liquid crystal polymer composites with VGCNF content of as high as 15 weight% (wt%), which was

attributed to the nonuniform dispersion of nanofibres and the lack of a percolated network between them [36]. Patton et al. observed a 300% increase in the thermal conductivity of vapour grown carbon fibre (VGCF) polymer composites with 39 vol % VGCF, however, the magnitude of the thermal conductivity remained relatively low ($0.8 \, \mathrm{W \, m^{-1} \, K^{-1}}$) as compared to the intrinsic thermal conductivity of the filler and the low magnitude of composite thermal conductivity was attributed to the low efficiency in transfer of thermal energy between nanofibres [37].

Xing et al. reported an increase in thermal conductivity of the polymer composite up to $2.83 \, \mathrm{W \, m^{-1} \, K^{-1}}$ with high volume fraction (57.5%) of well-dispersed multi-walled carbon nanotubes and copper nanowires in the epoxy matrix [38]. Wu et al. studied that a vertically aligned MWCNT array embedded in a composite can provide direct channels for transmitting heat and more effectively increase the thermal conductivity of the composite [39]. One of the important concern with the CNTs are towards the uniform dispersion of the nanotube phase within the polymeric matrix and improved nanotube/matrix wetting and adhesion are critical issues in the processing of nanocomposites [40].

Another interesting filler material is graphene, which is a single layer structure of two-dimensional new carbon material [41] and it has attracted tremendous interest particularly from engineers and scientists due to its unique physical and chemical properties like strong mechanical robustness [42], excellent thermal conductivities (more than $5000 \, \mathrm{W \, m^{-1} \, K^{-1}}$ at room temperature) [43] and large specific surface area ($3100 \, \mathrm{m^2 \, g^{-1}}$ for activation of graphene) [44]. As graphene is in the early stage of development, there are a few issues related to the production methods as there are no good general synthesis methods that could produce graphene quickly and precisely. Some research has proven that graphene is susceptible to oxidative environments and could exhibit toxic qualities [45].

3.1.6.2 Elastic and Failure Behaviour

Typical failure modes of composites include fibre fracture, matrix fracture, fibre-matrix interface debonding and interlaminar delamination [46, 47]. The cohesive matrix fracture and adhesive fracture of the fibre-matrix interface are known as inter-fibre fracture [47] The inter-fibre fracture is macro damage that starts by the initiation of matrix micro-cracks at the fibre-matrix interface during matrix curing or due to transverse stress as a result of loading, thermal stresses, or fatigue loading. The micro-cracks subsequently propagate through the matrix to form macro-cracks.

In addition to the inter-fibre fracture of composites, the low failure strain and ductility are other drawbacks in the mechanical response when composites are loaded in fibre direction (on-axis loading) [48]. Normally, composites could be subjected to large-deflection bending and multiple impacts in service conditions and these quasi-static and dynamic loads generate high local

stresses and strains leading to complex damage modes due to heterogeneity and anisotropy of composite laminates. In a bending scenario, a laminate experiences transverse shear and normal stresses resulting in the interlaminar delamination damage, because of their low through-thickness strength and stiffness [49]. Damage evolution results in significant reduction of in-service mechanical properties and leads to a loss of structural integrity of the composite.

One of the recent promising techniques to overcome the premature failure of composites due to delamination/debonding is to reinforce the composites with fillers [18].

Filler Material	Density $\mathrm{g\,cm^3}$	Young's Modulus (GPa)	Tensile Strength (GPa)
CNTs	1.3-2.1	≈ 1000	11-63
Graphene	1.5-2	$\approx 532\text{-}1000$	48
Diamond	3.52	1000-1220	> 1.2

TABLE 5: Mechanical Properties of commercially available fillers

Carbon nanotubes (CNTs), nano-clay, graphene nanoparticles (GNPs), and nano-silica are common non-metallic nanoparticles used to fabricate nanocomposites [50, 51]. Discovered by Ijima in 1991 [52], CNTs have attracted many scientists worldwide, because of their distinguished mechanical properties compared with conventional structural materials. Hossain et al. [53] reported a 49% and 31% increase in the flexural strength and modulus of on-axis woven E-glass/polyester composites reinforced by 0.1-0.4 wt% carbon nano fibres (CNF). Qiu et al. [54] examined the tensile and shear behaviour of (GFRP) composites, with 1.0% by weight function-alised multi-walled carbon nanotubes (MWCNTs), it was reported that a 14% and 5% increase in on-axis tensile and shear strengths respectively. Tensile strength and modulus of the composites filled with CB increased with increasing filler contents but impact strength and elongation at break were reduced, they have also reported that the composites with more than 30% carbon black were very brittle and were difficult to mix.

3.1.6.3   Summary

In comparison to other fillers that are described in last two sections , diamond powder (DP) being a carbon-based filler has a unique combination of properties like hardness, thermal conductivity (1000 - $2000\,\mathrm{W\,m^{-1}\,K^{-1}}$), chemical, thermal inertness and abrasion resistance. Moreover they have a lower thermal expansion coefficient than metal [30] based fillers. Since diamond's are isotropic, there would not be any necessity for special manufacturing techniques for aligning diamond powder. Few studies have examined using fillers to improve the out of plane thermal conductivity, elastic and failure behaviour of woven composites. This investigation has been intended to predict those properties using diamond powder filler.

4 Thermal, Elastic and Failure Behaviour of the Diamond Powder Filled Woven Composites

4.1 Thermal Behaviour

4.1.1 Micromechanical modelling

Traditional laminated uniaxial or biaxial composites have low through the thickness thermal conductivities, which limit their use in a variety of applications. The axial and through the thickness thermal conductivities of some of the commercially available pitch and PAN based fibres are shown in Table 6.

Fibre	Base material	Axial thermal conductivity K_a $(\mathrm{W\,m^{-1}\,K^{-1}})$	Through the thickness thermal conductivity $K_\perp$ $(\mathrm{W\,m^{-1}\,K^{-1}})$
T300-fibre	PAN	8.5	5
T650/35-fibre	PAN	14	5
T650/42-fibre	PAN	15	5
P25-fibre	Pitch	22	10
P30X-fibre	Pitch	40	10
P120s-fibre	Pitch	640	2.4
K1100-fibre	Pitch	1000	10

TABLE 6: Thermal conductivities of commercially available fibres [55]

Since composites have more than one component, heat transfer in composites is governed by each component's thermal properties, their relative volume fractions, their geometrical arrangement and the weave style of fibre, etc [56]. Fibre arrangements in composites are typically non-uniform and nonperiodic [57]. Generally, periodic fibre arrangement [58, 59] are employed for simplicity, assuming that the material has a deterministic and ordered distribution of fibres. Fibre reinforced composites are far from being periodic materials because the fibres are randomly distributed through the matrix [60]. It is generally agreed that periodic fibre distributions lead to incorrect predictions of the elastic-plastic behaviour under transverse loading conditions [57]. No manufacturing process can guarantee perfect uniformity of fibre placement in the composite volume. Therefore, the analysis of composites with a random microstructure is desirable [61].

In order to have a detailed understanding of through the thickness thermal conductivity of the on-axis $(0° - 90°)$ woven standard modulus (T300) and the high modulus (YS90A) fabric composites, micromechanical finite element models were developed in Abaqus$^{\mathrm{TM}}$. An algorithm was developed to generate the random distribution of the microstructures (fibres through the matrix) within the two dimensional representative volume element(RVE). The representative volume element (RVE or the unit cell) is the smallest volume over which a measurement can be made that will yield a value representative of the whole composite [62].

4.1.1.1 Algorithm development - Unit cell generation

An algorithm [63, 64] was developed (in Matlab) to generate the random distributions of fibres in the unit cell which would be statistically equivalent to the actual carbon fibre reinforced composite microstructure. Fibres were generated with the radius r = $3.5\,\mu$m in the RVE and the radius was kept constant (Figure 17). The side length of the RVE was kept as L. The object was considered as a quadrate area, the size of the RVE was represented as δ which related to side length of RVE L to the radius of fibre r using the relationship δ = L/r (Figure 17).
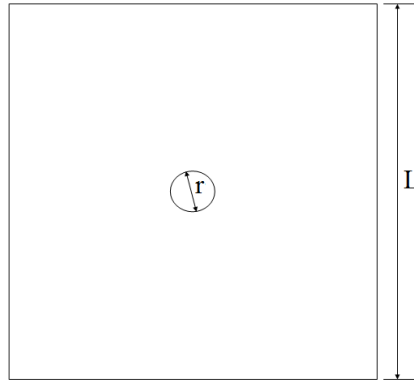
FIGURE 17: Schematic representation of the RVE

The algorithm proceeded in the following steps:

1. A random point for the first fibre was created with coordinates (x_1, y_1) (Figure 18).
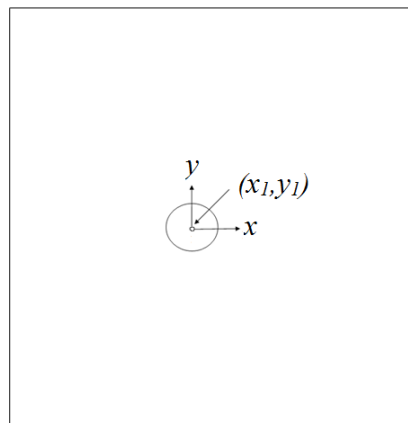
FIGURE 18: Assigning a random point for the center of first fibre

2. The second point (x_2, y_2) represents the center of a second fibre which would be the center of first nearest neighbour of the previous fibre. According to this algorithm all the accepted random coordinates of the fibres must pass certain conditions in order to control the position of new point: the distance d_1 (Equation 4.1) from (x_1, y_1) to (x_2, y_2) and the orientation angle θ_1 (Figure 19) which is a random angle ranging between 0 and 2π [60].

$$d_1 = \sqrt{(x_2 - x_1)^2 + (y_2 - y_1^2)} \qquad\qquad (4.1)$$

The distance d_1 was given a certain condition to avoid overlapping. As suggested by Melro et al. [65] a value of 2.7 (Equation 4.2) for d_1 was fixed. To fulfil this condition, the center coordinates of the ith fibre must pass the following check

$$d_1 \geqslant 2.07 \times r \tag{4.2}$$

$$\|\vec{X^i} - \vec{X^k}\| \geqslant d_1 \qquad \text{k=1,\ldots, (i-1)} \tag{4.3}$$
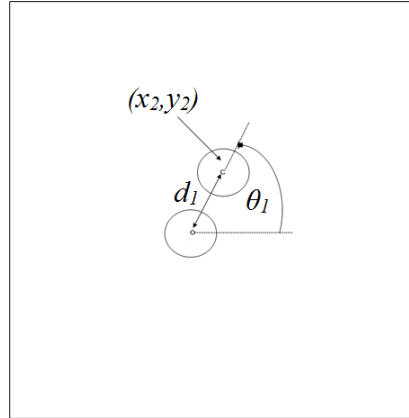
FIGURE 19: Assigning second fibre based on nearest neighbour.

3. If the fibre surface touches the surface of the RVE or if they are very close, it may not be possible to mesh or the generated FEM mesh might be distorted. To avoid these situations, fibres are kept at a minimum distance (s_1) from the surface of the RVE

$$s_1 \geqslant r + (0.1 \times r) \tag{4.4}$$

4. Steps 2 and 3 were repeated to generate new fibres surrounding the first fibre (Figure 20). Throughout the procedure, checks were performed to ensure the distance between the fibre centres and the distance from the surface of the RVE to make sure fibres lie within the RVE.
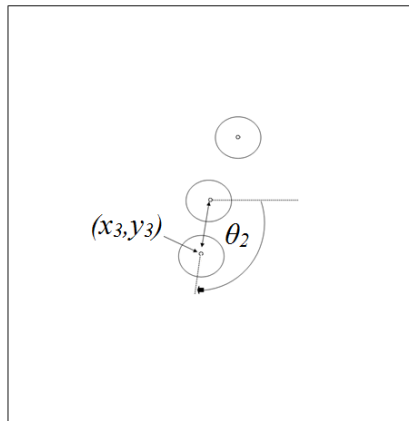
FIGURE 20: Assigning subsequent fibres

5. The algorithm was made to move to the second fibre and steps 2, 3 and 4 were re-
   peated.The entire process was repeated to all the fibres thereafter until the desired fibre
   volume fraction was reached or until the sample area was filled. The fibres were generated
   through Abaqus^{TM} python scripting.

6. A separate script was developed for generating the number of fillers (with a constant ra-
   dius $r_f = 0.5\,\mu m$) and their coordinates based on their specified volume fraction within the
   RVE. A minimum center distance between the fibre and the diamond filler were specified
   as shown in Equation 4.5 in order to maintain a random fibre-filler distance.

$$d_2 \geqslant r + (1.2 \times r_f) \tag{4.5}$$

7. Another condition was specified to maintain the filler-filler distance which are shown in
   Equation 4.6.

$$d_3 \geqslant r_f + (1.2 \times r_f) \tag{4.6}$$

The fillers were generated in the RVE through a python script in ABAQUS^{TM} after know-
ing their coordinates. Figure 21 represents the development of RVE based on an algorithm
by which YS90A carbon fibres were randomly generated with 50 % of fibre volume frac-
tion and $1.6\%(a), 8\%(b), 12\%$ (c) volume fractions of DP in the RVE.
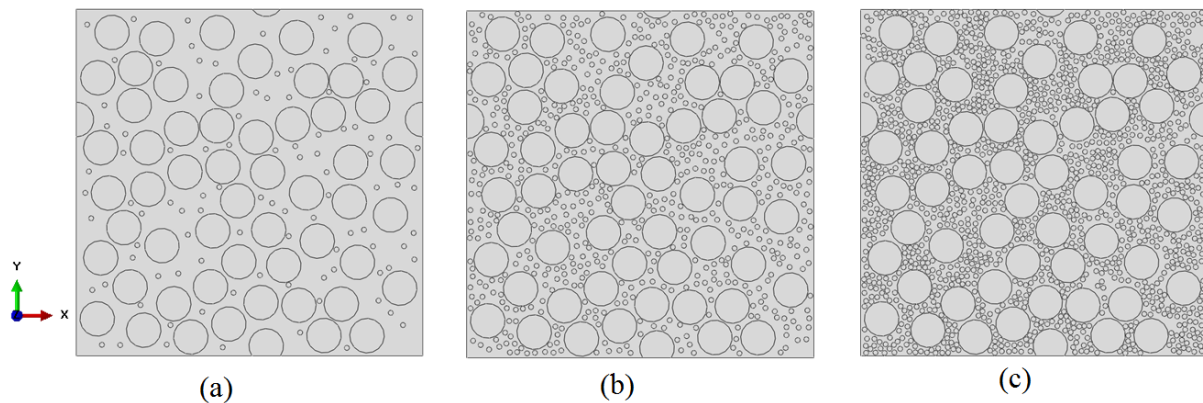
FIGURE 21: RVE's with randomly generated YS90A fibre of 50% volume frac-
tion and $1.6\%(a), 8\%(b), 12\%$ (c) volume fractions of Diamond Powder

4.1.1.2   Model set up

Three different sets of steady state heat transfer FEM was performed (Table 7). The RVE
with randomly generated T300 fibres (44% and 55% volume fractions) and YS90A fibres (50%
volume fraction) were incorporated with randomly distributed DP within the epoxy matrix.
Different loadings of DP in the RVE are shown in Table 7

Fibre	Fibre volume fraction (%)	DP volume fraction in the composite (%)
T300	44	0
T300	44	0.8
T300	44	1.6
T300	44	3
T300	44	8
T300	55	0
T300	55	0.7
T300	55	1.4
T300	55	2.7
T300	55	6
T300	55	11
T300	55	14
T300	55	16
YS90A	50	0
YS90A	50	1.6
YS90A	50	5
YS90A	50	6
YS90A	50	8
YS90A	50	10
YS90A	50	12

TABLE 7: Details of FEM models under steady state heat transfer

The models were meshed with three node linear heat transfer triangular elements DC2D3 (Figure 22). Two temperature conditions were set represented as T_1 and T_0. The insulated surfaces prevented convection and the direction of heat transfer was perpendicular to boundary lines of the heat sink (Figure 23). With the prescribed constant temperatures, the heat flux (Q) was calculated by integrating the entire T_1 surface formulated in Equation 4.7, where $q(x, y)$ is the heat flux in Cartesian coordinates.

$$Q = \frac{1}{2h} \int_{-h}^{h} q(x, y) dx \tag{4.7}$$

The out of plane thermal conductivity ($K_{\perp_{FEM}}$) was predicted from the calculated heat flux (Q) and knowledge of the temperature distribution (ΔT) across the distance (Δh) of a medium represented by Equation 4.8.

$$K_{\perp_{FEM}} = \frac{\Delta h \cdot Q}{\Delta T} \tag{4.8}$$

FIGURE 22: Finite element model with three node linear heat transfer triangular element and the boundary condition for the model setup

FIGURE 23: Boundary condition for the model setup

4.1.2   Experimental methods

The experimental investigation was carried out to validate the finite element simulation results. PAN based T300 carbon fibre fabric woven in 2/2 Twill was supplied by Cytec Thornel, Inc and Pitch based GRANOC YS90A carbon fibre fabric woven in plain weave was supplied by Nippon Grap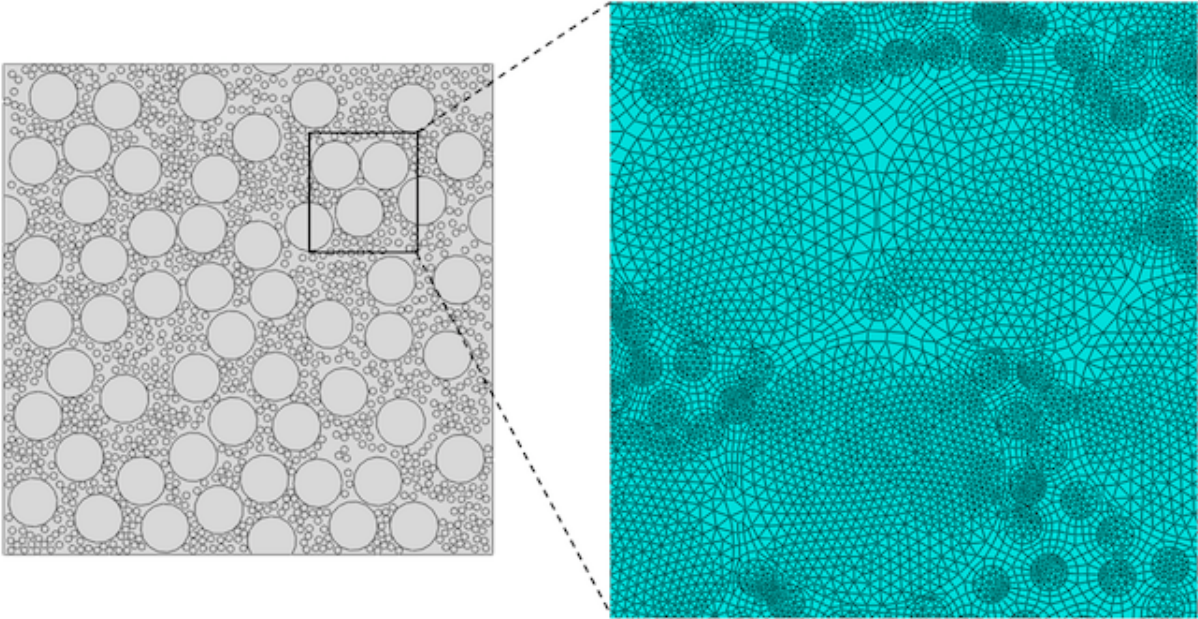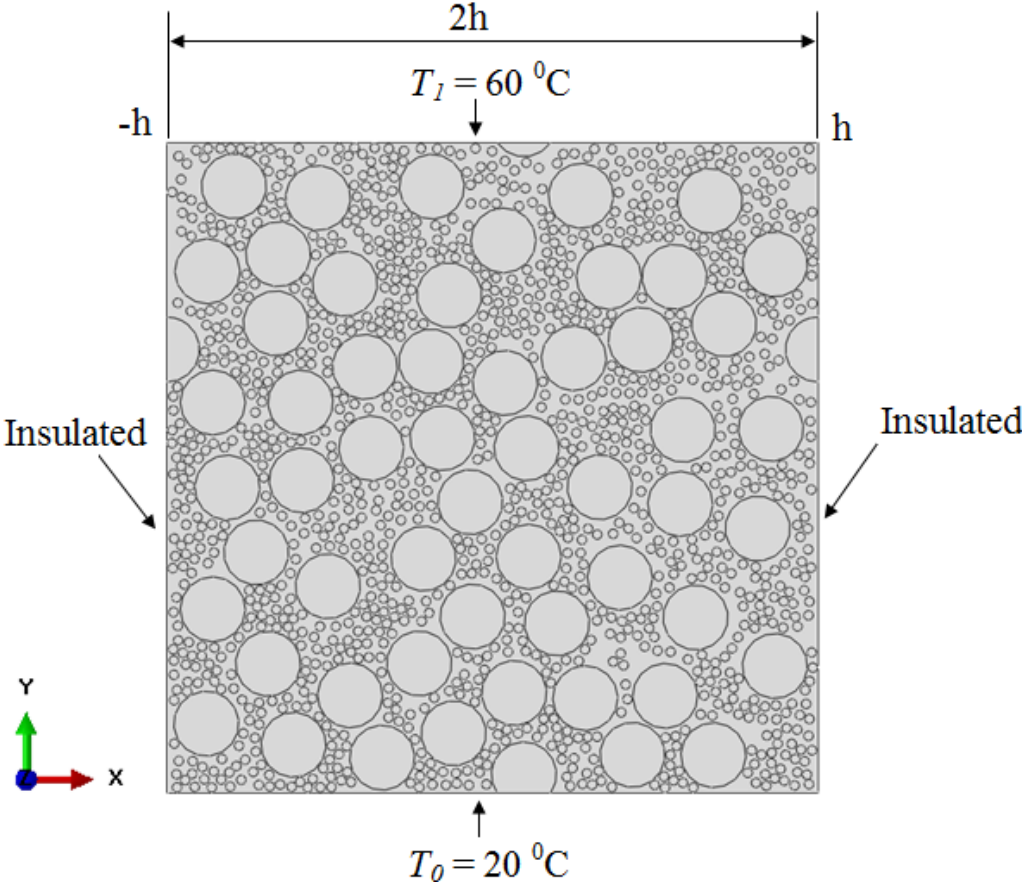hite fibre Corporation. Both the fabrics had the fibre diameter of $7\,\mu$m. The fabric data[‡‡] and fibre material properties are given in Table 8. The epoxy and hardener used in the fabrication are commercially available LARIT RIM 135 and LARIT RIM 134. The resin to hardener mixing ratio was 2:1, the pot life (pot life is a defined time during which the viscosity of the resin-hardener mixture doubles) was 30-45 minutes and the set time was 5-6 hours. Diamond Powder with diameter from 0.5 - 1 μm, thermal conductivity of $1000\,\mathrm{W\,m^{-1}\,K^{-1}}$ and density of $3.5\,\mathrm{g\,m^{-3}}$ was supplied by AB Industrial Diamonds, Germany. Both T300 and YS90A On-axis (0°-90°) fabrics had same number of yarns in the weft and warp directions.

	Fabric Data			**Fibre Material Properties**		
Fibre	Fabric	Fibre Density $(\mathrm{g\,cm^{-3}})$	Areal Weight $(\mathrm{g\,m^{-2}})$	Tensile Strength (GPa)	Tensile Modulus (GPa)	Axial Thermal Conductivity $(\mathrm{W\,m^{-1}\,K^{-1}})$
T300	Twill 2/2	1.76	395	3.75	231	8
YS90A	Plain Weave	2.18	125	3.53	880	500

TABLE 8: Fabric data and the fibre material properties

4.1.2.1   Dispersion of Diamond Powder on the Dry Fabric

Fabrication of woven fabric composite plates was performed at the Institute for Composite Materials (IVW), Kaiserslautern. The vacuum assisted resin infusion technique was used to fabricate the composite plate. Five layers of 2/2 twill fabric with an areal weight as specified in Table 8 were used for fabrication of specimens and this related to fibre volume fraction of $55\,\%$. The average dimensions of the composite specimens were 70 mm long, 70 mm wide and 2 mm thick. In this technique diamond powder filler was deposited on the woven carbon fibre fabric prior to impregnation. Figure 24 a-c shows the stages of deposition of diamond powder in every layer of the dry fabric. Epoxy resin mixture was degassed for 20 minutes to remove air bubbles. Vacuum assisted resin infusion was performed (Figure 24 d) and the composite was cured in an autoclave at a static pressure of 24 bar close to 9 hours (Figure 24 e). One Sample

---

[‡‡]Areal Weight of a Fabric $A_F = 2 * N_f * N_T * \pi * r_f * \rho_f$
N_f is number of filaments per tow ; N_T is number of tows in unit width of fabric ; r_f is radius of the fibre cross-section and ρ_f is density of the fibre

without diamond powder and one sample with 14% volume fraction of diamond powder in the composite were prepared (Table 9).
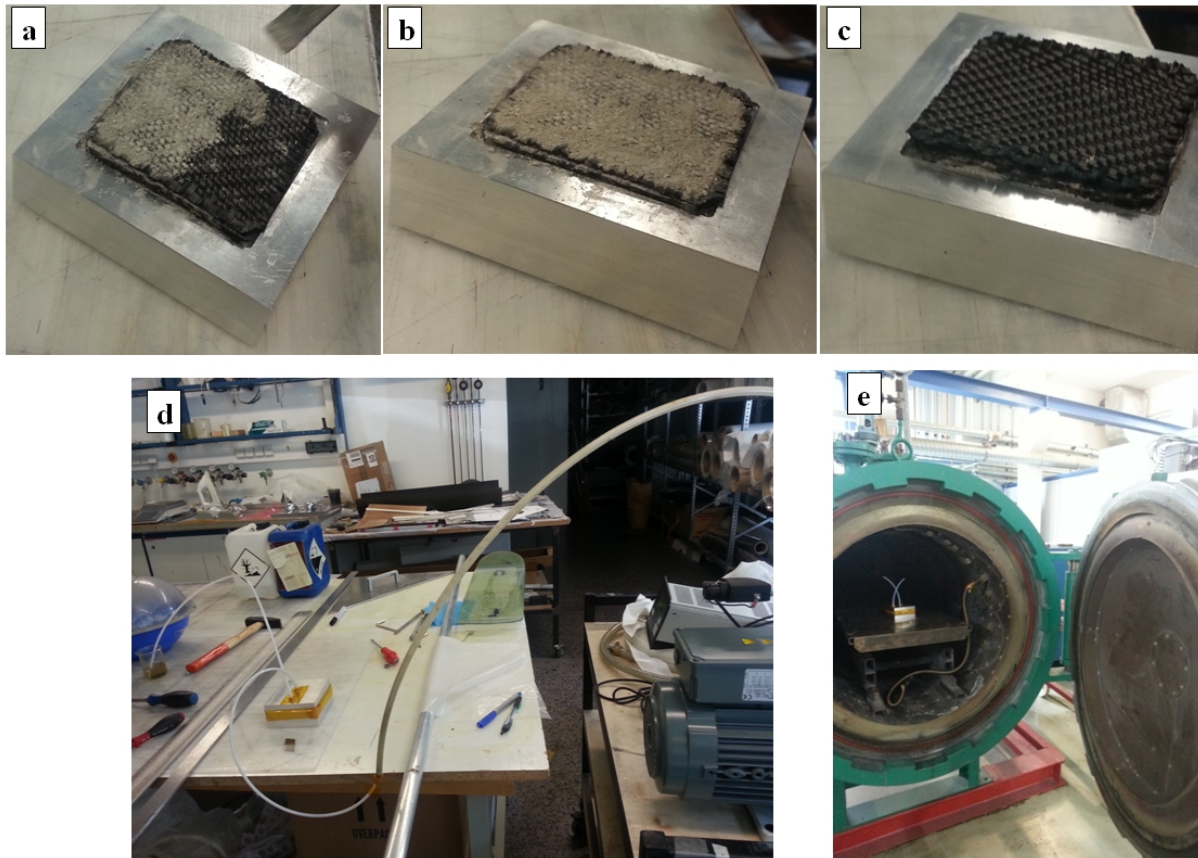
FIGURE 24: Deposition of diamond powder on woven carbon fibre fabric(a-c), Vacuum assisted resin infusion(d), Curing in an autoclave(e)

4.1.2.2 Matrix Modification Technique

Five different types of T300 composite plates were produced with this technique. Four layers of 2/2 twill fabric with an area weight and ply thickness as specified in Table 8 were used for fabrication of specimens and this related to a fibre volume fraction of $44\,\%$. The average dimensions of composite specimens were similar to that reported in the previous technique.

The first type of the sample was prepared without the diamond powder and the resin mixture was infused by vacuum into carbon fabric during the impregnation process. The remaining four samples were prepared by incorporating diamond powder of different fractions (Table 9) into the epoxy. A vacuum assisted hand layup technique was applied and the samples were cured in an autoclave.

In the same way, the high modulus YS90A samples were also produced where twenty six layers of plain weave fabric (Table 8) were used for fabrication of specimens. The average dimensions of YS90A composite specimens were 200 mm long, 250 mm wide and 3 mm thick. One sample

without and two other samples with the diamond powder of different fractions as listed in Table 9 were prepared.

Sample Number	Sample Thickness (mm)	Composite	Fibre Volume Fraction(%)	Diamond Powder Volume Fraction (%)	Epoxy Volume Fraction (%)
1	2	T300	55	0	45
2	2	T300	55	14	31
3	2	T300	44	0	56
4	2	T300	44	0.8	55.2
5	2	T300	44	1.6	54.4
6	2	T300	44	3	53
7	2	T300	44	8	48
8	3	YS90A	50	0	50
9	3	YS90A	50	6	44
10	3	YS90A	50	12	38

TABLE 9: Details of the diamond powder contents in the samples [63]

4.1.2.3   Thermal conductivity measurements

Steady state through the thickness thermal conductivity measurements were performed with a measuring cell built in-house at the Institute of Polymer Technology at the University of Applied Sciences, Kaiserslautern according to ASTM E1225-04 allowing measurements of circular samples with a diameter of 50 mm at thicknesses from 2 to 50 mm [66, 67, 68].

Water-jet cutting was used to prepare spherical specimens of 50 mm diameter, 3 mm thickness for the high modulus YS90A composite specimens (Figure 25) and 2 mm thickness for the standard modulus T300 fibre specimens (Figure 25).
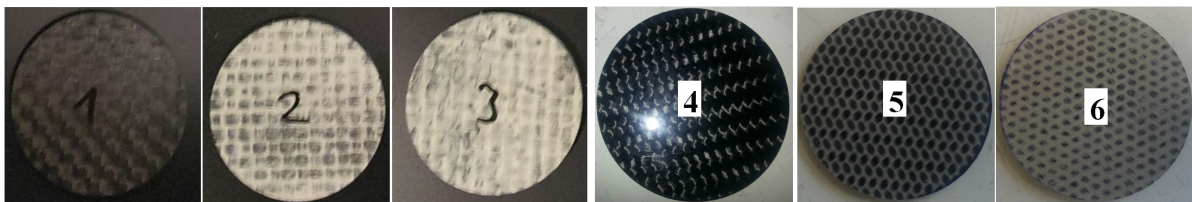
FIGURE 25: Composite samples of 50 mm diameter after water-jet cutting : YS90A composite samples without DP (1), with DP volume fractions of 6% (2) and 12% (3) in the composite. T300 composite (fibre volume fraction of 44 %) samples without DP (4), with DP volume fractions of 0.8% (5) and 3% (6) in the composite [63]

The measuring cylinder shown in Figure 26 consisted of four individual components namely the outer cylinder, insulating cylinder, meter bar and a cooling plate with a sample holder connected

to the bottom of the measuring cylinder. The outer cylinder was connected to a voltage device through which output A of the outer cylinder was controlled, the meter bar was controlled by output B of the voltage device. Four thermistors were used for the temperature measurement at the meter bar and the heating was provided through a cartridge heater in the top meter bar. The height of the two bars ΔZ including the sample is about $250\,\text{mm}$. Three thermistors in the top meter bar were used to measure the temperatures T_1, T_2 and T_3 and the temperature T_4 was measured by the thermistor in the bottom meter bar which contacted a cool plate to provide a heat sink with a constant temperature of $20\,^\circ\text{C}$ beneath the bottom plate.

The top meter bar was made of stainless steel (thermal conductivity of $K_{bar} = 16.2\,\text{W}\,\text{m}^{-1}\,\text{K}^{-1}$) and it was insulated with foam and additionally shielded by a guard heater (Figure 26) to prevent the radial heat loss. Conductivity paste (OMEGATHERM®201 with a thermal conductivity of $2.3\,\text{W}\,\text{m}^{-1}\,\text{K}^{-1}$) and a weight of $1.5\,\text{g}$ was weighed twice and was applied on each side of the sample in order to facilitate coupling and to reduce interfacial thermal resistance between meter bars and samples. All the thermistor informations were evaluated by a LabView® based program [63, 68, 69].
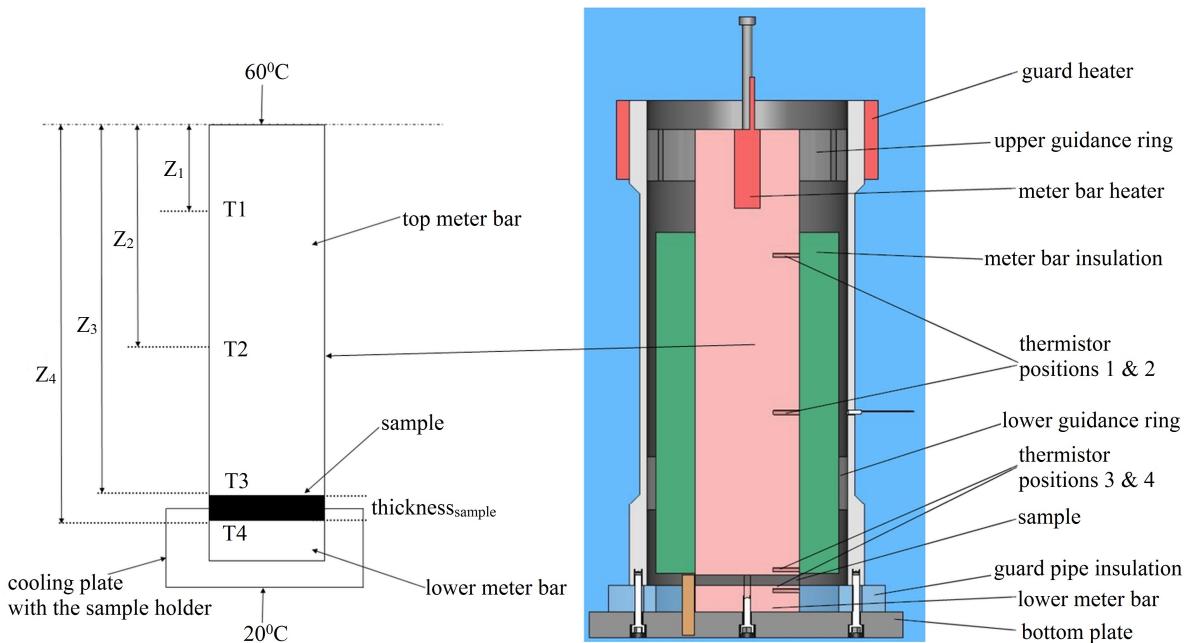
FIGURE 26: Measurement Setup with the Sample [63]

Calibration measurements were performed on isotropic specimens to determine the accuracy of the measuring cell [68]. The materials (like steel, stainless steel, aluminum, polyamide) with known thermal conductivities were measured and the matches were almost perfect with the [68] and the uncertainties were less than $\pm 3\,\%$.

The thermal resistance R_{int} at the interfaces from the meter bars and the sample was determined to be $0.000\,415\,079\,8\,\text{K}\,\text{m}^2\,\text{W}^{-1}$. Once the calibration measurements were completed,

the samples were tested and the out of plane thermal conductivity of the composite ($K_{\perp_{Test}}$) was calculated by the LabVIEW® (using Equation 4.9). More information on Equation 4.9 is given in Appendix A (Equations A.1 - A.7)

The temperatures measured by the thermistors for the T_1, T_2, T_3 and T_4 were averaged to 60°, 51°, 40° and 32° respectively. The test was repeated at least four times in order to obtain the mean value of out of plane thermal conductivity of the composite which are reported in the results and the typical percentage uncertainty (based on the standard deviation) of the measurement data for the standard modulus (T300) and the high modulus (YS90A) composite specimen was 0.71 % and 1.06 %.

$$K_{\perp_{Test}} = \frac{thickness_{sample}}{\dfrac{T_4 - T_3}{T_2 - T_1} * \dfrac{Z_2 - Z_1}{K_{bar}} - R_{int}} \tag{4.9}$$

4.1.3   Results and Discussion

4.1.3.1   T300 Composite

4.1.3.1.1   44% Fibre volume fraction

The experimental results of T300 woven composite with fibre volume fraction of 44% (Figure 27, Table 10) indicated that the effect of diamond powder up to 8% volume fraction was not significant and the out of plane thermal conductivity ($K_\perp$) of the composite increased from $0.67\,\mathrm{W\,m^{-1}\,K^{-1}}$ to $0.76\,\mathrm{W\,m^{-1}\,K^{-1}}$. The content of epoxy was higher than the fibre and diamond powder in the samples and epoxy being an insulator inhibited the fibre-diamond powder filler interaction and filler-filler interaction.
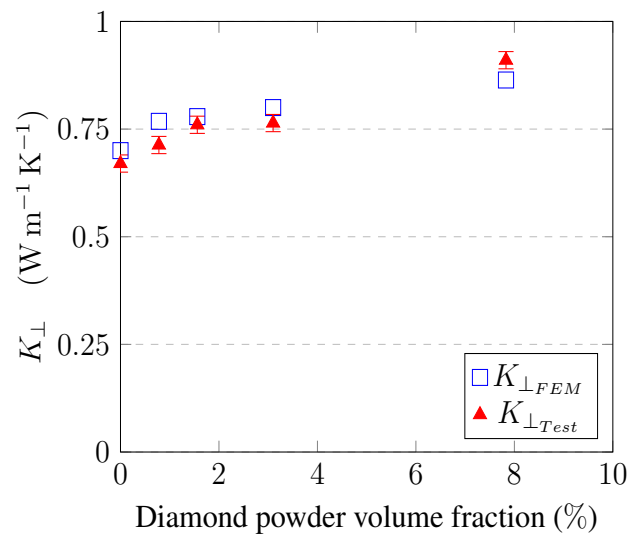

FIGURE 27: Enhancement of the $K_\perp$ of the T300 composite filled with the DP

Fair agreement was observed between the FEM and measurement results. The FEM results as shown in Figure 27 and in Table 10 also predicted the lack of improvement in $K_\perp$ at lower diamond powder content. The distance between the inter-filler (diamond powder-diamond powder) and filler-fibre distance were larger at lower diamond powder content and the isolated diamond powder particles did not show any significant effects towards a thermal conductivity improvement and it also resulted in a lack of formation of conductive paths. At 8% diamond powder volume fraction (Figure 27, Table 10), experimental and FEM results predicted a linear increase in $K_\perp$. With higher epoxy content and even when diamond powder content was increased, the increase in thermal conductivity was again not significant.

T300 fibre volume fraction (%)	DP volume fraction in the composite (%)	$K_\perp (\mathrm{W\,m^{-1}\,K^{-1}})$		Improvement (factor)	
		FEM	Measurement	FEM	Measurement
44	0	0.7	0.67±0.002056	1	1
44	0.8	0.77	0.71±0.000854	1.1	1.06
44	1.6	0.78	0.76±0.001315	1.1	1.13
44	3	0.8	0.764±0.002869	1.14	1.13
44	8	0.86	0.91±0.007157	1.23	1.36

TABLE 10: Comparison of the FEM and experimental results of the T300 composite

4.1.3.1.2 55% Fibre volume fraction

The experimental thermal measurements were only conducted for the samples without DP and with 14% volume fraction of DP in the composite (Figure 28). The measurements showed an increase in the out of plane thermal conductivity ($K_\perp$) from $0.8\,\mathrm{W\,m^{-1}\,K^{-1}}$ (without DP) to $1.85\,\mathrm{W\,m^{-1}\,K^{-1}}$ with 14% volume fraction of DP. A detailed finite element modelling was conducted to understand the increase in the $K_\perp$.

FEM results as shown in Figure 28 and in Table 11 also explains the physical phenomenon of a lack of conductive path formation up to 1.4% volume fraction of DP in the composite. From 3% to 14% volume fraction of DP, there was an effect of a rapid increase in thermal conductivity. The FEM simulation considered two step (homogenisation) process by which, an increase in the volume of diamond powder reduced the inter-diamond filler distance which enhanced the polymer thermal conductive path.

With the increase in DP content, the fibre-diamond filler distance also reduced, which increased the network of conductive path for the composite. When the DP volume content increased,

interaction between the fibre and DP accelerated. This led to the formation of additional conductive paths. The number of contact points between the diamond powder filler and the fibres in the microstructure increased due to a homogeneous dispersion of diamond powder in the composite leading to a rapid increase in the $K_\perp$. An agreement in both FEM and measurements could be seen from the results with 14% volume fraction of DP in the composite, where the $K_\perp$ increased by factors of 2.57 (FEM) and 2.3 (experimental) respectively. More detailed explanation of conductive path formation in a composite with DP are given in 4.1.3.3.
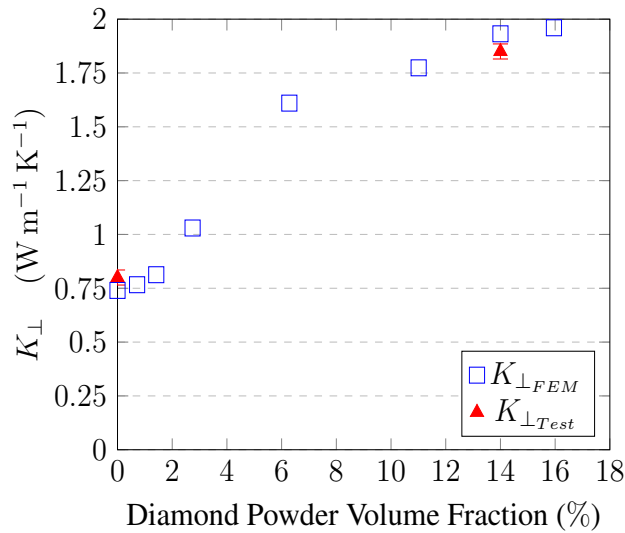
FIGURE 28: Comparison of FEM and experimental results for $K_\perp$ of T300 composite (55% fibre volume fraction) filled with the DP

T300 fibre volume fraction (%)	DP volume fraction in the composite (%)	$K_\perp(\mathrm{W\,m^{-1}\,K^{-1}})$		Improvement (factor)	
		FEM	Measurement	FEM	Measurement
55	0	0.74	0.8±0.002		
55	0.7	0.77		1.04	
55	1.4	0.8		1.08	
55	3	1		1.35	
55	6	1.6		2.16	
55	11	1.78		2.4	
55	14	1.9	1.85±0.0044	2.57	2.3
55	16	1.96		2.65	

TABLE 11: $K_\perp$ of the T300 composite filled with DP

A SEM image (prepared by Mr. Uwe Schmitt, IVW Kaiserslautern) as shown in Figure 29 represents the behaviour of fibre-filler and filler-filler interaction at higher content (14% volume

fraction) of DP which influence the formation of thermal interface in the composite (marked in red in Figure 29).
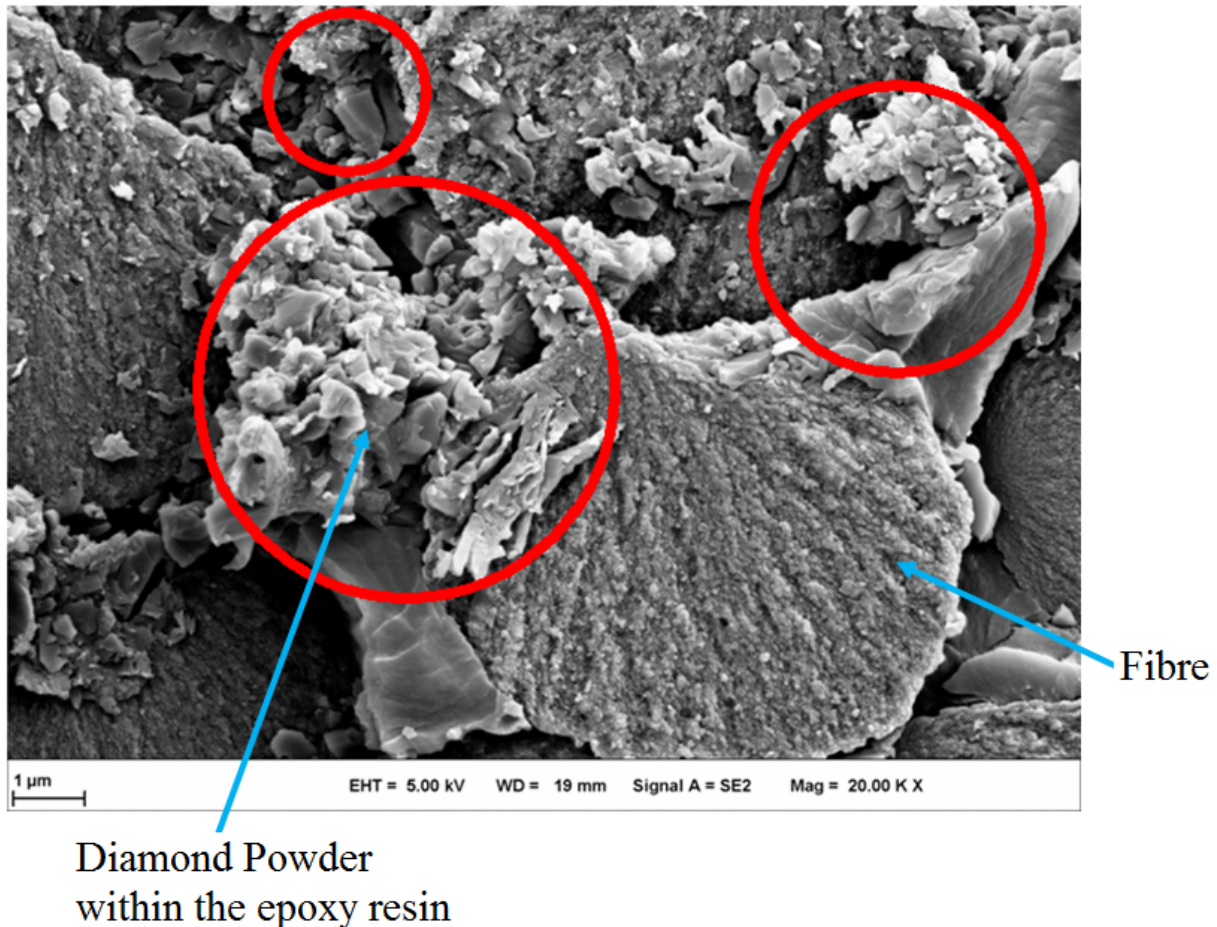
FIGURE 29: SEM image showing fibre-diamond filler epoxy matrix forming the thermal interface (marked in red) in T300 composite (55% fibre volume fraction) with 14% volume fraction of diamond powder

The behaviour predicted by the FEM result after 14% volume fraction content of diamond powder showed a saturation, where with the further increase in the filler content, the influence was not significant (Figure 28, Table 11) where the thermal conductivity of the fibres determine the overall thermal conductivity of the composite.

The effective conductive path formation by diamond powder becomes nullified even by increasing the content of diamond powder. This saturation point has been reported by Shan-Tung Tu et al. as a physical property ratio which happens with the increase of volume fraction of the fillers and beyond this saturated ratio, the physical properties of the composites cannot be further improved by enhancing the corresponding property of the matrix material [70].

4.1.3.2 YS90A Composite

The influence of DP towards the $K_\perp$ was again minimal at volume contents below 5% in the YS90A composite . This phenomenon could be seen from the experimental and FEM results in Figure 30. From 6% volume fraction content of DP in the composite, there was a rapid increase in in the $K_\perp$. This steep increase remained until 12% volume fraction of DP in the composite. An increase in the conductive path formation was observed. The measurement as well as the FEM predicted this steep increase (Figure 30 and Table 12) which led to an increase in through the thickness thermal conductivity upto $2.69\,\mathrm{W\,m^{-1}\,K^{-1}}$(Test) and $2.3\,\mathrm{W\,m^{-1}\,K^{-1}}$(FEM).
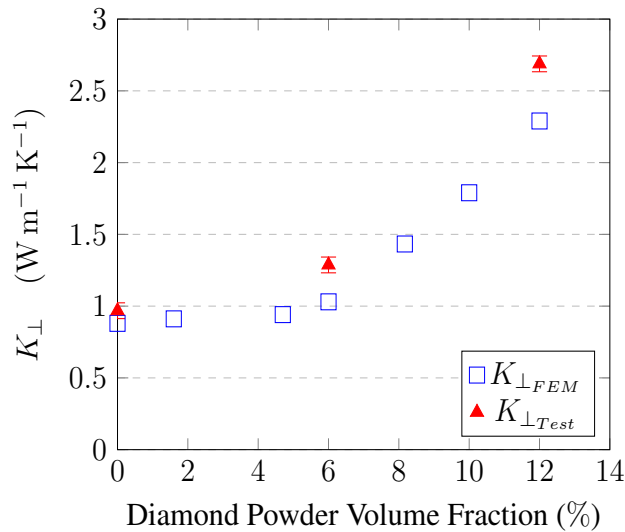
FIGURE 30: FEM and Experimental results comparison of diamond powder filled YS90A composite (50% fibre volume fraction)

YS90A fibre volume fraction (%)	DP volume fraction in the composite (%)	$K_\perp(\mathrm{W\,m^{-1}\,K^{-1}})$		Improvement (factor)	
		FEM	Measurement	FEM	Measurement
50	0	0.88	0.97±0.0081	1	1
50	2	0.91		1.03	
50	5	0.94		1.07	
50	6	1.03	1.29±0.00905	1.17	1.33
50	8	1.43		1.63	
50	10	1.8		2.05	
50	12	2.3	2.69±0.001275	2.6	2.8

TABLE 12: Out of plane thermal conductivity ($K_\perp$) of the YS90A composite

4.1.3.3 Conductive path formation in the composite

A statistical analysis was performed in order to evaluate the ability of the composite to form clusters of thermally conductive paths in the FEM model. These paths are observed to be based on the distances and the interactions between the fibre-fibre and diamond filler-fibre. In order to find the increase in the conductive path, it would be necessary to determine the average distance between the neighbouring fibres and diamond filler within the RVE. The FEM model for the high modulus YS90A composite was taken as a reference. The distribution of nearest neighbour distance is generally evaluated using the probability density function (PDF), which defines the frequency of a random distance. The PDF of nearest neighbour distance was formed, in order to determine the short distance interaction between fibre-fibre and fibre-DP-fibre and also to determine whether the distance pattern shows some degree of clustering.

It could be seen from Figure 31, the nearest neighbour distance of the numerically generated microstructure of 50 vol% fibre and 6 vol% diamond powder shows a relatively lower probability density at a higher distance, while the nearest neighbour distance for the microstructure with 12 vol% diamond powder (Figure 32) shows a relatively higher probability density at a shorter distance. For the microstructure with 12 vol% diamond powder, the nearest neighbour distances are very close to a peak as a result of clustering of diamond filler between the neighbouring fibres.
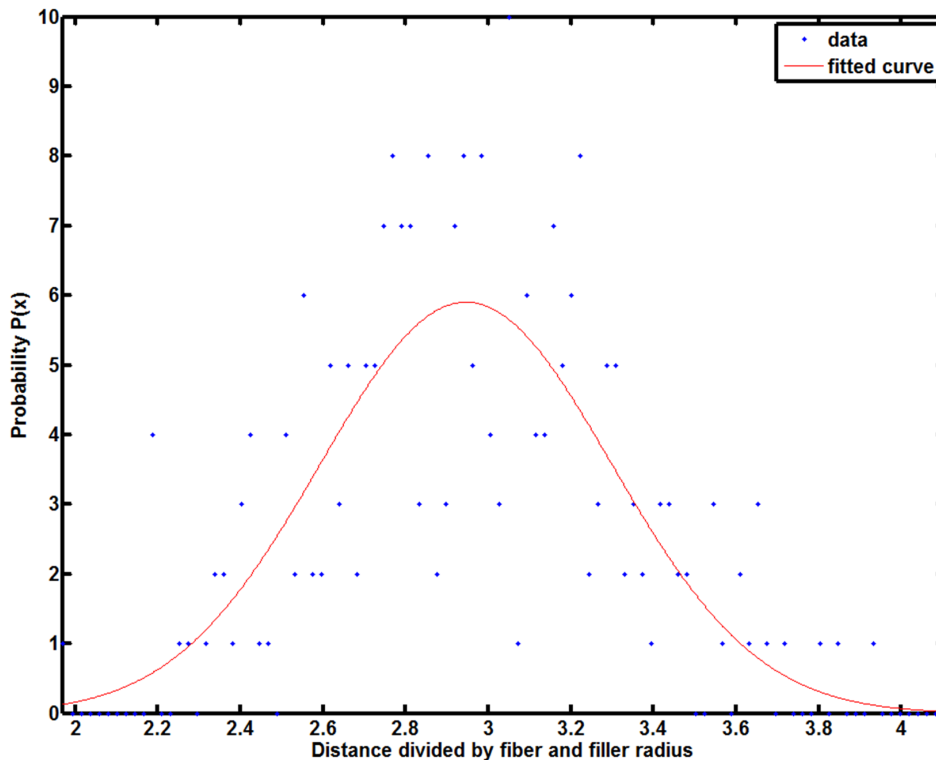
FIGURE 31: Nearest neighbour distance function for the numerically generated microstructure of the YS90A composite with the diamond powder of 6 vol%
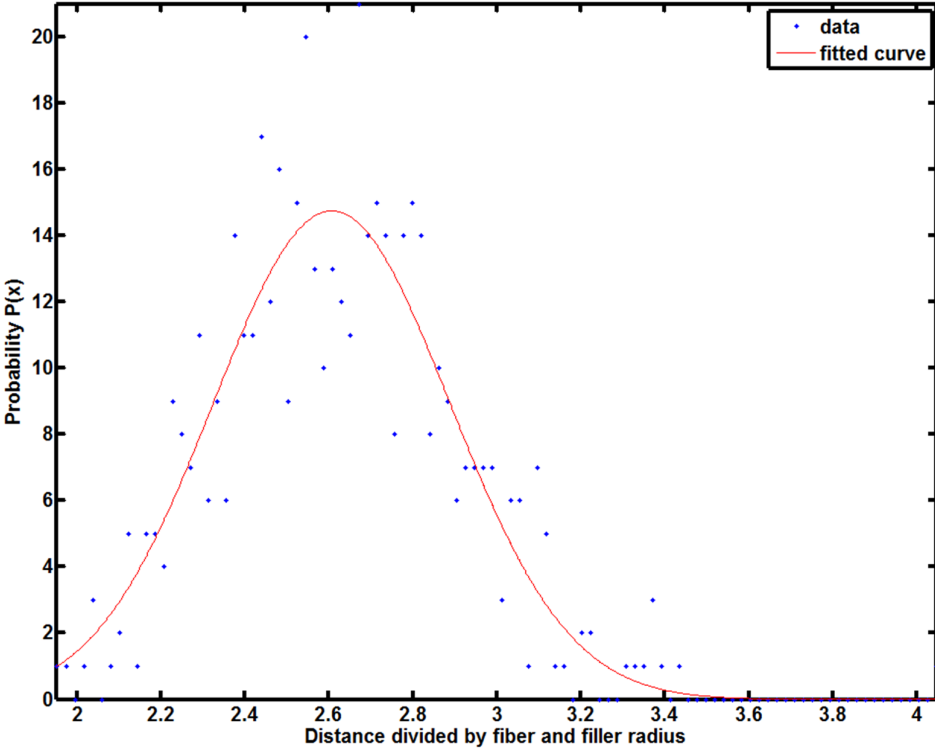
FIGURE 32: Nearest neighbour distance function for the numerically generated microstructure of the YS90A composite with the diamond powder of 12 vol%

For a randomly generated microstructure as shown in Figure 33, the heat conduction and the conductive chain formation are dominated by the fibres when they are in close contact with the neighbouring fibres and the diamond powder filler influences as a catalyst to form additional conductive path when they are in close contact between the fibres.
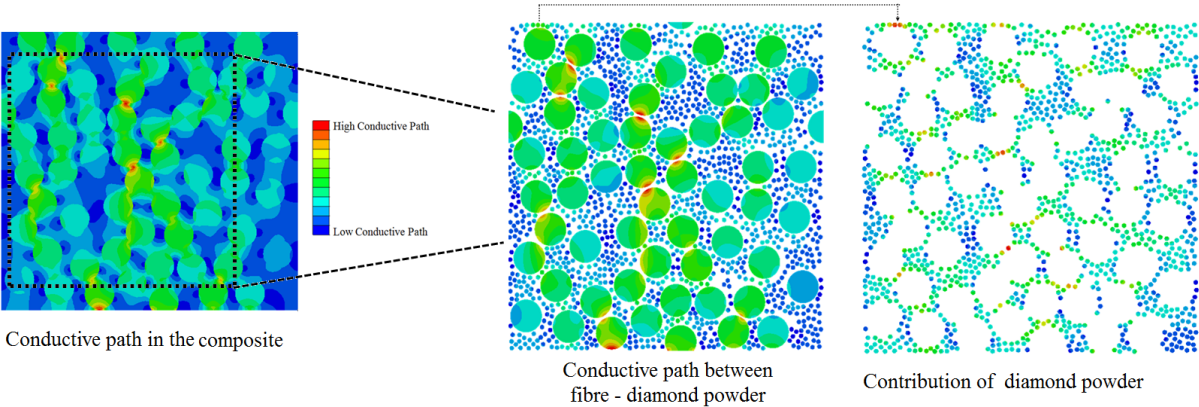
FIGURE 33: FEM model for conductive path formation in YS90A composite with diamond powder of 12 vol% (c)

To further emphasize the behaviour of fibre-fibre interaction and fibre-diamond filler interaction, a periodic distribution of YS90A fibres within a RVE along with diamond powder (12% volume fraction) are shown in Figure 34. Even though it would be unrealistic to have a periodic

distribution of fibres in the real composite, the behaviour shown in Figure 34 explains that when fibres are aligned in close thermal contact with the neighbouring fibres and when the diamond fillers are between the fibres, then the heat conduction would be much higher than the randomly generated microstructures (Figure 33). The significance of heat conduction remains sensitive to the distance between neighbouring fibres and diamond powder. Physically this means that, if a better dispersion of diamond powder could be achieved the results would be further enhanced. For better dispersion, the size and the volume content of the diamond powder are important as it influences the viscosity of the resin. In terms of fabrication of the samples with the microscale diamond powder, the uniform dispersion was limited due to the high viscosity of the diamond filled resin and the samples had to be fabricated by the hand layup technique.
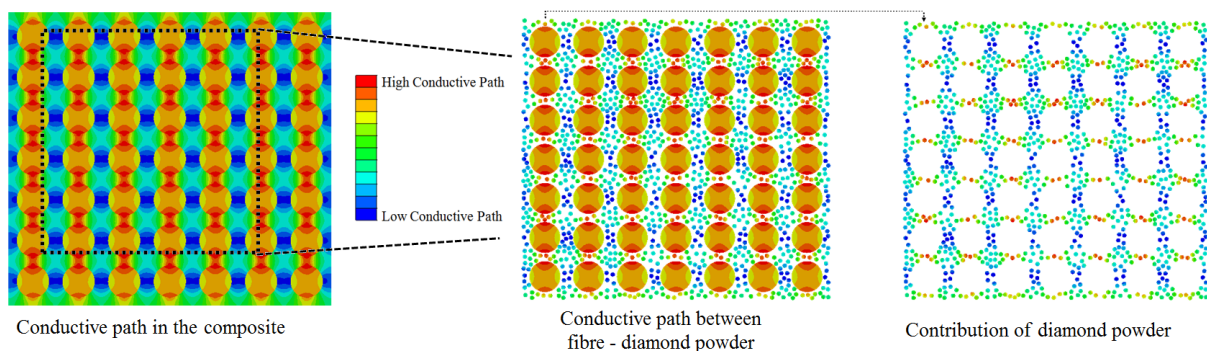
FIGURE 34: An example of heat conduction in the YS90A diamond powder filled (12 vol%) composite with periodic fibre distribution

4.1.4 Summary

In this investigation, the out of plane thermal conductivity ($K_\perp$) of the standard modulus (T300) and the high modulus (YS90A) woven composites were examined by FEM and thermal measurements. FEM investigations with higher diamond powder contents showed the formation of conductive contact points through interaction with fibres which improved the thermal transport. Current experimental investigations by dispersing DP on the dry fabric showed that the $K_\perp$ of the T300 composite increased by a factor of 2.3 for 55% fibre volume fraction - 14% diamond powder volume fraction. Experimental investigation via the matrix modification technique showed that the through the thickness thermal conductivity of the YS90A composite increased by a factor of 2.8 with 50% fibre volume fraction - 12% diamond powder volume fraction. The results showed that the thermal conductivity of the composites depends significantly on the fibre and diamond powder filler volume fraction. These results yield much value when compared to those reported in literature (as mentioned in 3.1.6, where complex fabrication techniques were carried out in order to functionalise (chemically alter) the filler. The above improvement in the $K_\perp$ using DP can benefit several composite applications. The improvement in the $K_\perp$ would directly benefit the development of new stave designs with the DP filled carbon fibre pipe, as the new stave would benefit from a much enhanced heat transfer behaviour.

4.2   Elastic and Failure Behaviour

With the improvement of thermal behaviour of composites with DP, it is necessary to investigate the influence of DP towards the elastic and failure properties. The objectives (Figure 35) of this study were :

- To predict the elastic properties of the epoxy-diamond powder matrix through a homogenisation method.

- To develop a micromechanical unit cell model in order to predict the elastic properties of the DP filled T300 and YS90A woven composites.

- To develop a numerical model in order to evaluate the on-axis tensile and bending behaviour of DP filled T300 and YS90A woven composites through a progressive damage modelling technique.
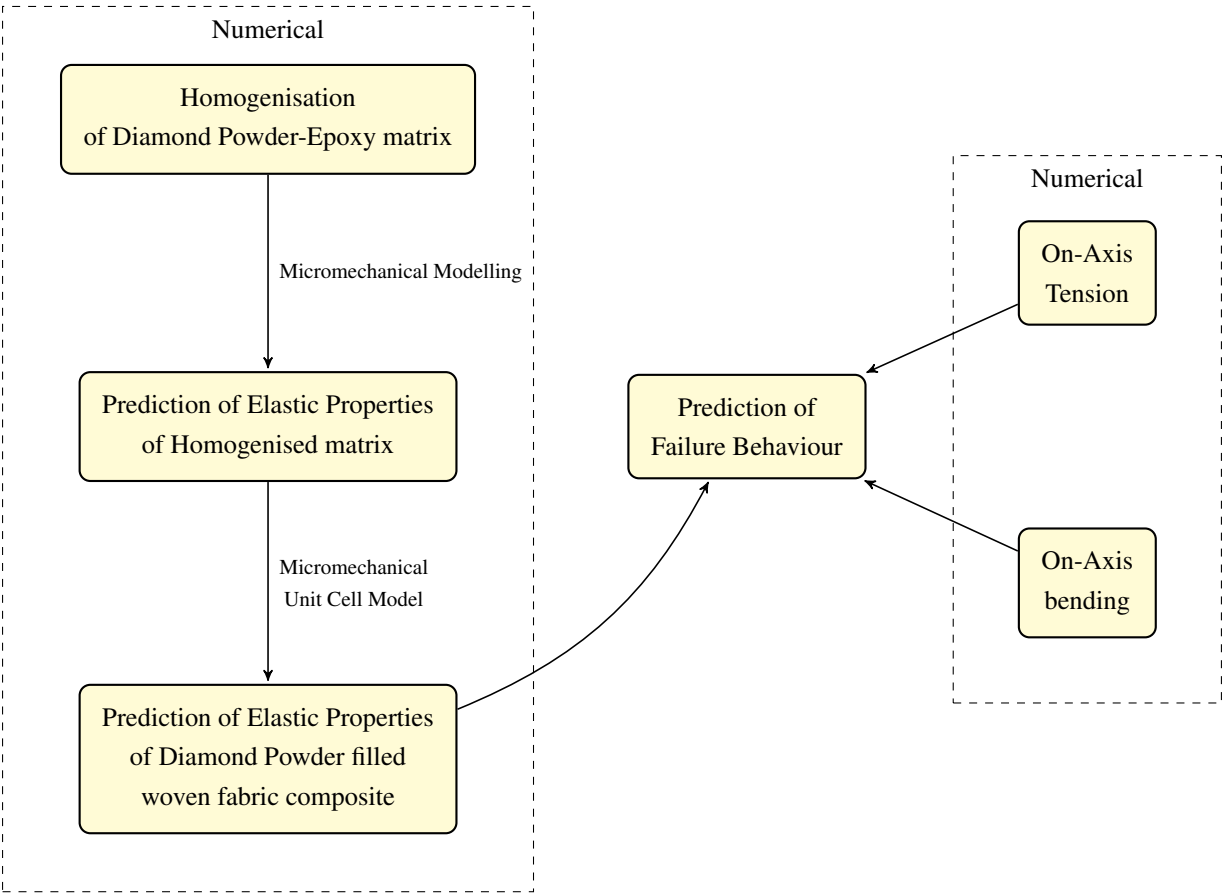

FIGURE 35: Work Flow

4.2.1   Homogenisation of Heterogeneous Matrix Microstructure

The macro response of the epoxy-diamond powder matrix was calculated from the micro response through numerical homogenisation. The mechanical properties of a micro heterogeneous matrix material were characterized by a spatially variable elasticity tensor C. Generally,

in order to demonstrate the homogenised effective macroscopic response of such materials, the relation between averages are described as shown in the following :

$$\langle \sigma \rangle_\Omega = \mathbf{C} \langle \epsilon \rangle_\Omega \tag{4.10}$$

where $\mathbf{C}$ is defined as the effective property which is the elasticity tensor used in structural scale analysis. $\langle \sigma \rangle_\Omega$ and $\langle \epsilon \rangle_\Omega$ are the volume average stress and strain tensor fields within a statistically Representative Volume Element (RVE) of volume $|\Omega|$. The two phases considered in the matrix here are epoxy (m) and diamond powder filler (d) which are denoted by volume fraction as V_m and $V_d = 1 - V_m$. The constitutive equations for the volume average stress and strain tensors can be denoted as

$$
\begin{aligned}
\langle \sigma \rangle^d &= \frac{1}{V_d} \int_{V_d} \sigma dV \\
\langle \epsilon \rangle^d &= \frac{1}{V_d} \int_{V_d} \epsilon dV
\end{aligned}
\tag{4.11}
$$

$$
\begin{aligned}
\langle \sigma \rangle^m &= \frac{1}{V_m} \int_{V_m} \sigma dV \\
\langle \epsilon \rangle^m &= \frac{1}{V_m} \int_{V_m} \epsilon dV
\end{aligned}
\tag{4.12}
$$

The total averaged stress and strain tensors defined by the rule of mixtures is then given by

$$
\begin{aligned}
\langle \sigma \rangle &= V_d \langle \sigma \rangle^d + V_m \langle \sigma \rangle^m \\
\langle \epsilon \rangle &= V_d \langle \epsilon \rangle^d + V_m \langle \epsilon \rangle^m
\end{aligned}
\tag{4.13}
$$

The homogenised effective elastic modulus of diamond powder filled polymer matrix composite was obtained by finite element analysis with a 2D RVE consisting of randomly distributed spherical diamond powder fillers. An algorithm as specified in the section 4.1.1 was used to generate the fillers content up to 25% of volume fraction and the effective elastic properties of the composite were predicted from the properties of their constituents. Both diamond powder filler and epoxy matrix were considered to be isotropic materials with Young's modulus and Poisson's ratio given as $E_d = 1000$ GPa, $\nu_f = 0.3$ and $E_m = 3.5$ GPa, $\nu_m = 0.35$, respectively. Python scripts were used to generate RVE's in the commerical code ABAQUS® and were meshed with 4-node bilinear plane strain quadrilateral elements with reduced integration CPE4R. Periodic boundary conditions (PBC) were then applied to the RVE. The PBC are a set of boundary conditions that are normally used when the physical geometry of interest and the expected pattern of the solutions have a periodically repeating nature. They can be used to simulate a bulk material by modelling a finite RVE [71]. For the RVE shown in Figure 36, the PBC were applied to the RVE to ensure a macroscopically uniform stress or displacement field

for tension and shear load (Equation 4.14 - 4.15 [72]).

$$u_{\overline{BC}} - u_B = u_{\overline{AD}} - u_A \tag{4.14}$$

$$u_{\overline{DC}} - u_D = u_{\overline{AB}} - u_A \tag{4.15}$$

where u is the displacement vector of any node on the boundary. The subscripts A, B and D corresponds to the vertex. AB, BC AD and DC correspond for the edge between the two vertices (Figure 36). The PBC's were implemented in the form of equations using the constraint option in ABAQUS® through a python script.
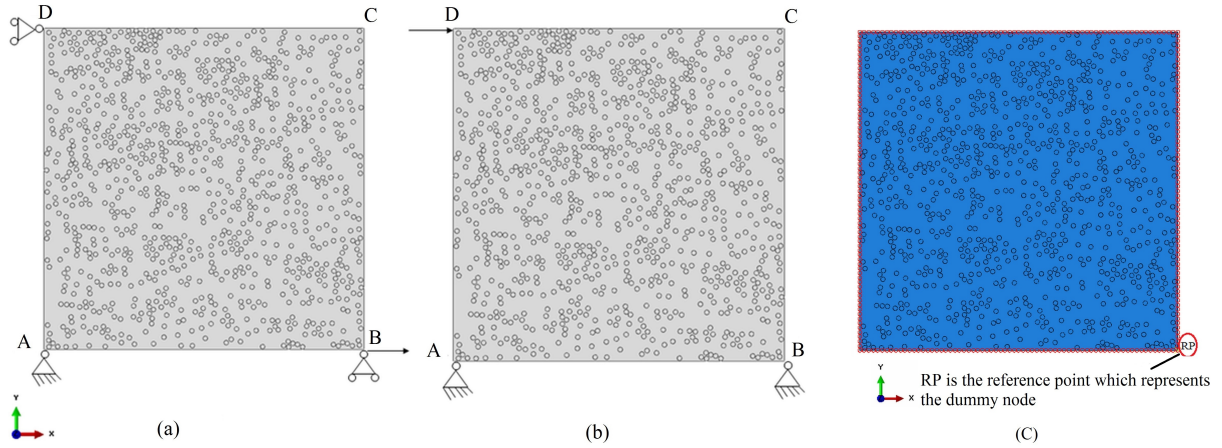
FIGURE 36: Representation of the Periodic Boundary Condition in tensile (a) and shear (b) loading scenarios

4.2.1.1   PBC as constraint equations in ABAQUS®

A general linear homogeneous equation is defined as follows

$$A_1 u_i^P + A_2 u_j^Q + \cdots + A_N u_k^R = 0 \tag{4.16}$$

where R is the node, k is the degree of freedom and A_N is a constant coefficient that define the relative motion of the nodes [71]. In order to apply the PBC using the constraint equations as described in Equation 4.16, a dummy node was introduced in ABAQUS®. In Equation 4.16, zero on the right side of the equation would be replaced by a nonzero value

$$A_1 u_i^P + A_2 u_j^Q + \cdots + A_N u_k^R = \hat{u} \tag{4.17}$$

where $\hat{u}$ is the displacement vector. In ABAQUS®, the prescribed $\hat{u}$ was applied through a dummy node, I, which was not attached to any other part in model. A reference point (Figure 36 (c)) with arbitrary coordinates were defined to represent the dummy node. This node was specified as a boundary condition with the value $\hat{u}$ in a certain direction, as shown in Equation 4.18 where n is the direction of the prescribed displacement.

$$A_1 u_i^P + A_2 u_j^Q + \cdots + A_N u_k^R - \hat{u}_n^I = 0 \tag{4.18}$$

A load step was defined in order to apply the prescribed displacement $\hat{u}$ as a boundary condition. The homogenisation scheme as shown in Equations 4.19, 4.20 was implemented with the volume averaged stress and strain calculated in each elements in order to predict the effective elastic properties of diamond powder filled polymer matrix composites.

$$E = \frac{\sum_{i=1}^{n} \sigma^i A^i}{\sum_{i=1}^{n} \epsilon^i A^i} \tag{4.19}$$

$$G = \frac{\sum_{i=1}^{n} \tau^i A^i}{\sum_{i=1}^{n} \gamma^i A^i} \tag{4.20}$$

where E is the elastic modulus and G is the shear modulus. n is the total number of elements in the model. σ^i and ϵ^i are the average component of stress and strain calculated in each element respectively. A^i is the area of that element. The deformed shape of the RVE is shown in Figure 37. As expected, the diamond powder epoxy matrix became stiffer as the tensile and shear moduli increased with the increase in content of the diamond powder (Table 13).

Undeformed   Deformed
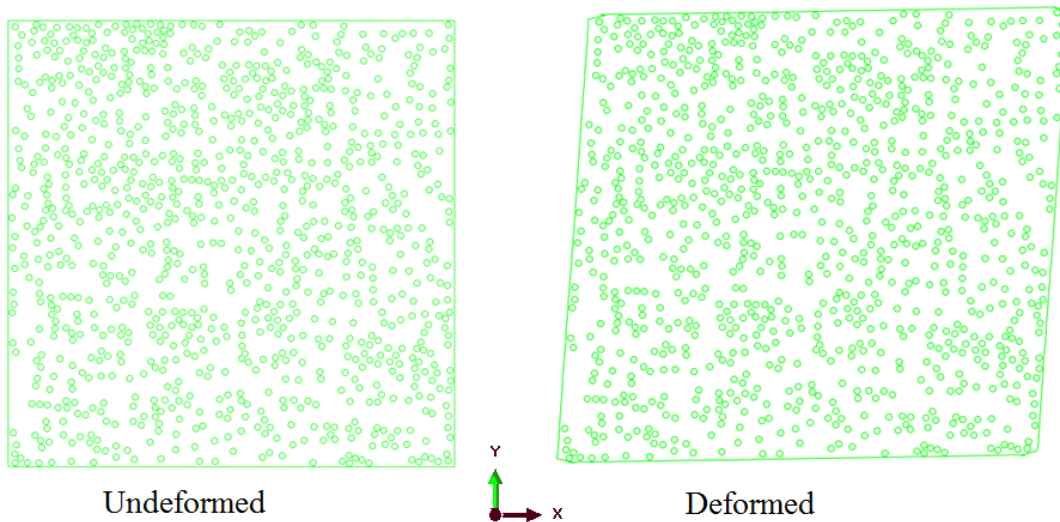
FIGURE 37: Deformed shape of the RVE subjected to the PBC

Diamond Powder Volume Fraction (%)	Elastic Modulus (GPa)	Shear Modulus (GPa)
0	3.5	1.01
10	4.68	1.53
15	5.05	1.64
25	7.8	2.55

TABLE 13: Predicted effective elastic properties of the diamond powder-epoxy
matrix through a numerical homogenisation technique

4.2.2 Prediction of Elastic Properties of Diamond Powder Filled Woven Composites

The prediction of macromechanical properties of T300 (55% fibre volume fraction) and YS90A (50% fibre volume fraction) woven composites filled with diamond powder were evaluated with the periodic unit cell structure through micromechanical method. The unit cell was modelled using TexGen® [73] by considering that the warp and weft yarns posses geometric and material similarities (Figure 38). The developed geometric models with the information of textile data (Table 14), fibre material data (Table 15) and mesh details were exported into ABAQUS® through an input file containing voxel based mesh details using 8 node 3D linear brick elements.
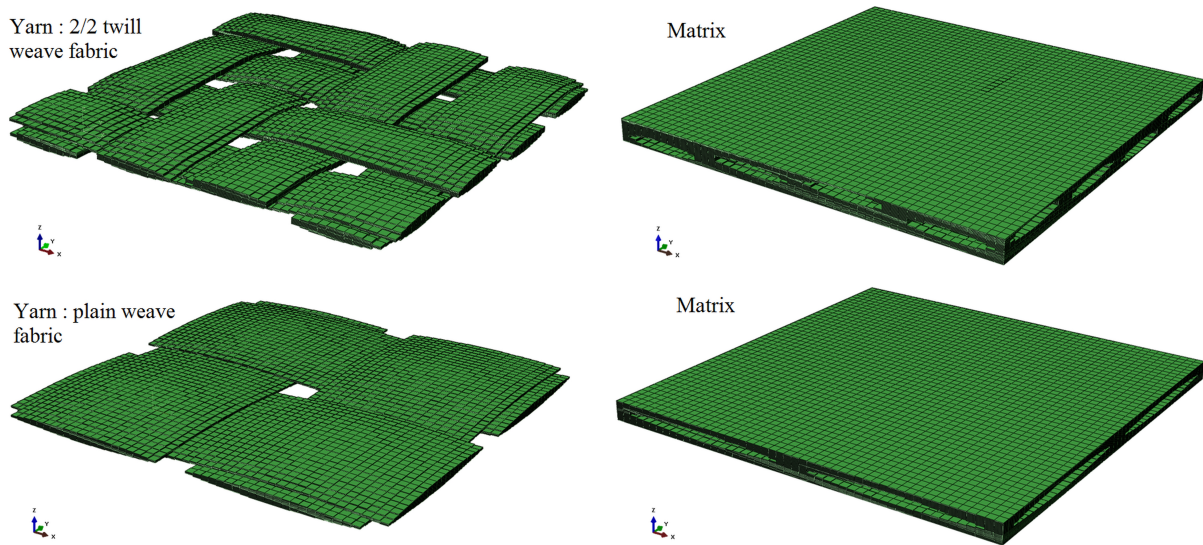
FIGURE 38: FEM Model developed in TexGen® with the 2/2 twill weave and plain weave fabrics

Weave Style	Weave Data						
	Yarn Spacing (mm)	Yarn Width (mm)	Fabric Thickness (mm)	Weft Yarns (mm)	Warp yarns (mm)	Length (mm)	Width (mm)
Twill	1	0.8	0.2	4	4	4	4
Plain	3.5	3	0.3	2	2	7	7

TABLE 14: TexGen® model data for T300 and YS90A fibre

Fibre	Elastic Properties					
	E_{11} (GPa)	E_{22} (GPa)	ν_{12}	ν_{23}	G_{12} (GPa)	G_{23} (GPa)
T300	231	40	0.27	0.3	24	10.7
YS90A	880	10	0.26	0.4	5	5

TABLE 15: T300[74] and GRANOC YS90A[75] fibre material data

The elastic properties of diamond powder filled polymer matrix which were predicted through numerical homogenisation in the previous section (Table 13) were applied to the TexGen® material data for predicting the macroscopic properties of woven composites.

The amount of DP were kept the same, as that reported in the thermal modelling section. The contents were limited to volume fractions of 14%, 25% in epoxy corresponding to 6% and 12% by volume fraction in the composite. The orthotropic behaviour of the yarns were defined by 3D stiffness matrix consisting of nine independent constants and are shown in Equation 29.

$$
\begin{bmatrix} \epsilon_x \\ \epsilon_y \\ \epsilon_z \\ \gamma_{xy} \\ \gamma_{xz} \\ \gamma_{yz} \end{bmatrix} = \begin{bmatrix} \dfrac{1}{E_x} & \dfrac{-\nu_{yx}}{E_y} & \dfrac{-\nu_{zx}}{E_z} & 0 & 0 & 0 \\ \dfrac{-\nu_{xy}}{E_x} & \dfrac{1}{E_y} & \dfrac{-\nu_{zy}}{E_z} & 0 & 0 & 0 \\ \dfrac{-\nu_{xz}}{E_x} & \dfrac{-\nu_{yz}}{E_y} & \dfrac{1}{E_z} & 0 & 0 & 0 \\ 0 & 0 & 0 & \dfrac{1}{G_{xy}} & 0 & 0 \\ 0 & 0 & 0 & 0 & \dfrac{1}{G_{xz}} & 0 \\ 0 & 0 & 0 & 0 & 0 & \dfrac{1}{G_{yz}} \end{bmatrix} \begin{bmatrix} \sigma_x \\ \sigma_y \\ \sigma_z \\ \tau_{xy} \\ \tau_{xz} \\ \tau_{yz} \end{bmatrix}
$$

$$(4.21)$$

The displacement boundary conditions for the unit cell have been defined following the procedures defined by Li et al [73]. As specified by Li et al [73] the unit cells were treated by using the translational symmetry transformation.

The macroscopic strains ϵ_x^0, ϵ_y^0, ϵ_z^0, γ_{yz}^0, γ_{xz}^0, γ_{xy}^0 in Equation 29 were treated as six extra degrees of freedom through which loads to the unit cell have been prescribed. Concentrated forces were applied to these degrees of freedom and effectively, macroscopic stresses were applied to the unit cell [73].

Periodic boundary conditions were applied in the form of equations for all the unit cells that can be implemented using an equation option in ABAQUS®. Uniaxial loads (F_x, F_y, F_z, F_{yz}, F_{xz}, F_{xy} and ΔT) were applied to the unit cell at any point in the cell defined as constraint driven point (Figure 39) assigned as x=0, y=1, z=2, xy=3, xz=4 and yz=5 in the analysis to obtain the elastic properties.
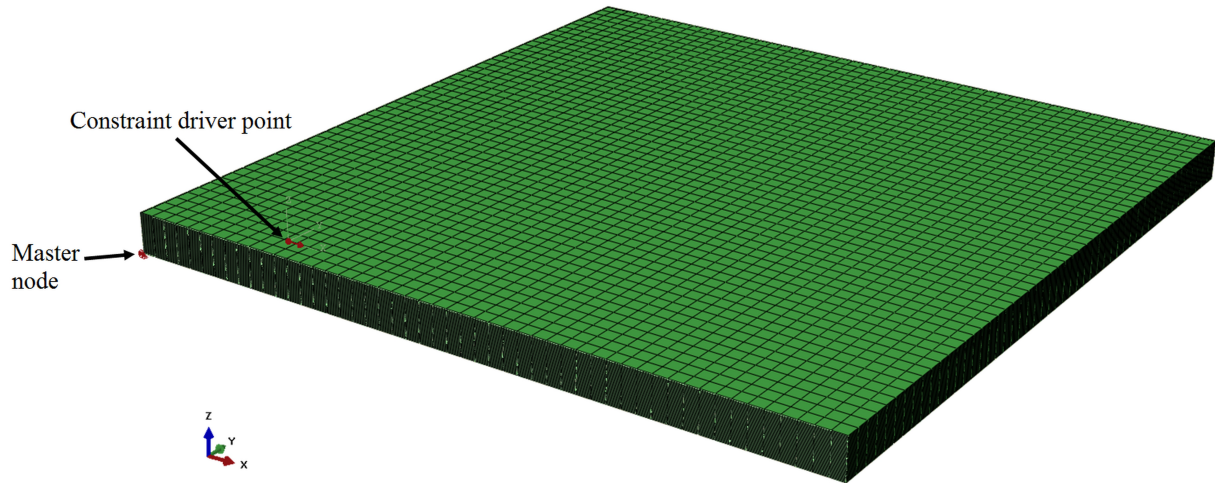
FIGURE 39: Assigning constraint driver point within the unit cell for applying the uniaxial loads

With the macroscopic stresses being expressed in terms of forces applied to the unit cell, the effective properties of the material represented by the unit cell were obtained in terms of the independent degrees of freedom (ϵ_x, ϵ_y, ϵ_z, γ_{yz}, γ_{xz}, γ_{xy}) and the applied loads (F_x, F_y, F_z, F_{yz}, F_{xz}, F_{xy} and ΔT) [73].

The predicted elastic properties of T300 and YS90A composites with and without diamond powder are listed in Table 16. The predicted results showed an increase in the overall mechanical properties of the composite, where the stiffer DP-epoxy matrix influences to increase those properties. These properties would be applied to the model for predicting the failure behaviour of the composite.

Results	Without DP		With 6 *vol* % DP		With 12 *vol* % DP	
	T300	YS90A	T300	YS90A	T300	YS90A
E_{11}(GPa)	67.25	216.64	69	221.7	71.7	227.94
E_{22}(GPa)	67.25	216.64	69	221.7	71.7	227.94
ν_{12}	0.12	0.13	0.12	0.11	0.11	0.09
$\nu_{23}=\nu_{13}$	0.42	0.47	0.43	0.47	0.44	0.49
G_{12}(GPa)	8.8	3.1	9.4	3.38	10.42	3.87
G_{23}(GPa)	4.6	2.76	5.5	3.2	6.9	3.81

TABLE 16: Predicted numerical elastic properties of the standard modulus T300 (55% fibre volume fraction) and the high modulus YS90A (50% fibre volume fraction) - diamond powder epoxy filled woven composites

4.2.3   Failure Behaviour under Tensile and Bending

4.2.3.1   Experimental tensile testing

The experimental testing (Figure 40) was only carried out for the high modulus YS90A composite filled with diamond powder in order to characterize the elastic properties of the composite filled with diamond powder under tensile loading.

Twenty six layers of the plain weave fabric (On-axis 0^0-90^0) with an areal weight of $125\,\mathrm{g\,m^{-2}}$ relating to a fibre volume fraction of 50 % were used for the fabrication of specimens. The first sample was prepared without DP and the resin mixture was infused via vacuum into the carbon fibre reinforcement fabric during the impregnation process. The remaining two samples were prepared by incorporating DP into the epoxy resin corresponding to DP volume fractions of 6 % and 12 % in the composite. A vacuum assisted hand layup technique was applied and the samples were cured in an autoclave at a static pressure of 24 bar for close to 9 hours. The average dimensions of the composite specimens were $200\,\mathrm{mm}$ long, $250\,\mathrm{mm}$ wide and $3\,\mathrm{mm}$ thick. Water-jet cutting was used to prepare coupons of 83 mm length, 15 mm width and 3 mm thickness. 1 mm thick epoxy tabs were attached to the ends of the composite coupons to facilitate adequate gripping of the specimens in the testing frame and to avoid slippage and possible failure at the grips.
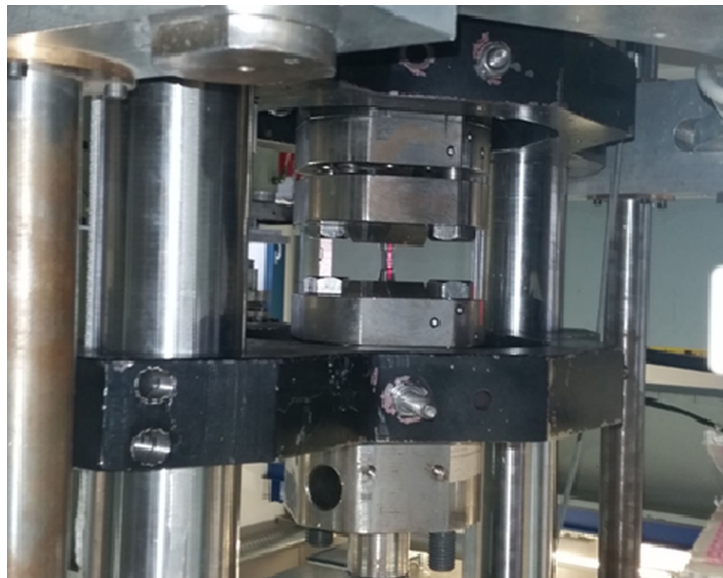
FIGURE 40: Tensile Testing Set Up

The on-axis tensile tests were performed at the Institute for Composite Materials, Kaiserslautern in order to examine the tensile behaviour of YS90A woven composite filled without and with DP (at volume fractions of 6% and 12% in the composite). The tensile tests were performed using a SHIMADZU® Universal testing machine (Figure 40). The machine had a load cell with a capacity of 40 kN and the tests were performed at 2 mm/min following ASTM D3039 standards.

In every test, load, displacement and strain were measured and recorded. The displacement was measured by the frame LVDT while the strain was measured by laser extensometer (developed and produced by Fiedler Optoeletronik GmbH)which enabled a contact free measurement of locally resolved strain distribution over the samples.

4.2.3.2 Finite Element Modelling

Numerical modelling was carried out for both the standard modulus T300 and the high modulus YS90A composite under tensile and flexural loading using ABAQUS®. Mesomechanical damage models were developed for damage detection, evolution and propagation through a progressive failure analysis methodology.

Material strength, interlaminar strength and fracture toughness properties of T300 woven composite were taken from [76],[77] and the interlaminar strengths for the YS90A composite were examined by numerical analyses as the experimental testings to measure the strength and the fracture properties of these composites were not performed.

Continuum damage mechanics models were implemented in ABAQUS® to represent the intralaminar damage modes (transverse matrix cracking and fibre failure) and cohesive elements were used to capture delamination at ply interfaces. The intralaminar and interlaminar damage models implemented are briefly described below.

4.2.3.2.1 Intralaminar Damage

The intralaminar damage is simulated in ABAQUS® using Hashin damage [78, 79] material model. The constitutive stress-strain relationship are formulated in a local Cartesian coordinate system considering the base vectors aligned with the fibre directions. The fabric reinforced ply was modelled as a homogeneous orthotropic elastic material with the potential to sustain progressive stiffness degradation due to fibre/matrix cracking and plastic deformation under shear loading [79].

It has been assumed that the elastic stress-strain relationship are given by orthotropic damage elasticity. Four failure modes that are evaluated are fibre tension, fibre compression, matrix tension, and matrix compression.

Damage Initiation

Initiation of damage refers to the onset of damage at a material point. Four different failure modes based on Hashin Criteria [78, 79] are described in Equations 4.22 to 4.25. The damage initiation criteria must be used in ABAQUS® with elements with a plane stress formulation, which include plane stress, shell, continuum shell, and membrane elements.

$$\text{Fibre Tension } (d_f^t \quad \text{if} \quad \hat{\sigma}_{11} \geq 0):$$

$$F_f^t = \left[\frac{\hat{\sigma}_{11}}{X^T}\right]^2 + \alpha\left[\frac{\hat{\tau}_{12}}{S^L}\right]^2 \tag{4.22}$$

$$\text{Fibre Compression} \quad (d_f^c \quad \text{if} \quad \hat{\sigma}_{11} \leq 0):$$

$$F_f^c = \left[\frac{\hat{\sigma}_{11}}{X^C}\right]^2 \tag{4.23}$$

$$\text{Matrix Tension } (d_m^t \quad \text{if} \quad \hat{\sigma}_{22} \geq 0):$$

$$F_m^t = \left[\frac{\hat{\sigma}_{22}}{Y^T}\right]^2 + \left[\frac{\hat{\tau}_{12}}{S^L}\right]^2 \tag{4.24}$$

$$\text{Matrix Compression } (d_m^c \quad \text{if} \quad \hat{\sigma}_{22} \leq 0):$$

$$F_m^c = \left[\frac{\hat{\sigma}_{22}}{2S^T}\right]^2 + \left[[\frac{Y_C}{2S^T}]^2 - 1][\frac{\hat{\sigma}_{22}}{Y^C}\right] + \left[\frac{\hat{\tau}_{12}}{S^L}\right]^2 \tag{4.25}$$

In the above equations, X^T and X^C are the longitudinal tensile and compressive strengths, Y^T and Y^C are the tensile and compressive strengths in the matrix direction, and S^L and S^T denote the longitudinal and transverse shear strengths. The coefficient α in equation 4.22 determines the contribution of the shear stress to the initiation of fibre tensile failure. $\hat{\sigma}_{11}$, $\hat{\sigma}_{22}$ and $\hat{\tau}_{12}$ and components of the effective stress tensor. The effective stress $\hat{\sigma}$ is used to evaluate the initiation criteria and it is intended to represent the stress acting over the damaged area that effectively resists the internal forces. $\hat{\sigma}$ is computed from:

$$\hat{\sigma} = \mathbf{M}\sigma \tag{4.26}$$

where σ is the true stress and $\mathbf{M}$ is the damage operator. The damage operator is defined as :

$$\mathbf{M} = \begin{bmatrix} \dfrac{1}{(1-d_f)} & 0 & 0 \\[2ex] 0 & \dfrac{1}{(1-d_m)} & 0 \\[2ex] 0 & 0 & \dfrac{1}{(1-d_s)} \end{bmatrix} \tag{4.27}$$

d_f, d_m and d_s are internal damage variables that characterise fibre, matrix, and shear damage, which are derived from damage variables d_f^t, d_f^c, d_m^t and d_m^c. The shear damage internal variable d_s is calculated as shown below

$$d_s = 1 - (1 - d_f^t)(1 - d_f^c)(1 - d_m^t)(1 - d_m^c) \qquad (4.28)$$

Prior to any damage initiation, the damage operator **M** is equal to the identity matrix so that $\hat{\sigma} = \sigma$. Once the damage initiation has occurred for at least one mode, the damage operator becomes significant in the criteria for damage initiation of other modes. An output variable is associated with each initiation criterion (fibre tension, fibre compression, matrix tension, matrix compression) to indicate whether the criterion has been met. A value of 1.0 or higher indicates that the initiation criterion has been met [79].

Damage Evolution

Once the damage initiation function has been satisfied, the associated damage variable would be different from zero and further loading would cause degradation of the material stiffness coefficients. The stiffness matrix of a damaged ply ($\mathbf{C_d}$) is defined as :

$$\sigma = \mathbf{C_d}\epsilon \qquad (4.29)$$

$$\mathbf{C_d} = \frac{1}{D} \begin{bmatrix} (1-d_f)E_{11} & (1-d_f)(1-d_m)\nu_{21}E_{22} & 0 \\ (1-d_f)(1-d_m)\nu_{12}E_{22} & (1-d_m)E_{22} & 0 \\ 0 & 0 & (1-d_s)G_{12}D \end{bmatrix}$$

$$(4.30)$$

where $D = 1 - (1 - d_f)\nu_{12}\nu_{21}d_f$ and d_f is the damage variable associated with fibre fracture, d_m is the damage variables associated with matrix failure. The damage evolution laws for the damage variables are defined in terms of the fracture energy dissipated during the damage process. The damage evolution laws are needed to predict the material response as loading increases beyond the point of initial damage. The damage progressions are characterised by degradation of the stiffness matrix.

At the point of initiation, the damage evolution model would begin to calculate the reduction in stress as the displacement of the element increases. The stress will drop until it reaches zero, the amount of displacement required to get to this point would be defined by the fracture energy, G_C (Figure 41). In case the strength properties remain constant when the fracture energy has been increased, the element will experience a larger displacement before it reaches ultimate failure [79]. During material softening, the damage variable will evolve such that the constitutive law is expressed as a stress-displacement relation (Figure 41) for the four failure modes. The positive slope of the stress-displacement curve (as shown in Figure 41) prior to damage initiation corresponds to linear elastic material behaviour. The negative slope after damage initiation is achieved by evolution of the respective damage variables [79].
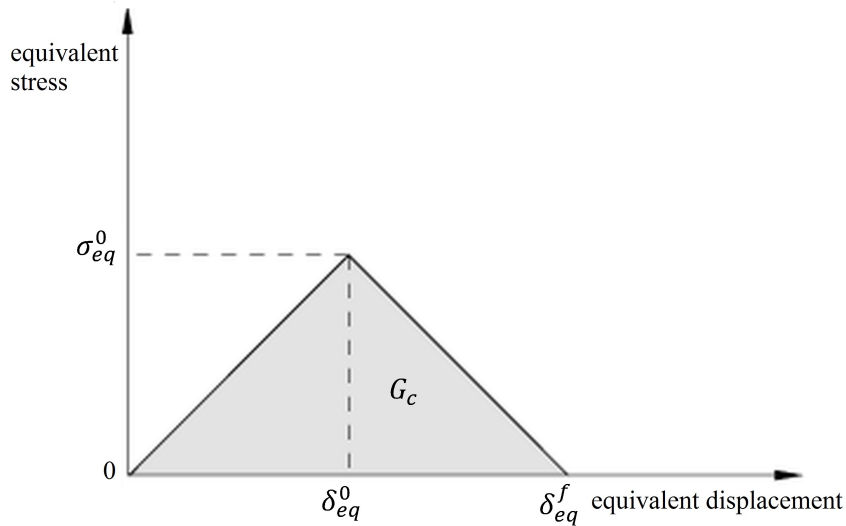
FIGURE 41: Equivalent stress versus equivalent displacement [79]

After damage initiation ($\delta_{eq} \geq \delta_{eq}^0$) for the behaviour shown in Figure 41, the damage variable (d) for a particular mode is given by the following expression

$$d = \frac{\delta_{eq}^f (\delta_{eq} - \delta_{eq}^0)}{\delta_{eq}(\delta_{eq}^f - \delta_{eq}^0)} \tag{4.31}$$

where δ_{eq}^0 is the initial equivalent displacement at which the initiation criterion for that mode was met and is the displacement at which the material is completely damaged in this failure mode. This relation is presented in Figure 42. The values of δ_{eq}^0 for the various modes depend on the elastic stiffness and the strength parameters specified as part of the damage initiation definition. For each failure mode the energy dissipated due to failure (G_C) must be specified. The values of δ_{eq}^f for the various modes depend on the respective G_C values [79].

FIGURE 42: Damage variable as a function of equivalent displacement [79]

4.2.3.2.2   Interlaminar Damage

Delamination (Interlaminar damage) is one of the typical failure mode in composite laminates due to weak bonding between fibre and polymer matrix. The constitutive response of the cohesive elements are defined by bilinear traction-separation law (Figure 43).

Damage Initiation

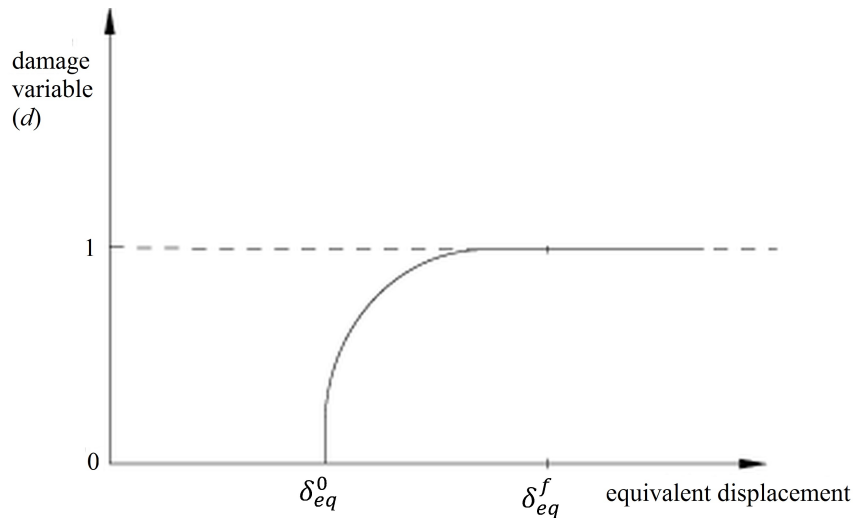The constitutive response shown in Figure 43 shows the linear elasticity before the damage initiation. The linear elasticity relates the nominal stress acting on the interface to the nominal strain. The cohesive elements are normally specified with unit thickness, so that the nominal strain corresponds to the separation value. The elastic modulus for the traction-separation law should be interpreted as penalty stiffness K_n. The penalty stiffness for the opening mode[§§] (Mode I) is defined as :

$$K_n = \frac{N_{max}}{\delta_n^{init}}$$

(4.32)

where N_{max} in Equation 4.32 is the maximum nominal stress and δ_n^{init} is the displacement at damage initiation in normal (opening) mode. The elastic response is governed by K_n and the thickness of the cohesive element is quite important to obtain the correct stiffness K_n. In ABAQUS® an unit thickness could be specified for the cohesive element or even geometric thickness based on the nodal coordinates could even be specified. The elastic modulus is interpreted as :

$$E_n = K_n h_{eff}$$

(4.33)

where h_{eff} is the thickness of the cohesive element. ABAQUS® evaluates the stiffness based on Equation 4.34 which is equivalent to Equation 4.35.

[§§]In fracture mechanics, the stress intensity due to any loading scenario can be broken down into three modes of loading: tensile opening - mode I, in-plane shear - mode II, and out of plane shear - mode III

| Mode I | Mode II | Mode III |
| tensile opening | in plane shear | out of plane shear |
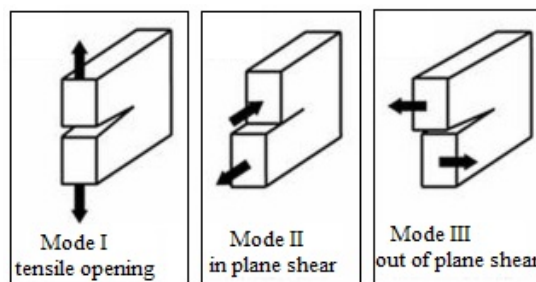
$$N_{max} = E_n \epsilon_n \tag{4.34}$$

$$N_{max} = K_n \delta_n^{init} \tag{4.35}$$

The nominal strain (ϵ_n) is defined as the ratio of the relative displacement (δ_n) between the top and bottom of the cohesive element to that of the thickness of the cohesive element.

$$\epsilon_n^{init} = \delta_n^{init}/h_{eff} \tag{4.36}$$
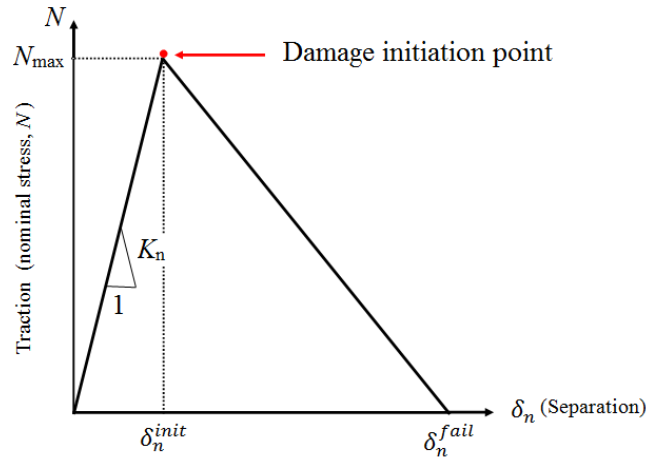
FIGURE 43: Constitutive response for delamination damage initiation [79]

When unit thickness is specified for the cohesive element, then the nominal strain is equal to the separation value. In this research the cohesive element is specified with an unit thickness. The onset of damage is attained when the total stress acting on the interface reaches a critical value N_{max} (Figure 43) and is given by:

$$\left\{ \frac{\langle \sigma_n \rangle}{N_{max}} \right\}^2 + \left\{ \frac{\sigma_s}{S_{max}} \right\}^2 + \left\{ \frac{\sigma_t}{T_{max}} \right\}^2 = 1 \tag{4.37}$$

$\langle \rangle$ in the equation 4.37 stands for Macaulay brackets which indicates that compressive normal stress does not contribute to damage initiation and σ_n, σ_s, σ_t are the nominal stress in the pure normal mode, first shear, second shear direction. For mode I opening mode, the damage initiates when :

$$\sigma_n = N_{max} \tag{4.38}$$

Damage Evolution

The constitutive response for the post damage initiation response is defined by :

$$\overline{\sigma} = (1 - d)K_n \tag{4.39}$$

where d is the scalar damage variable. d is equal to 0 when the response is undamaged and d is equal to 1 when the response is fully damaged. d increases monotonically. Damage propagation leads to a progressive reduction in the stresses transferred through the interface as well as in the interface stiffness. In ABAQUS®, damage evolution could be specified based on displacement or total fracture energy (fracture toughness). In this research energy based damage evolution approach is followed. The actual reduction of the stress transferred by the cohesive crack would be defined by the slope of the softening region which depends on N_{max} and the fracture toughness G_{TC} (Figure 44). The interply toughness depends on the mode-mix behaviour is determined by Benzeggaagh-Kenane [79] criterion as:

$$G_{TC} = G_{IC} + (G_{IIC} + G_{IC})\left[\frac{G_{Shear}}{G_T}\right]^{\eta} \tag{4.40}$$

where η is the Benzeggaagh-Kenane material parameter, G_{IC} and G_{IIC} are the critical fracture toughness values for pure Mode I and Mode II fracture $G_{Shear} = G_{II} + G_{III}$, $G_T = G_I + G_{II} + G_{III}$. Generally, the values of the Mode I and Mode II fracture toughness are predicted from the double cantilever beam (DCB) and the end notch bending (ENF) experimental testing.
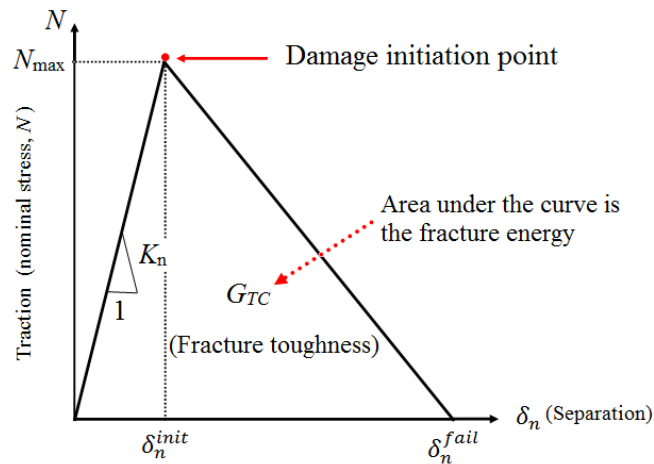
FIGURE 44: Constitutive response for delamination damage evolution based on energy [79]

4.2.3.2.3 Conventional shell versus continuum shell

Shell elements are used to model the structures where the thickness is significantly smaller. Conventional shell elements (Figure 45) use this condition to discretise a body by defining the geometry at a reference surface. In this case the thickness is defined through the section property definition. Conventional shell elements have displacement and rotational degrees of freedom [79].
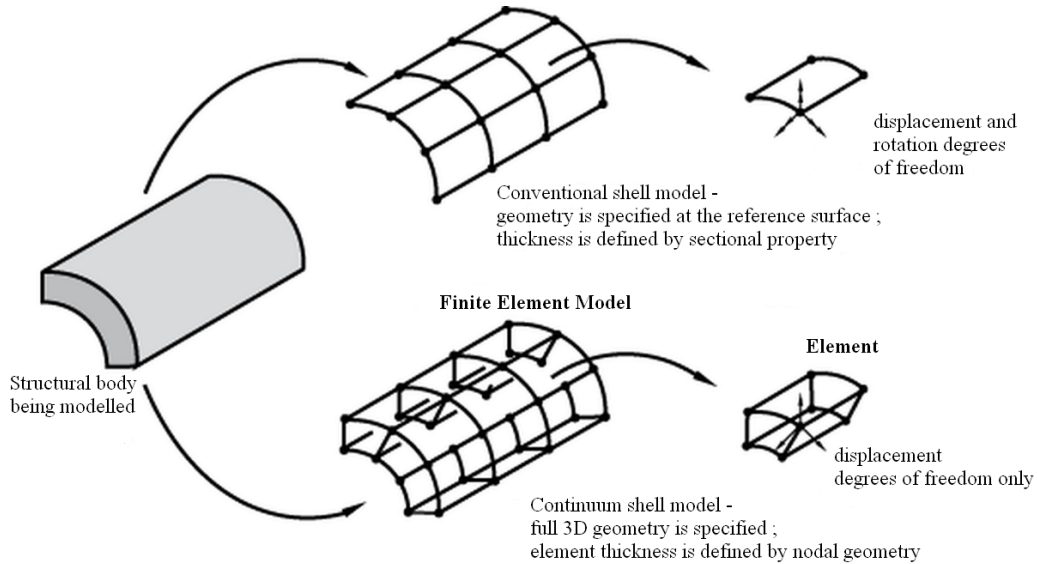
FIGURE 45: Conventional versus continuum shell element in ABAQUS® [79]

In contrast, continuum shell elements (Figure 45) discretise an entire three-dimensional body. The thickness is determined from the element nodal geometry. Continuum shell elements have only displacement degrees of freedom. From a modelling point of view continuum shell elements look like three-dimensional continuum solids, but their kinematic and constitutive behaviour is similar to conventional shell elements [79]. In this investigation, continuum shell elements are used for modelling composites in ABAQUS®.

4.2.3.2.4 Model Set-Up

Progressive failure analysis for the tension was performed with the on-axis laminates (0^0-90^0) of 117 mm in length, 15 mm in width and 3 mm in thickness respectively (Figure 46). The three point bending FEM was performed out with the on-axis laminates (0^0-90^0) of 83 mm in length, 15 mm in width and 3 mm in thickness respectively (Figure 46). A 5-ply laminate with a ply thickness of 0.6 mm along with a cohesive layer of nearly zero thickness between each ply was modelled (Figure 46) for both the tensile and bending loading. The bending stress-strains were then obtained using Equations 4.41 and 4.42.

$$\sigma_f = \frac{3FL}{2bh^2} \tag{4.41}$$

$$\epsilon = \frac{6sh}{L^2} \tag{4.42}$$

where F is the applied load, L is the span length and b is the width of the specimen which is about $15\,\text{mm}$. h is the thickness of the specimen and s is the deflection of the mid-span. The modulus was obtained using Equation 4.43

$$E_f = \frac{L^3}{4bh^3}\left[\frac{\Delta F}{\Delta s}\right] \tag{4.43}$$
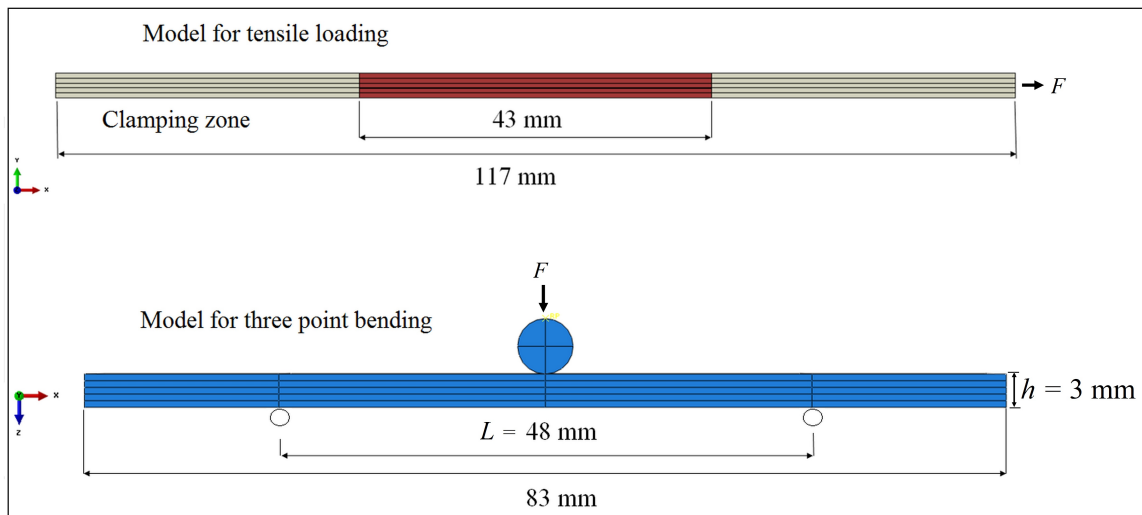
FIGURE 46: Finite element model representing the laminate and cohesive zone modelling for the on-axis tensile and three point bending scenarios

Each ply was modelled in Abaqus® using quadrilateral continuum shell elements, type SC8R which is an 8-node, quadrilateral and uses first-order interpolation with reduced integration and 3 degrees of freedom per node (Figure 47). Each ply was discretised by a single layer of continuum elements with reduced integration (reduced integration uses a lower-order integration to form the element stiffness and it reduces the computational time) through the thickness. As the ply failure criteria and continuum damage models were derived based on the stress state of a whole ply, a single integration point through the thickness of each ply is required. The cohesive layers between plies (Figure 47) were modelled using COH3D8 (COH stands for cohesive element, 3D stands for three dimensional and 8 stands for 8 node) cohesive elements.
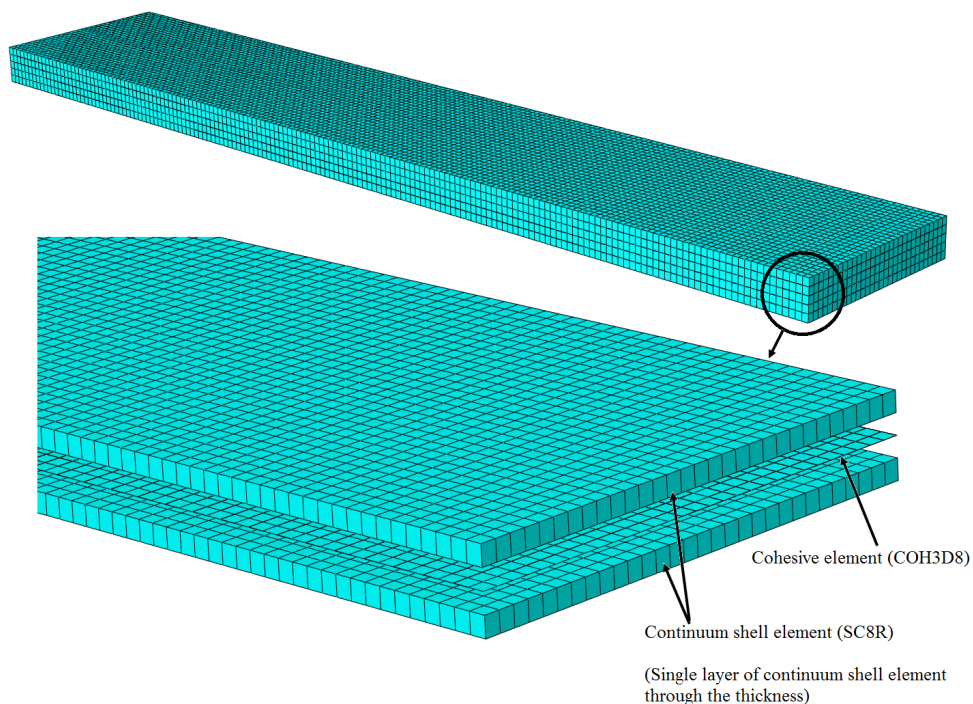
FIGURE 47: Finite element mesh with continuum shell and cohesive elements

The ply elements were connected with the cohesive elements by using the Tie constraints. The initial thickness of the cohesive elements were specified as unit thickness and a value of 1×10^6 N mm^{-3} was specified as the penalty stiffness for the interface. The interface elements were meshed with an element size of 0.5 mm. It is known that the response of cohesive elements are affected by the mesh size, however a detailed investigation of different element size towards the damage behaviour was not carried out here (due to computational difficulties). To alleviate the convergence difficulties, the viscous regularization option was assigned to the cohesive elements. The material data giving the elastic properties of the standard (T300) and the high modulus (YS90A) woven composite filled with diamond powder are detailed in Table 16.

Material strength, interlaminar strength and fracture toughness properties of T300 woven composite given in Table 17 were taken from the literature, as the experimental testings to measure the strength and the fracture properties were not performed. Interlaminar strengths for YS90A composite (Table 17) were examined by numerical analyses. Normal and shear strengths were examined from FEM model of an undamaged coupon under the same boundary conditions. In the numerical analysis the interlaminar shear stress was assumed as the interlaminar shear strength and normal stress at the ultimate load was taken as the normal strength of the laminate.

Fibre	Properties							
	X_T (MPa)	Y_T (MPa)	Y_C (MPa)	S_{12} (MPa)	σ_{I0} (MPa)	σ_{II0} (MPa)	G_{IC} (J m^{-2})	G_{IIC} (J m^{-2})
T300	539.5	550	507	128	12	26	800	1750
YS90A	361	361	361	60	30	30		

TABLE 17: T300 woven material strength [76], interlaminar strength and toughness [77]; YS90A material strength, interlaminar strength

For the on-axial tensile models, fully clamped boundary conditions were applied at one end of the specimen and a uniform axial displacement was prescribed at the opposite end. For on-axial flexural models, simply supported boundary conditions were applied at the ply nodes of supports. Tie constraints were applied to provide contact between the surface of rigid indenter and the surface of the top ply. A displacement controlled load was applied at the reference point on the rigid indenter which comes in contact with the top ply of the laminate.

Three different configurations of T300 and YS90A filled composite under static tension and bending (displacement control) corresponding to coupons without DP and coupons with 6% and 12% DP by volume fraction in the composite were simulated by means of an implicit numerical scheme. On average, each on-axis flexural simulation took about six hours and each on-axis tensile simulation took about five hours to run on a single 3.4 GHz Intel® Core™ i7 processor.

4.2.4   Results and Discussion

4.2.4.1   Three-Point-Bending Simulation

4.2.4.1.1   T300 Composite

A FEM analysis was carried out for the T300 woven composite considering specimens with and without diamond powder. Upon examination of the results which are shown in the stress-strain curves (Figure 48), the bending stiffness to peak load occurs without any visible delamination and without any oscillations before the peak load. This linear region of the curve explains the elastic deformation of the composite. After the load reaches its peak value, a significant drop in the peak load was observed. This sudden drop can be attributed to fibre cracking (Figure 48).
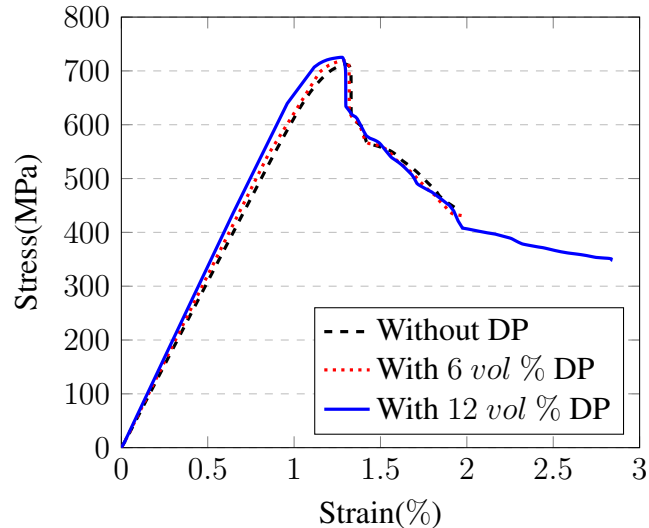

FIGURE 48: FEM results for the on-axis flexural behaviour of the T300-diamond powder filled composite and unfilled reference model

The top region of the laminate experiences compression (Figure 49 (b)). The bottom region experiences tension (Figure 49 (a)) and the middle region experiences shear as can be seen in (Figure 49 (c)). Delamination was initiated faster in the middle cohesive layers. The top and the bottom layers exhibited a mode-I type fracture, triggered by normal stresses. The middle layers exhibited a mode-II type fracture (Figure 49 (d)). Delamination damage developed more rapidly in the middle cohesive section than in the top and bottom layers. The reason for mode-II damage in the middle cohesive layers (Figure 49 (d)) can be attributed to a maximum through the thickness shear stresses occurring in the middle region of the laminate. A similar fracture behaviour has been reported by H. Ullah $et.al$ in [77]. After the crack initiated in tensile side, the crack propagates to the compressive side within the laminate before final failure which occurred through brittle fracture (Figure 49). When a load is applied to the composite structures in this study, the matrix starts to crack first and stress is then transferred from the lower modulus matrix to the filler and then to the reinforcing fibres via a bridging effect and ultimately the composites properties enhance. From Table 18, it is clear that the flexural modulus, flexural strength and failure strain all increased with the inclusion of DP, although the influence of the DP on the flexural strength and modulus is quite minimal. The failure strain increased significantly with

12 $vol\ \%$ volume fraction of diamond powder in the composite. The diamond powder filled epoxy matrix also slowed the crack propagation under flexural loading, which resulted in an increase in the failure strain.
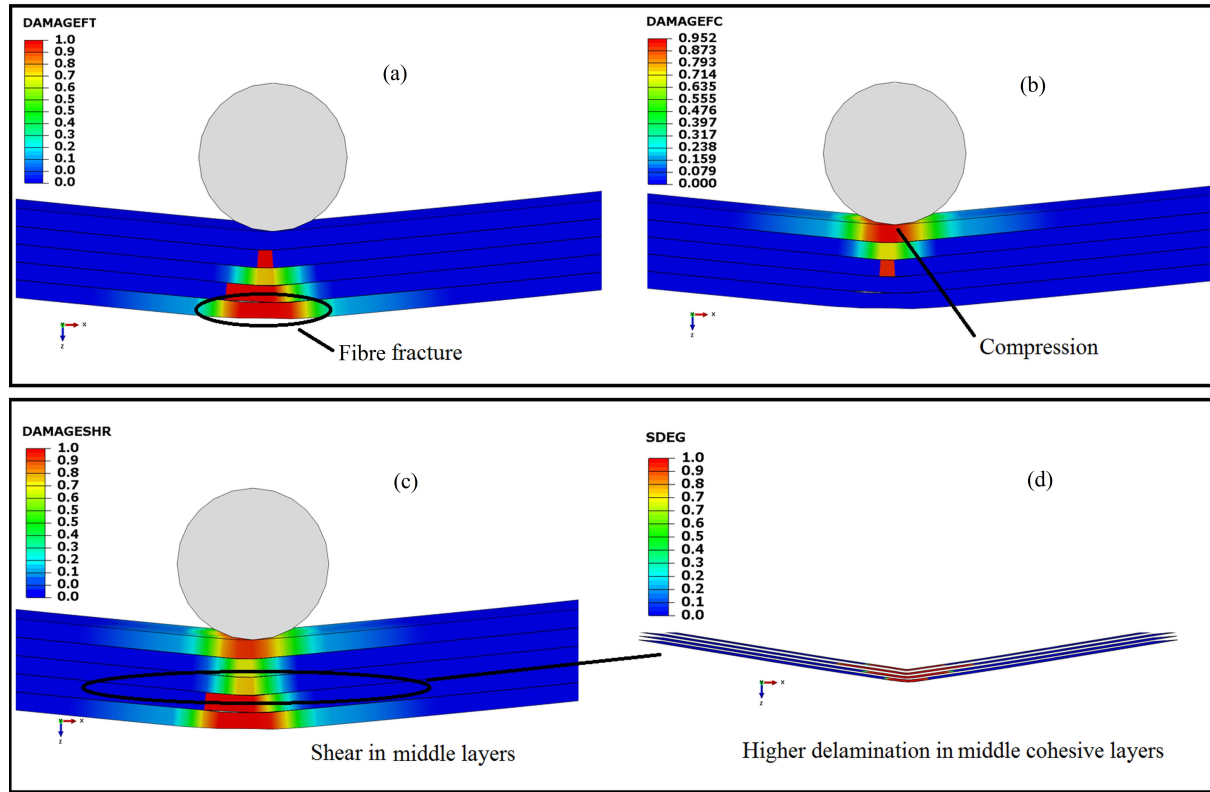
FIGURE 49: Contour plots (a-d) showing the fibre fracture (DAMEGEFT) in the bottom region, the top region experiencing compression (DAMEGEFC), the middle region expereincing shear (DAMEGESHR) and the delamination damage in cohesive layers between the plies of the T300 composite under bending. (SDEG is the scalar stiffness degradation variable)

Results	Without DP	With 6 $vol\ \%$ DP	With 12 $vol\ \%$ DP
E_f(GPa)	62	65.9	67.9
σ_{fm}(MPa)	712.4	719	725.2
ϵ_{fm} (%)	1.3	1.31	1.27
σ_{fb} (MPa)	442.6	428	348
ϵ_{fb}(%)	1.94	1.98	2.84

TABLE 18: FEM results of T300 composite coupons representing flexural modulus(E_f), flexural strength(σ_{fm}), deflection at flexural strength(ϵ_{fm}), strength at break(σ_{fb}), deflection at break(ϵ_{fb})

4.2.4.1.2 YS90A Composite

Finite element modelling was carried out to also investigate the on-axis flexural behaviour of the YS90A woven composite. The first region in the stress-strain curve (Figure 50) with linear behaviour explains the elastic deformation.

It was observed from the FEM analysis that the fibres on the top surface of the model, which are in compression, remain intact (Figure 51 (b)).

It can be seen that the failure occurred due to fibre fracture on the bottom surface which is in tension (Figure 51 (a)).
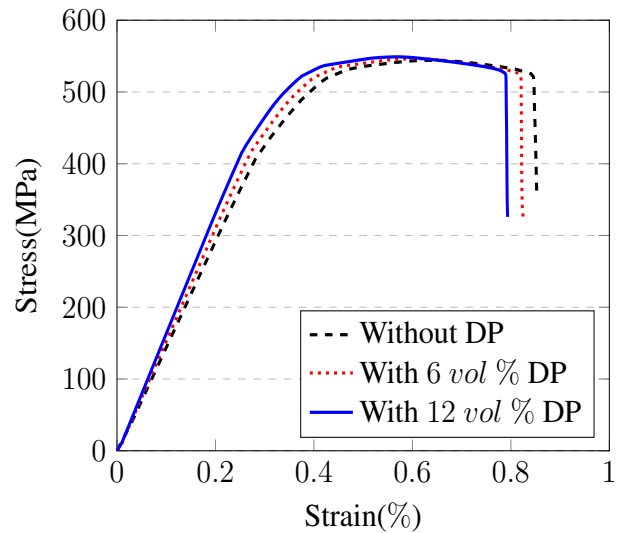
FIGURE 50: Stress-Strain curve for the on-axis bending behaviour of YS90A-diamond powder filled composite
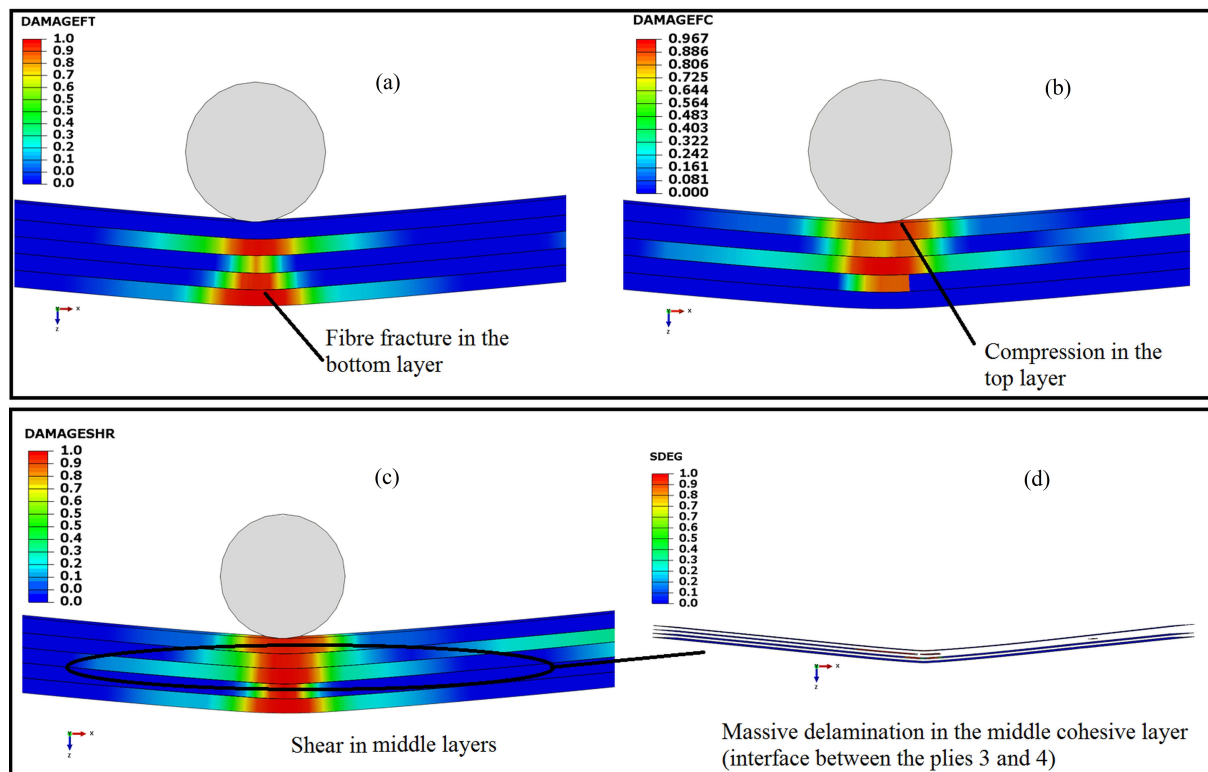
FIGURE 51: Contour plots (a-d) showing FEM damage modes of the YS90A composite under three point bending scenario

Massive delamination (Figure 51 (c-d)) started to initiate and propagate from the middle surfaces which can also be seen in the stress-strain curve (Figure 50) in the region after the load reached its peak value. At this point, a significant drop in the peak load was observed in the

laminate. The final failure observed in the simulation was due to fibre cracking in the bottom layers, which experience tension along with delamination in the middle layers. The diamond infused matrix again increased the flexural stiffness (Figure 50) but compared to T300 composite (Figure 48), the crack propagation in the high modulus YS90A composite was higher which reduced the ultimate failure strain (Table 19).

Results	Without DP	With 6 vol % DP	With 12 vol % DP
E_f (GPa)	147	155	165
σ_{fm} (MPa)	544.3	546.5	549
ϵ_{fm} (%)	0.65	0.61	0.57
σ_{fb} (MPa)	354	326.3	325.9
ϵ_{fb} (%)	0.85	0.82	0.79

TABLE 19: FEM results of the YS90A composite coupons representing flexural modulus(E_f), flexural strength(σ_{fm}), deflection at flexural strength(ϵ_{fm}), strength at break(σ_{fb}), deflection at break(ϵ_{fb})

4.2.4.2 On-axis Tensile Simulation

4.2.4.2.1 T300 Composite

The FEM results of the on-axis tensile stress-strain behaviour of the standard modulus T300 woven composite ((55% fibre volume fraction)) with and without DP are presented in Figure 52. The characteristics of an instantaneous load drop past the maximum tensile load would prove to be an actual case where the fibre failure occurs in all the plies almost simultaneously corresponding to the behaviour of brittle failure.
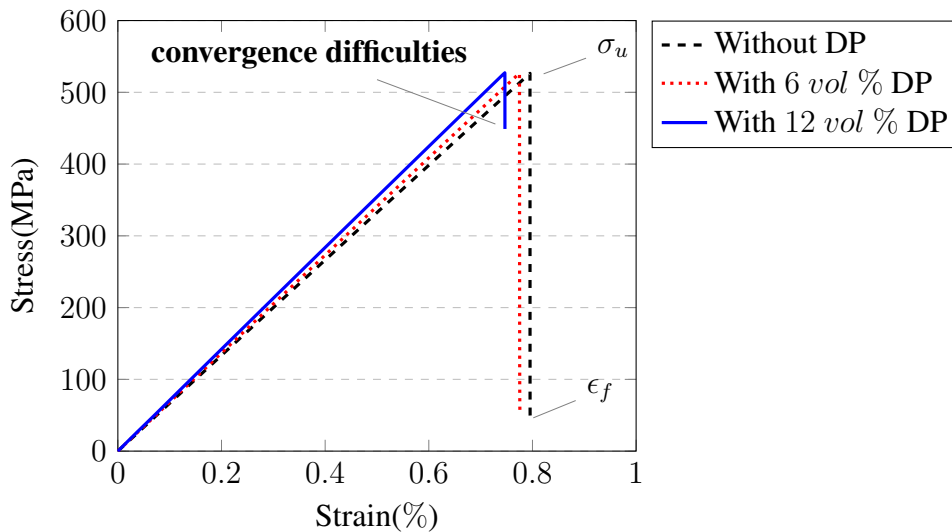

FIGURE 52: FEM results for the on-axis tensile behaviour of T300-diamond powder epoxy filled composite

fibre, matrix and the delamination damage modes are presented in Figures 53,54 which demonstrate the typical characteristics of brittle failure. It can be seen that the damage initiation was faster with 6 vol % and 12 vol % DP present in the composite. From Figure 53 it is clear that the fibre failure occurs in all the plies. Matrix damage (Figure 53) and delaminations (Figure 53, 54) were only confined to the crack path.

Overall, matrix damage in the composite has been reduced with the addition of diamond powder. With the inclusion of diamond powder, the elongation at break in the composite reduced drastically (Table 20, Figure 52) as the diamond powder enhanced epoxy matrix became stiffer and brittle.

The elastic modulus (E) of the composite as shown in Table 20 was predicted from the ultimate tensile strength (σ_u) and the failure strain(ϵ_f). With the infusion of diamond powder, elongation at break in the composite reduced drastically (Table 20, Figure 52) as the diamond powder enhanced epoxy matrix became stiffer and more brittle.

Convergence difficulties were observed in the composite filled with 12 vol % of diamond powder (Figure 52). The damage analysis were carried out in an implicit scheme and the presence of stiff rigid matrix, contact constraints along with the stiff cohesive elements led to convergence difficulties.
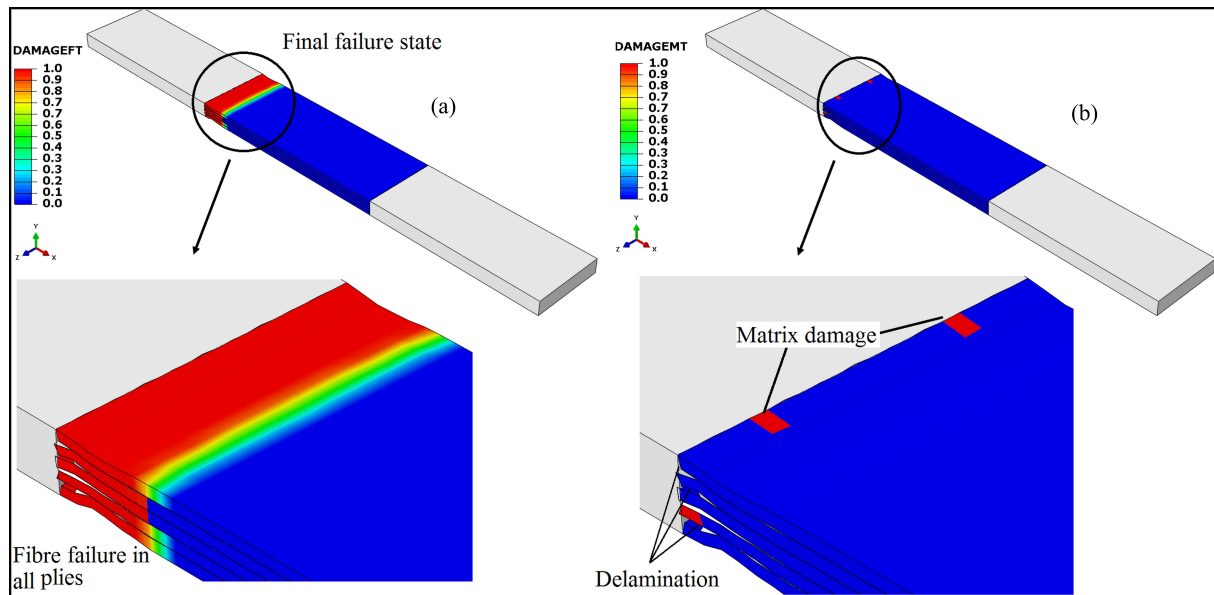
FIGURE 53: Contour plots (a-b) of the fibre failure (DAMEGEFT), the matrix damage (DAMEGEMT) in the standard modulus T300 composite under tension
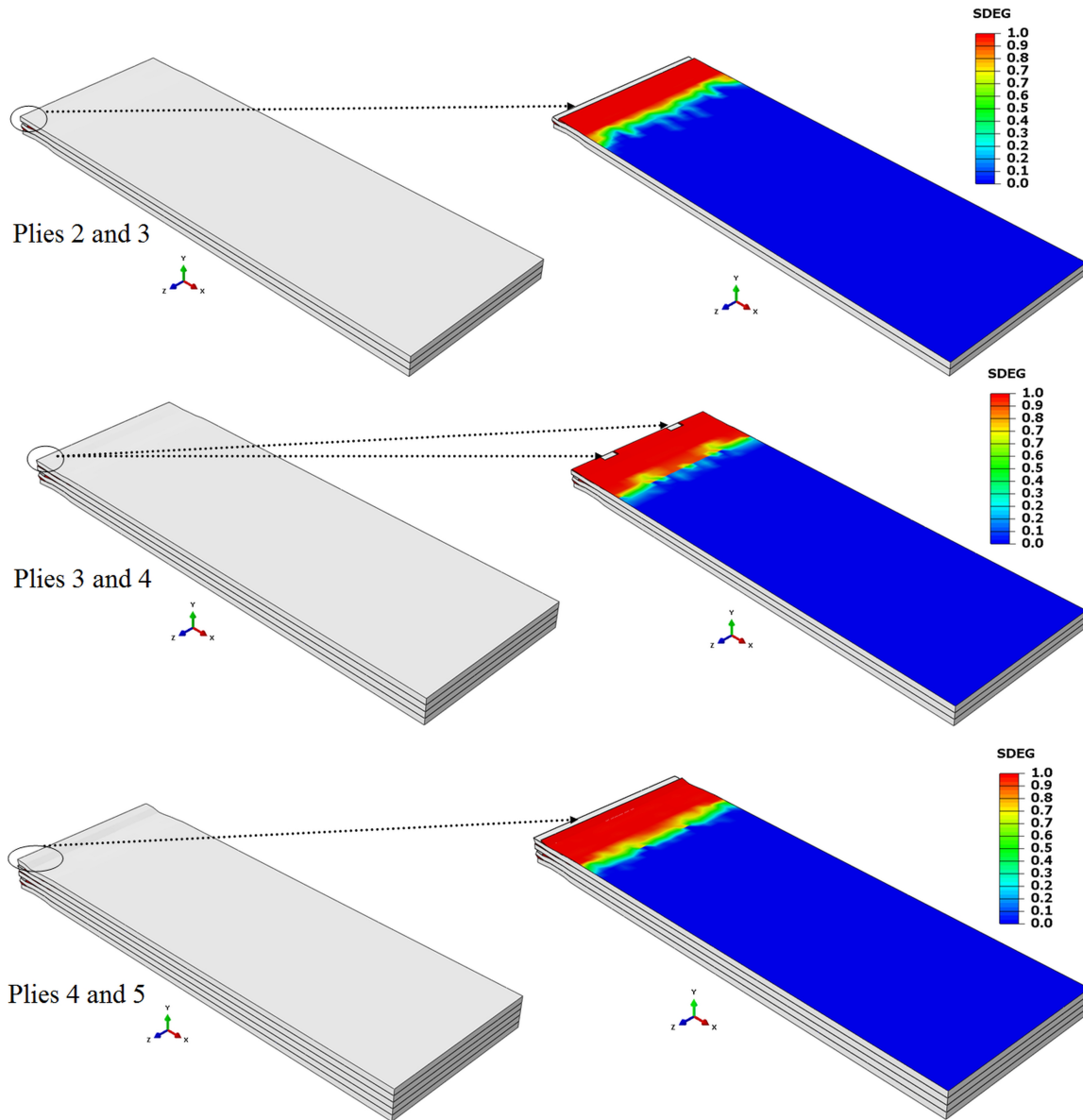
FIGURE 54: Contour plots showing delamination in the T300 composite under tension (elements were deleted upon reaching maximum degradation)

As a result of enhancing the epoxy with DP, the tensile modulus and tensile strength of the composite (Table 20) increases while the elongation at break reduces substantially, which means that high strength fillers like DP change the matrix behaviour into a more rigid-like material.

Results	Without DP	With $6\ vol\ \%$ DP	With $12\ vol\ \%$ DP
E(GPa)	66.7	68.5	71.1
σ_u(MPa)	526.2	526.3	527
ϵ_f(%)	0.79	0.77	0.75

TABLE 20: On-axis tensile FEM results of the T300 composite coupons representing the modulus of elasticity(E), ultimate strength(σ_u), failure strain(ϵ_f)

4.2.4.2.2   YS90A Composite

Experimental tensile results

The experimental tensile testing was performed at the Institute for Composite Materials, Kaiserslautern. The results showed a brittle fibre fracture along with delamination. From the tensile testing, a drastic reduction in the elastic modulus and strength of the YS90A composite filled with diamond powder was observed (Figure 56, Table 21). The average ultimate tensile strength of the composite reduced to $320\,\mathrm{MPa}$ with $6\,\%$ volume fraction of DP in the composite, while with $12\,\%$ volume fraction of DP in the composite, the ultimate tensile strength reduced to $286\,\mathrm{MPa}$ (Figure 56).

The failure strain of the composite increased to $0.56\,\%$ with $12\,\%$ volume fraction of DP in the composite. Elastic moduli reduced significantly to $157.7\,\mathrm{GPa}$ and $129.6\,\mathrm{GPa}$ with DP volume fractions of $6\,\%$ and $12\,\%$ in the composite. One of the reasons for the severe reduction in the strength and stiffness are due to the non-homogeneous dispersion (Figure 55) of DP in the matrix.
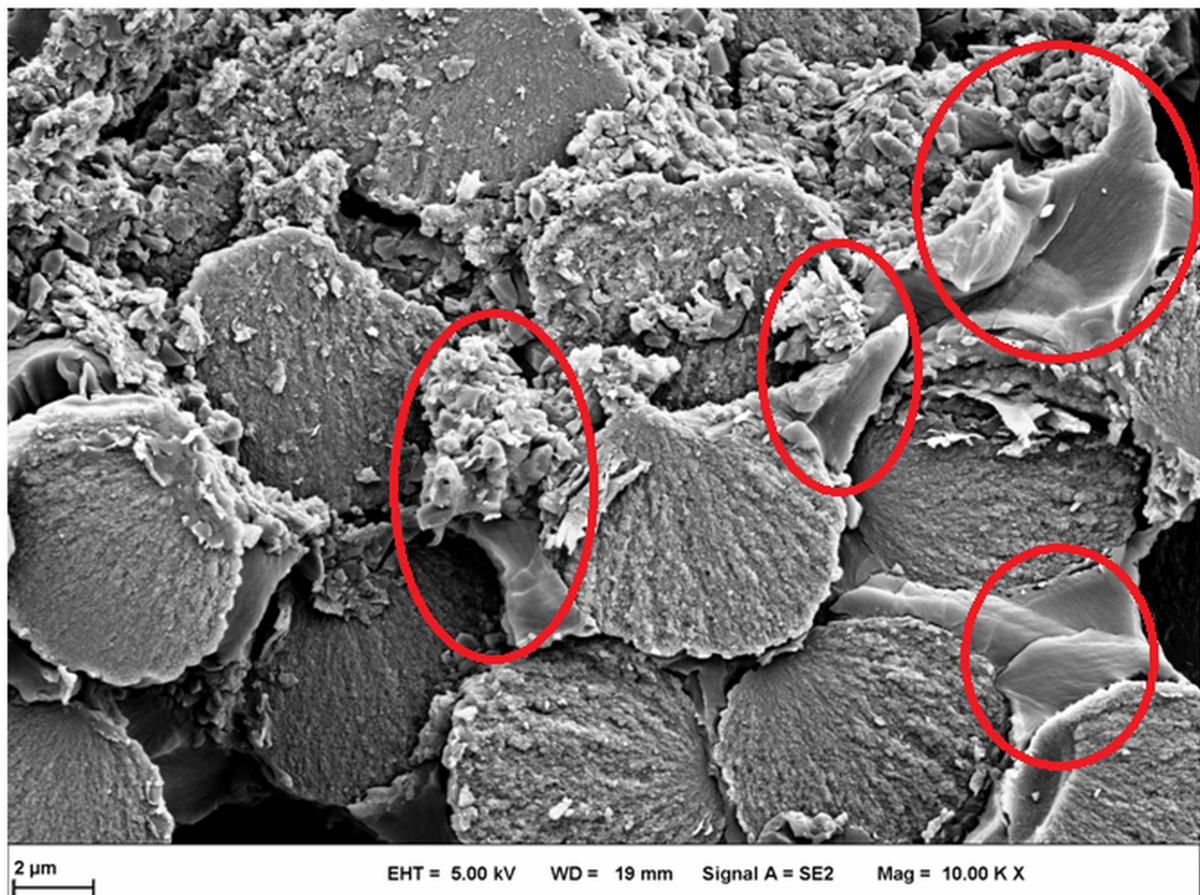

FIGURE 55:   SEM image showing non-homogeneities in dispersion of DP
(marked in red) in the composite

Ultrasonication techniques were not used to achieve uniform dispersion and the manufacturing procedure was carried out by hand-layup, which led to a reduction in the production quality of the testing coupons. A higher content of diamond powder led to agglomerations and also the sharp edges of the DP itself can contribute to stress concentrations through geometric defects.

A good dispersion and the interfacial properties between the epoxy resin and DP are crucial for determining the properties of the composite as the interface between the two is the region where the stresses are transferred from the epoxy resin to diamond powder and thereby into the composite material itself.

It is stated in the literature[80] that higher filler content leads to an agglomeration of particles, which reduces the adhesion between matrix and fillers and causes a drop in the mechanical strength of composites. Agubra et al. have stated that an increasing viscosity causes problems in the homogeneous dispersion of fillers and therefore results in the agglomeration of the filler particles [50]. Hossain et al. and Demirkol et al. have reported that, the non-homogeneous distribution of fillers at high filler content led to agglomeration and caused stress concentration regions, leading to some drop in the strength and modulus [81, 82]. Sobia et al. reported [83] that the mechanical properties of epoxy-diamond composites initially increased at lower contents of DP but with the higher content the mechanical properties decreased due to agglomeration.

High modulus YS90A being a pitch based carbon fibre was extremely fragile to handle in terms of fabrication of the samples and the interface bonding between diamond powder-epoxy resin was not perfectly formed which can be seen from the SEM image shown in Figure 55. From the SEM image, it can be noted that, as the content of DP increased in the matrix, the DP filler network could have trapped some portion of epoxy resin preventing it from infiltrating the reinforcing fibres properly. The above hypothesis could be one of the reasons for the reduction in the tensile properties (Figure 56, Table 21) of the DP filled composite.

To understand the above mentioned behaviour further, finite element modelling was performed with and without stress concentrations in the present composite specimen.

On-axis tensile simulation without stress concentrations

The FEM results of the on-axis tensile behaviour of the YS90A composite (without stress concentrations) exhibited a delamination type failure. Delamination triggered a substantial level of load drop due to dissipation of energy (Figure 56). At the ultimate tensile strength of the composite (Figure 56) just before the occurrence of massive delamination, it is worth noting that fibre failure was not detected in any of the plies (Figure 57 (a)) and that matrix damage was also not present. After this point, the propagation of delamination (Figure 57 (b), 58) at the interface developed further.
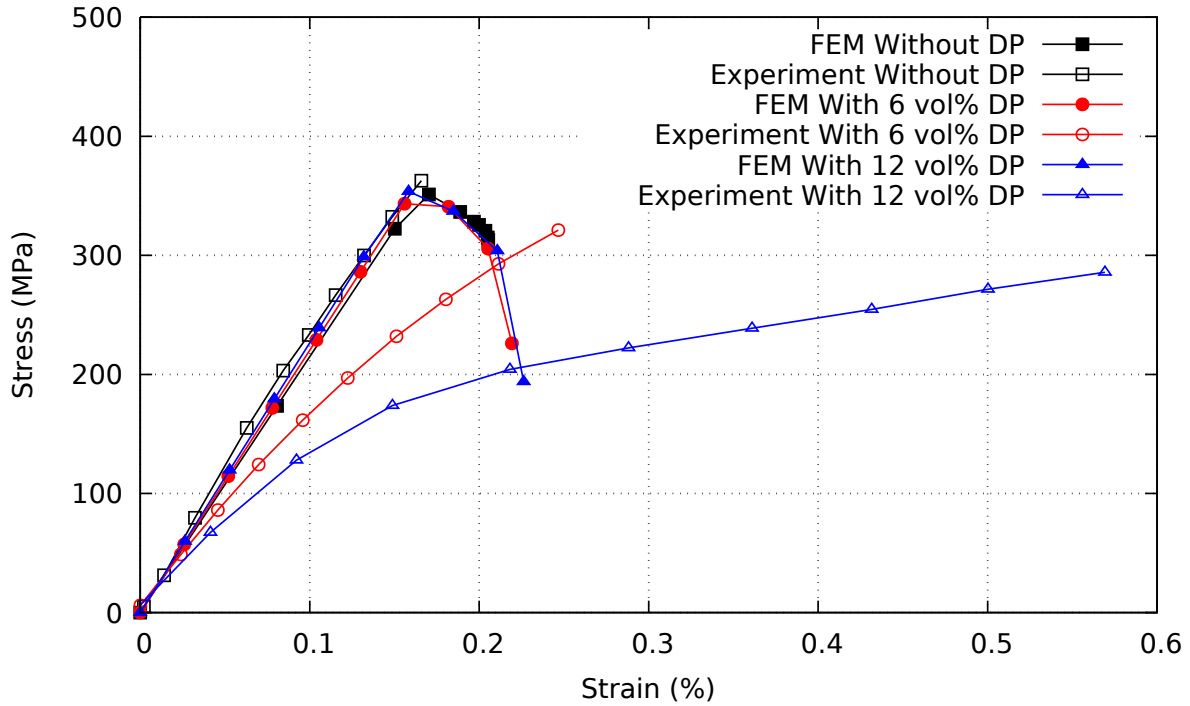
FIGURE 56: Comparison between the experimental tensile testing results and FEM tensile behaviour without considering stress concentrations in the laminate

Figure 57 (a-b) represents the damage mode occuring in the plies and shows that fibres in the on-axis plies have not failed even as the load drops significantly to a level corresponding to the failure stress.

The FEM analysis of laminates without DP showed a tensile strength and modulus of $215\,\text{GPa}$ and $355\,\text{MPa}$ respectively (Figure 56, Table 21) which are in close agreement with the experimental results (Figure 56). The analysis of laminates with 6 vol % and 12 vol % of DP shows an increasing trend in the elastic modulus whereas the experimental results shows a decreasing trend due to the presence of DP induced stress concentration in the samples.

Results	Without DP		With 6 vol % DP		With 12 vol % DP	
	Experiment	FEM	Experiment	FEM	Experiment	FEM
E(GPa)	226.3±2572	215	157.7±209	220	129.6±229	226
σ_u(MPa)	361±131	355	320±112	355	286±38	355.1
ϵ_f(%)	0.17	0.22	0.25	0.21	0.56	0.23

TABLE 21: Comparison between the experimental tensile and FEM tensile results (without stress concentrations in the laminate) of the YS90A composite representing the modulus of elasticity(E), ultimate strength(σ_u), failure strain(ϵ_f)

FIGURE 57: Contour plots (a-b) showing detection of the final fracture

FIGURE 58: Delamination in the interface of the YS90A composite under tension.

On-axis tensile simulation with stress concentrations

To study the behaviour of stress concentrations in the YS90A composite filled with diamond powder, Open Hole Tension (OHT) coupons were modelled with diameters of 6 mm (laminate filled with $6\ vol\ \%$ DP, Figure 59) and 10 mm (laminate filled with $12\ vol\ \%$ DP, Figure 59).
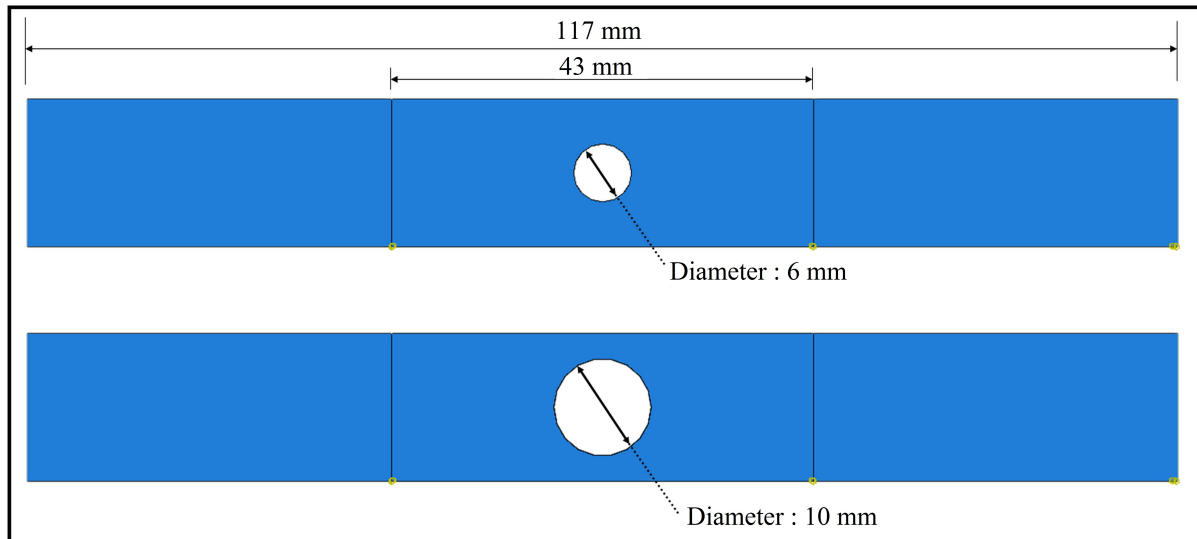

FIGURE 59: Development of the OHT laminate with a diameter of $6\,\text{mm}$ (a) and $10\,\text{mm}$ (b) for studying the behaviour of stress concentrations under tensile loading

The FEM results with the Open Hole Tensile (OHT) coupons exhibited a brittle fibre fracture (Figure 60 (a-b)) along with delamination. The results also revealed that the presence of stress concentrations would severely reduce the stiffness and strength of the DP filled composite. Comparison of the experimental results (Figure 56) with the FEM OHT results are listed in Table 22.

The FEM results with the OHT coupons predicted a reduction in the elastic modulus for the composite filled with DP (6% and 12% volume fraction) with the predictions showing reasonable accuracy when compared to the experimental results (Table 22). From the data given above, it is evident that the reduction in the elastic modulus is due to inhomogeneities in the dispersion of the DP and the presence of possible stress concentrations in the composite.

The FEM results also show that a higher content of DP causes weak adhesion in the fibre-matrix interface which reduces the the strength of the composite and also reduces the ability of the composite to resist the damage (Figure 60 (a-b), Table 22). The FEM results also show that the presence of a rigid filler reduces the elongation at the break (Table 22).

In general, the elastic and the failure properties reduce significantly with the presence of stress concentrations. The drastic increase in the failure strain (Table 22, Figure 56) as shown by the

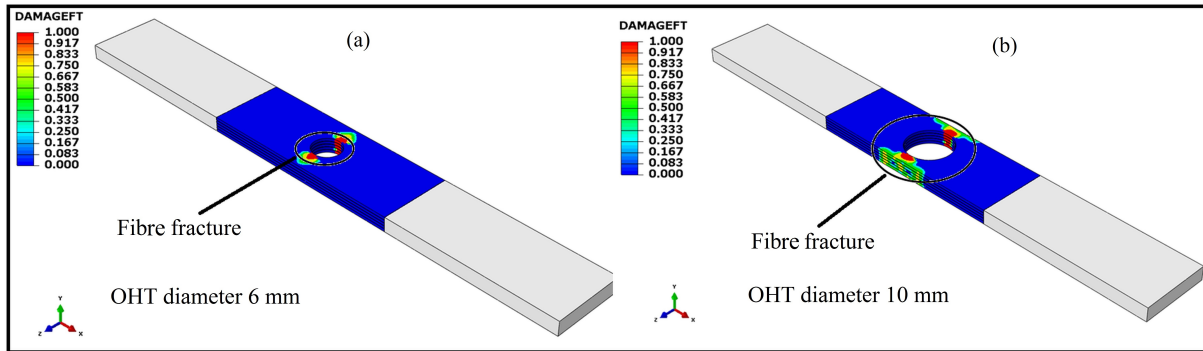experimental results for the composite filled with 12% volume fraction of DP requires further investigation.

FIGURE 60: Fibre failure under tension for the YS90A composite with stress concentrations modelled with OHT coupons with diameters of $6\,\text{mm}$ (a) and $10\,\text{mm}$ (b)

Coupons	E(GPa)		σ_u(MPa)		ϵ_f(%)	
	6 *vol* % DP	12 *vol* % DP	6 *vol* % DP	12 *vol* % DP	6 *vol* % DP	12 *vol* % DP
FEM - stress concentrations (Open Hole Tension (OHT))	173	93	209.12	119	0.12	0.11
Experimental testing (Figure 56)	157.7	129.6	320	286	0.25	0.56

TABLE 22: Comparison of the on-axis tensile experimental testing (with the normal specimen) and FEM - OHT (with stress concentrations) results of the YS90A composite representing the modulus of elasticity(E), ultimate strength(σ_u) and failure strain (ϵ_f)

4.2.5 Summary

In this study, the elastic and failure characteristics of standard modulus T300 and high modulus YS90A woven composites filled with diamond powder were examined. A numerical homogenisation technique was applied to predict the elastic properties of the diamond powder enhanced matrix. Micromechanical unit cell models were first developed to predict the elastic properties of the diamond powder filled woven composites.

Finite element modelling was then carried out to predict the failure behaviour of the composite under tension and flexure. The influence of DP on the moduli and flexural strengths of the T300 and YS90A composites was quite minimal. From the on-axis FEM simulations it was observed that with the addition of DP, elongation at break in the composite reduced drastically as the DP

epoxy matrix became stiffer and brittle.

Fabrication of the YS90A composite through the matrix modification technique with DP led to agglomeration. A inhomogeneous dispersion of the diamond powder in the composite was observed from SEM images. This eventually reduced the elastic properties of the YS90A composite when subjected to on-axis tensile testing.

Finite element modelling of the YS90A composite was carried out with OHT coupons to investigate the effect of stress concentrations in the composite when subjected to tensile loading. A reduction in the elastic modulus was observed with the OHT FEM results.

The predicted elastic properties of the DP filled composite has a direct influence in the development of the stave design. The enhanced material properties will be applied as a numerical input for the DP filled carbon fibre pipe. This is one of the focus in order to develop a stave design with a low thermal figure of merit.

5 Design and Development of Novel Local Support Structures

5.1   Introduction to New Designs

The design of a stave is deeply related to the detector layout. In general, the active elements (sensors) should be distributed in the detectors volume, then the mechanical structures can be developed around them. The requirement on the thermal performance assures that the modules will not suffer the so called "thermal run-away" at the end of the detectors life.

The metric for the requirements is given by the Thermal Figure of Merit (TFM) and it is typical of any local supports design (Refer to Table 1, Section 2.6). The contribution to the total TFM comes from several areas: from the HTC (Heat Transfer Coefficient) in the pipe, from the interfaces in the local supports cross section and from the heat conduction in the materials [84]. As already specified in Section 2.2, the convective TFM is not considered and the conductive TFM is the only focus of this thesis.

Figure 61 shows the conductive TFM requirement. As the performance of the stave depends upon the layer's radius, there is a TFM value for each layer. Moreover, the requirement depends also by the type of the sensor.
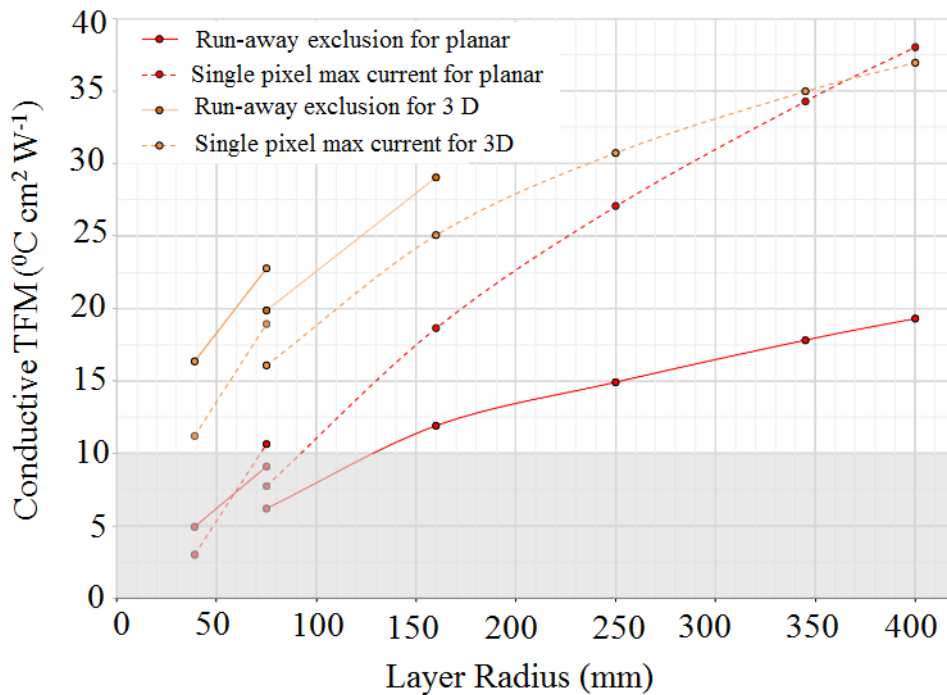
FIGURE 61: Requirement for an optimal conductive thermal figure of merit of the staves in different barrel layers mounted with planar or 3D sensors [84]

Two types of sensor namely the Planar and 3D have been proposed. The solid lines shown in Figure 61 give the conductive TFM limit required to cope with the thermal run-away and this is highlighted in orange color for the 3D and in red color for planar sensors. The dotted lines in Figure 61 show the limit for the maximum pixel current (set at $10\,\mathrm{nA}$) with the same color coding. It could be observed that the TFM requirement with the planar sensor is quite low, than

with a planar sensor. This is due to the fact that, the planar sensor dissipate more power than the 3D due to its higher depletion voltage. It is not yet decided which of these two types of sensor will be mounted on the stave.

However the objective of this study is to develop new stave designs that would fulfill the stiffness requirement (already discussed in section 2.6, Table 1) including a low TFM. With this goal, three new stave designs namely the "Fishbone stave", the "Iso-Graphite stave" and the Stiffener stave" were developed (Figure 62). Several design and parametric modifications were performed for these three designs. Shape optimisation technique using different design variables and constraints were performed for the Fishbone stave.

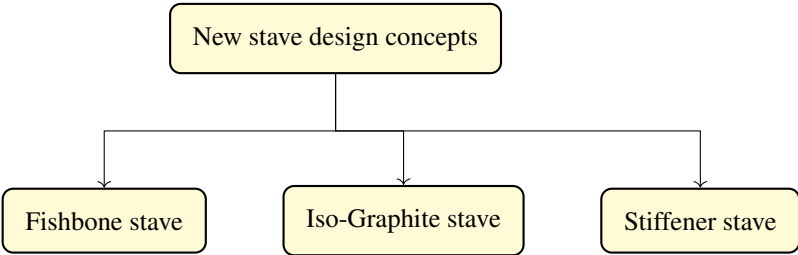FIGURE 62: Overview of the new stave designs

The procedure for evaluating the stave structural, thermal and thermomechanical behaviour (Figure 63) was carried out through the finite element method. The CAD models were developed in CATIA® V5 and were analysed in ABAQUS® 6.12-1.
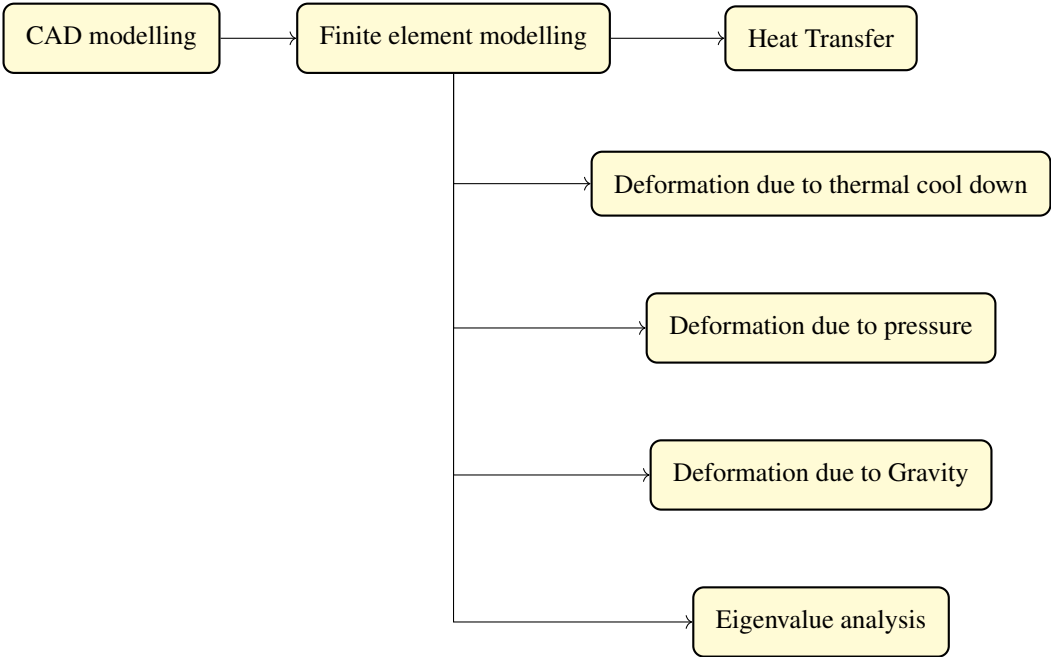
FIGURE 63: Procedure for reviewing of stave design performance

5.1.1   Composite Material Characterisation

An approach based on the classical lamination theory (CLT) was followed in order to calculte the elastic properties of the composite laminate. By this approach, the material properties of parts (of the stave design) which were developed with composite materials (with the fibre orientations of $[0/90/0]$ and $[0/60/-60]_s$) were obtained and these were used for performing the analysis.

The calculated elastic properties of composites as described in section 4.2.2 and in Table 16 were applied as an input in order to predict the elastic properties for the DP filled carbon fibre pipe with the fibre orientation of $\pm 45°$ and $[\pm 45/\overline{0}]_s$. The procedure for CLT (Figure 64) was programmed in Matlab® to generate the laminate elastic properties.

$E_1, E_2, \nu_{12}, G_{12}$	Engineering constants of ply
$[Q]_{1,2}$	Principal layer stiffnesses
θ_k	Fibre orientation of layer k
$[Q]^k_{x,y}$	Transformed layer k stiffnesses referred to x-y system
$Z_k - Z_{k-1}$	Location of layer k surfaces
$[A]_{x,y}, [B]_{x,y}, [D]_{x,y}$	Laminate stiffness matrices referred to x-y system
$[a]_{x,y}$	Laminate extensional compliance matrix
h	Total laminate thickness
$[E]_x, [E]_y, [G]_{x,y}, [\nu]_{x,y}, [\nu]_{y,x}$	Laminate engineering constants

FIGURE 64: Procedure for predicting the laminate properties with the classical laminate theory (CLT)

5.1.2   FEM Setup for All The Designs

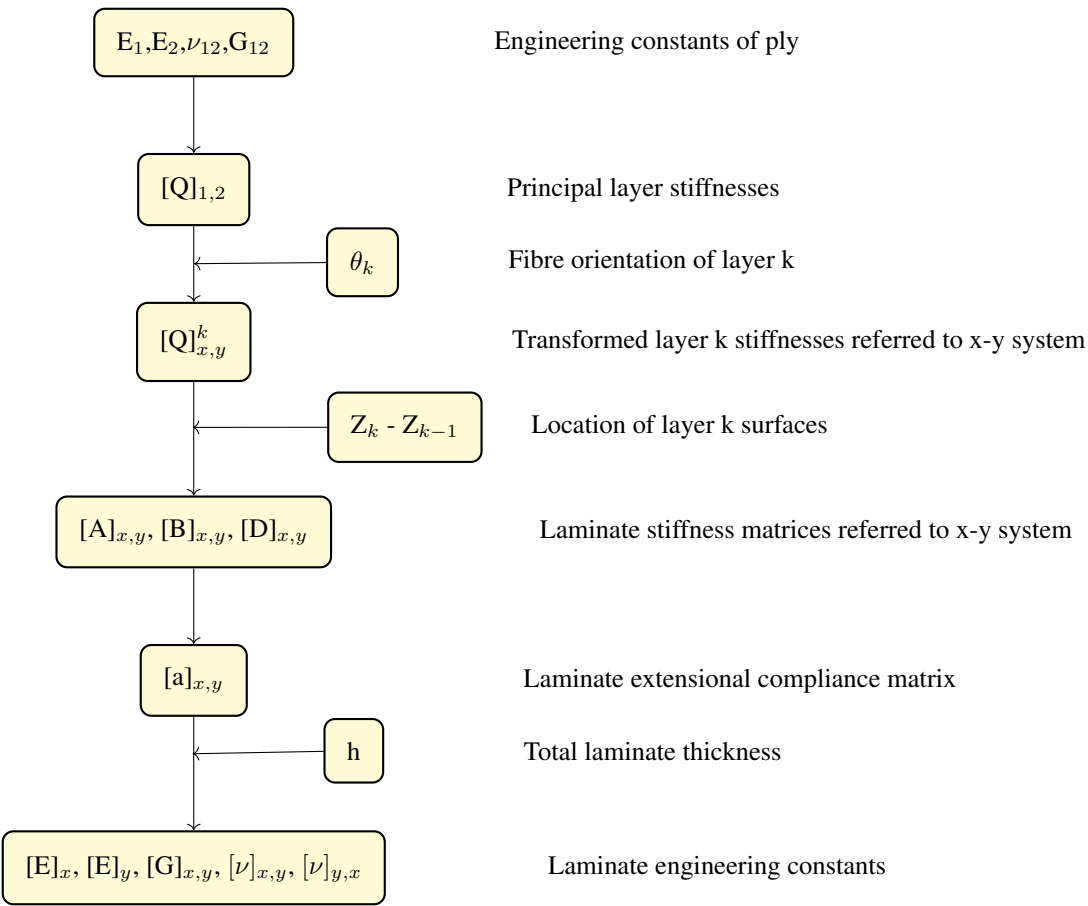Steady state heat transfer FEM was carried out with ABAQUS® and the heat flow through the structure was modelled with a vertical heat flux of $0.7\,\mathrm{W\,cm^{-2}}$ and a heat sink (inner surface of cooling pipe) at a temperature of $0\,°\mathrm{C}$ as shown in Figure 7. Every part was meshed with an 8-node linear heat transfer brick element DC3D8 (DC stands for heat transfer or mass diffusion, 3D stands for three dimensional, 8 stands for 8 node linear brick element).

In order to predict the behaviour of the stave under static and thermomechanical loading (detailed explanations are given in Chapter 1), finite element modelling towards calculating the deformations due to gravity loading, thermal cool down and pressure were performed under the implicit scheme. To predict the natural frequencies and the mode shapes of the structure, eigenvalue analysis were also performed.

The designs described in Sections 5.2 - 5.4 represent the stave for the inner detector layer L0. The stave designs were developed with a length (L) of $750\,\mathrm{mm}$. The boundary conditions were imposed by fully clamping the ends of the stave along with sliding support in the middle (Figure 10). The parts based on composite materials were meshed in ABAQUS® with continuum shell element SC8R with single element through the thickness and the non-composite parts were meshed with solid element C3D8R (C3D8R : C stands for continuum stress/displacement, 3D stands for three dimensional, 8 stands for 8 node linear brick element, R stands for reduced integration).

5.2   Fishbone Stave

The Fishbone stave was the first stave design to be developed within this research. The design was developed with (Figures 65 and 66) the unidirectional fibre plates, that could be glued between the face plate (composite laminate) and the carbon fibre cooling pipe so that the power (heat) generated by the electronics could be dissipated through the unidirectional fibre plates.

By this approach, the thermomechanical behaviour could be improved significantly, the total radiation length of the stave could also be reduced. First, a flexible CAD model (Figure 66) was developed in CATIA® V5 with fixed width of $18.8\,\text{mm}$ and fixed stave length of $750\,\text{mm}$. The description of different parts along with their material configuration, thickness and composite lay up are shown in Table 23.
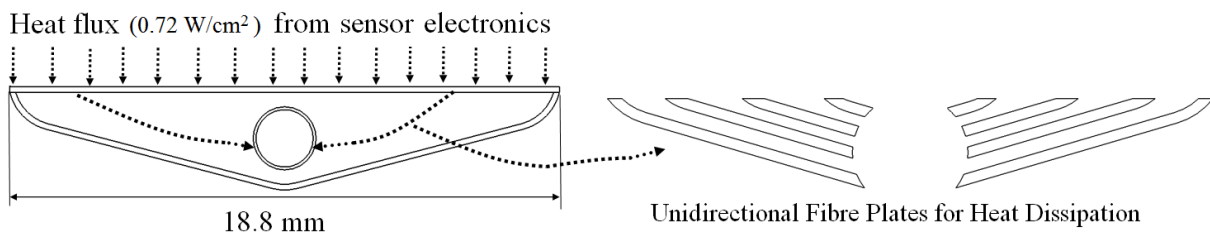
FIGURE 65: Development of the initial idea towards the improvement of the heat transfer behaviour with the Fishbone stave design
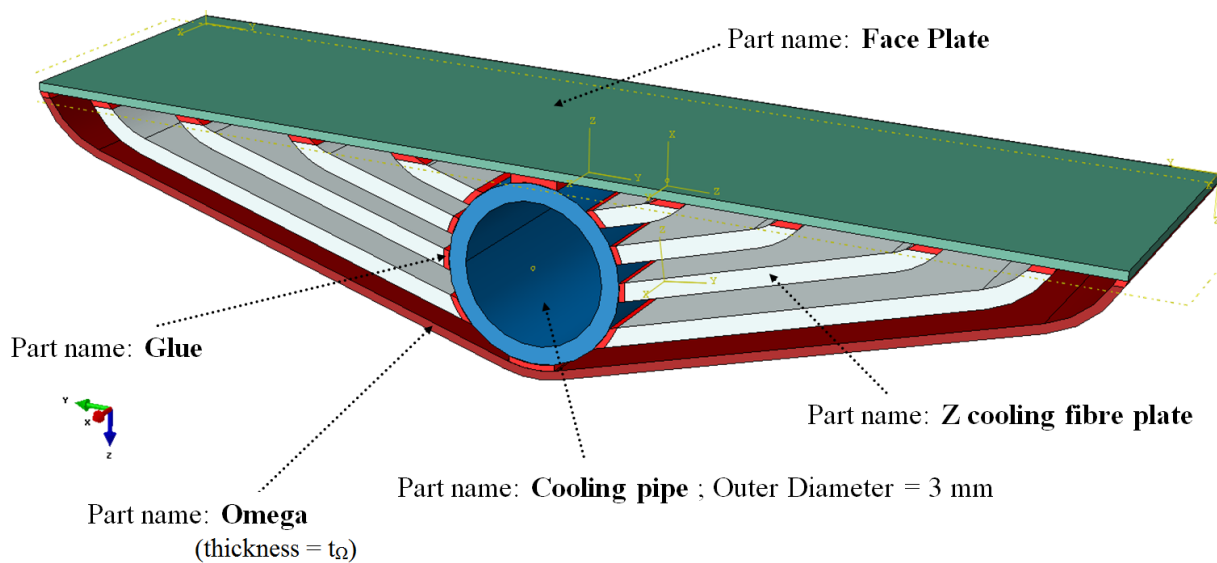
FIGURE 66: Description of the Fishbone stave

Part	Layup		Thickness	
	Fishbone 1	**Fishbone 2**	**Fishbone 1**	**Fishbone 2**
Face Plate	[0/90/0]		0.15 mm	
CF Pipe	$[\pm 45/\overline{0}]_s$		0.3 mm (WT)	
Z fibre plate	[0/90/0]		0.15 mm	
Glue			0.1 mm	
Omega	[0/90/0]	$[0/60/-60]_s$	0.15 mm	0.3 mm

TABLE 23: Different parts and their materials in Fishbone stave 1 and 2

5.2.1 Fishbone Stave 1

For the initial design (Fishbone stave 1) as shown in Figure 66, the thickness of the Face plate and Omega (t_Ω) were kept as $0.15\,$mm. The diamond powder filled carbon fibre cooling pipe was developed with an outer diameter of $3\,$mm and a wall thickness (WT) of $0.3\,$mm. It was also considered, that the face plate could be developed with DP filled laminate, as it would enhance the thermal behaviour along with the unidirectional Z fibres. The materials for the different parts along with their thickness and the composite layup are shown in Table 23. Deformation due to gravity and eigenvalue analysis were not carried out in this design. The heat transfer behaviour of the fishbone stave 1 showed an initial impression of possible improvements with the unidirectional Z fibre plates but the results showed that heat transfer being sensitive with the position of the fibre plates. It could be seen in Figure 67, that the hot spots are concentrated at the edges of the omega and face plate and the maximum heat from the face plate was dissipated through the unidirectional Z fibre plates and the carbon fibre pipe provides adequate cooling. The region where the carbon fibre pipe contacts the face plate was perfectly cooled. The results for deformation by thermal cool down are shown in Figure 68 and the maximum deformation happens to be in the middle as the stave bends in the Z-axis.
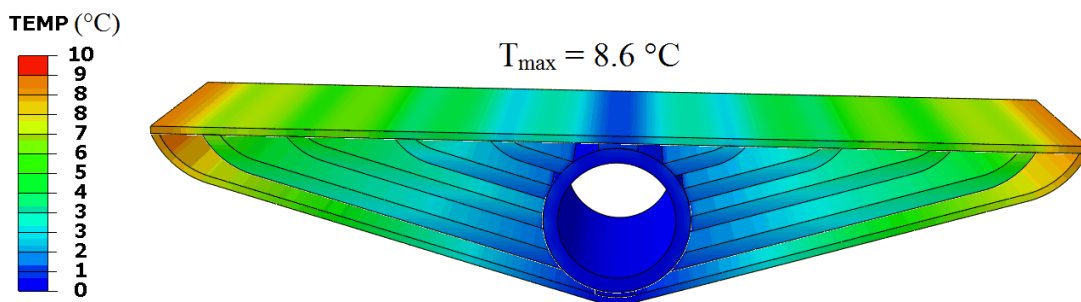
FIGURE 67: The heat transfer behaviour of the stave with a maximum temperature of $8.6\,°$C

The total (number of) radiation length of the stave (Table 24) is only $0.3\,\%$. The maximum temperature of the stave was $8.65\,°$C, with a thermal figure of merit (TFM) of $12\,°$C cm^2 W^{-1} which is close to the requirement of $15\,°$C cm^2 W^{-1} (Table 1). The deformation by pressure was $9\,\mu$m (Figure 68) and the deformation due to thermal cool down was $99\,\mu$m (Figure 68).
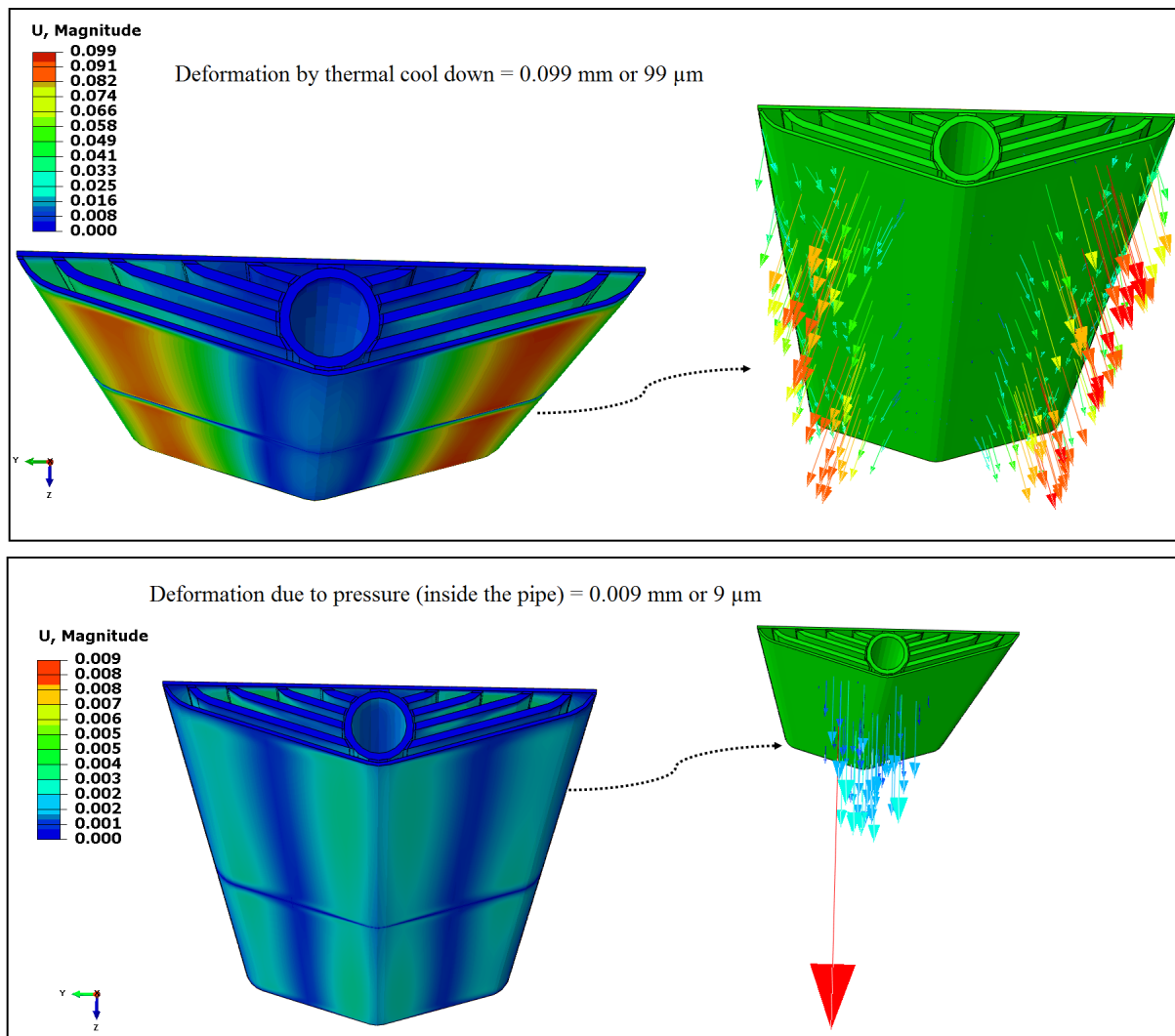
FIGURE 68: Deformations due to thermal cool down and pressure of $150\,\mathrm{bar}$

This design would require further optimisation as the conductive thermal figure of merit of the stave including the electronics has to below $15\,^{\circ}\mathrm{C}\,\mathrm{cm}^2\,\mathrm{W}^{-1}$ and the deformation by thermal cool down including the electronics has to be below $100\,\mu\mathrm{m}$ (Table 24).

5.2.2   Shape Optimisation of Fishbone Stave 1

The shape optimisation of the Fishbone stave 1 was performed with the assistance from Mr. Padala. The optimisation process was performed in Optimus®, which is a process integration and design optimization software. This software bundles a collection of design exploration and numerical optimization methods. The main objective of this optimisation activity was to improve the heat transfer behaviour of the stave design. The design variables are an input to the optimisation and in this research the position and the distance between the fibre plates were specified as design variables (Figure 69). The distance between the first and second fibre plate, second and third fibre plate and the distance between the third and the fourth fibre plates were specified as $d_1 = 3.4$ to 4.3 mm, $d_2 = 5.4$ to 6.3 mm , $d_3 = 7.4$ to 8.3 mm. The fibre plate bend

distance were specified as V = 0.9 to 1.1 mm. By this way it would be possible to understand the best position for the second and third and fourth fibre plates including an optimal distance between them.

FIGURE 69: The representation of design variables in the optimisation process

The constraints in the model were also defined. An objective function for predicting the maximum temperature on the face plate was defined as shown in Equation 5.1.

$$f(X) = \sum_{i=1}^{n} T_i(X) \tag{5.1}$$

where $f(X)$ is the objective function, X is the design variable, T is the maximum temperature (on the face plate) of the i-th element and n is the number of elements. The structure of optimisation process are shown in Figure 70. The input parameters were specified in the CATIA® model. A python script was used to develop the model set up in ABAQUS®. The CATIA® file and ABAQUS® python script including the objective functions were assigned in Optimus (Figure 70). The optimisation process was carried out in a batch mode. The cyclic process continued until optimised parameters were obtained.

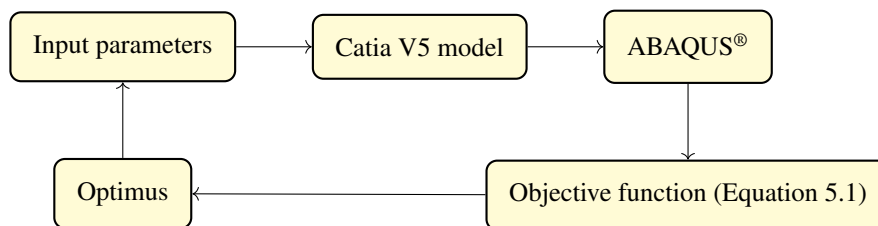FIGURE 70: Schematic representation of the optimisation process

5.2.2.1 Heat Transfer Behaviour After Shape Optimisation

After the optimisation procedure, a set of average values for the distance between the fibre plates were noted and then heat transfer FEM was performed to predict the maximum temperature on the face plate. The results shown in Figure 71 explains that the distribution of temperature

between the edges of the Face plate and Omega was reduced. The maximum temperature on the face plate (Figure 71) was also reduced to $8\,°C$ while the maximum temperature before the optimisation was $8.6\,°C$ which leads to an improvement of about $7\,\%$ in the reduction of the maximum temperature. The optimisation procedure was constrained based on the specified design variables and objective functions and an optimisation based on the topology could be one of an option for achieving more optimal design for the fibre plates and also to reduce the maximum temperature.
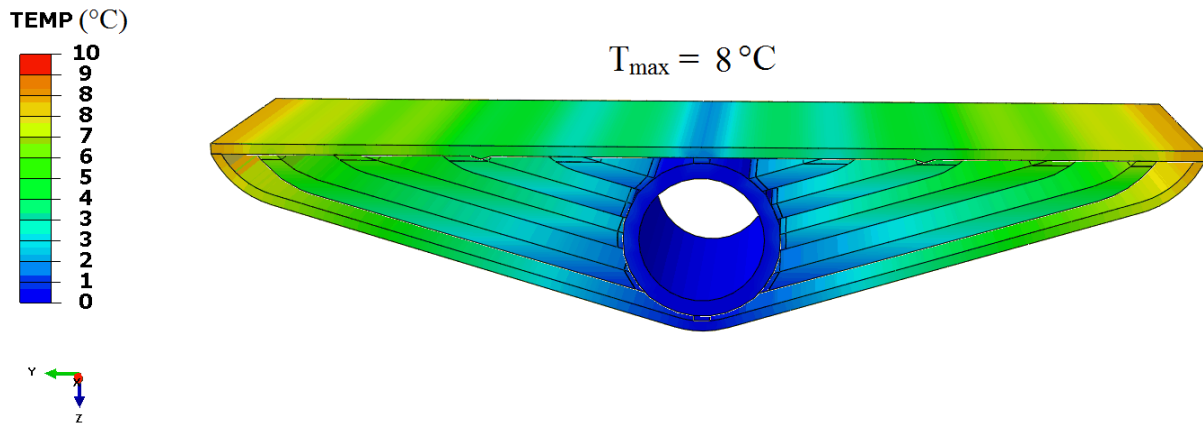

FIGURE 71: Maximum temperature on the surface of the face plate reduced to $8\,°C$ after the shape optimisation procedure

5.2.3   Fishbone Stave 2

In the previous design, the deformation by thermal cool down and the thermal figure of merit was very close to the specification limit. To improve the thermal behaviour and also to increase the stiffness in order to reduce the deformation by thermal cool down, the thickness of Omega (t_Ω) was increased to $0.3\,\mathrm{mm}$ (Figure 66). The fibre material of Omega was modified to YS80A (high modulus, high conductive fibre) and the laminate lay up of Omega was also modified to $[0/60/-60]_s$. Omega was considered as the fifth (cooling) fibre plate, as the thermal transport could be improved further. FEM results showed that the maximum temperature on the face plate was reduced and the deformation by thermal cool down also reduced signifcantly. The maximum temperature was reduced to $5.8\,°C$ with a thermal figure of merit of $8.05\,°C\,\mathrm{cm}^2\,\mathrm{W}^{-1}$. With this modified design, the hotspots at the edges between face plate and omega were reduced and the maximum temperature was concentrated on the region where the Z fibre plates did not had contact to the face plate (Figure 72). Normally in mechanics, an increase in the thickness leads to an increase in the stiffness and the deformation due to thermal cool down was reduced to $56\,\mathrm{\mu m}$ with $0.3\,\mathrm{mm}$ thick omega (Table 24). The increase in thickness of Omega provided a better thermal and thermomechanical behaviour. Overall, when compared to the fishbone stave 1, the design 2 showed a better behaviour (Table 24) with all the required parameters within the specification limit.
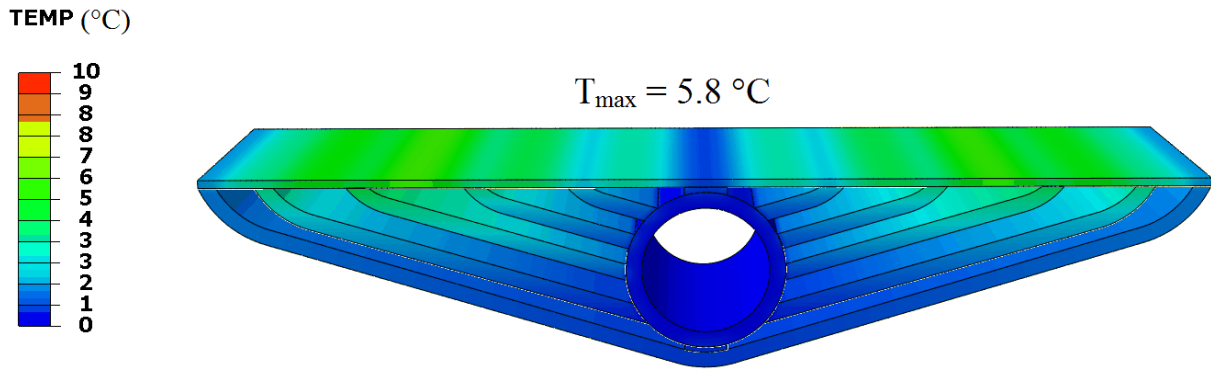
TEMP (°C)

$T_{max} = 5.8$ °C

FIGURE 72: Improved heat transfer behaviour with the fishbone stave 2

5.2.4 Summary

The Fishbone stave 1 showed the possibility to reduce the thermal figure of merit. The shape optimisation of the Fishbone stave 1 was carried out by modifying the distances between the cooling fibre plates. The heat transfer FEM after the optimisation, showed further reduction in the maximum temperature (on the ends of Face plate)(Table 24). The Fishbone stave 2 was developed by increasing the thickness of Omega. This design provides a solution that satisfies all the design requirements (Table 24) for the upgrade of the stave support structure. Overall in terms of manufacturing possibility, the Fishbone stave design would be complicated to achieve an accurate positioning of the Z fibre plates. It would also be difficult to provide a perfect contact with the cooling pipe. It is worth to note that the total height of the stave is only 3.5 mm. Based on the manufacturing complexities, this stave design concept would not be considered towards the development of prototype.

Design	Maximum Temperature	Thermal Figure of Merit	Thermal Cool Down	Pressure Deformation	X/X_0
	(°C)	(°C cm² W⁻¹)	(µm)	(µm)	(%)
Fishbone Stave 1	8.65	12	99	10	0.3
Optimisation	8	11			0.3
Fishbone Stave 2	5.8	8.05	56	9	0.36
	< 10.5	< 15	< 100	< 100	< 0.5

TABLE 24: Comparison of the FEM results of the Fishbone Stave 1 (including optimisation) and Fishbone Stave 2

5.3   Iso-Graphite Stave

The Iso-Graphite stave was developed after considering the manufacturing difficulties of the Fishbone stave. The Graphite FU2590[TM] material considered in this research was produced by Schunk Kohlenstofftechnik GmbH (Table 25). This graphite material has a thermal conductivity (isotropic) of $110\,\mathrm{W\,m^{-1}\,K^{-1}}$, which would help to take away the maximum heat from the sensor electronics. The electronics can be glued directly on top of the graphite as there would not be any problem due to the glue penetration or also due to the carbon dust. In this way, a Face plate would not be required. Hence, the production cost and the material budget can be reduced.

Physical and mechanical properties	Graphite FU2590
Density	$1.88\,\mathrm{g\,cm^{-3}}$
Bending strength	$50\,\mathrm{MPa}$
Tensile strength	$30\,\mathrm{MPa}$
Compressive strength	$110\,\mathrm{MPa}$
Young's modulus	$10\,\mathrm{GPa}$
Thermal conductivity	$110\,\mathrm{W\,m^{-1}\,K^{-1}}$ (Isotropic)

TABLE 25: Physical and mechanical properties of Graphite FU2590[TM] [85]

5.3.1   Initial Designs

The initial designs of the Iso-Graphite stave was developed with a round (a) and a rectangular (b) style of the graphite, which was split horizontally (Figure 73).
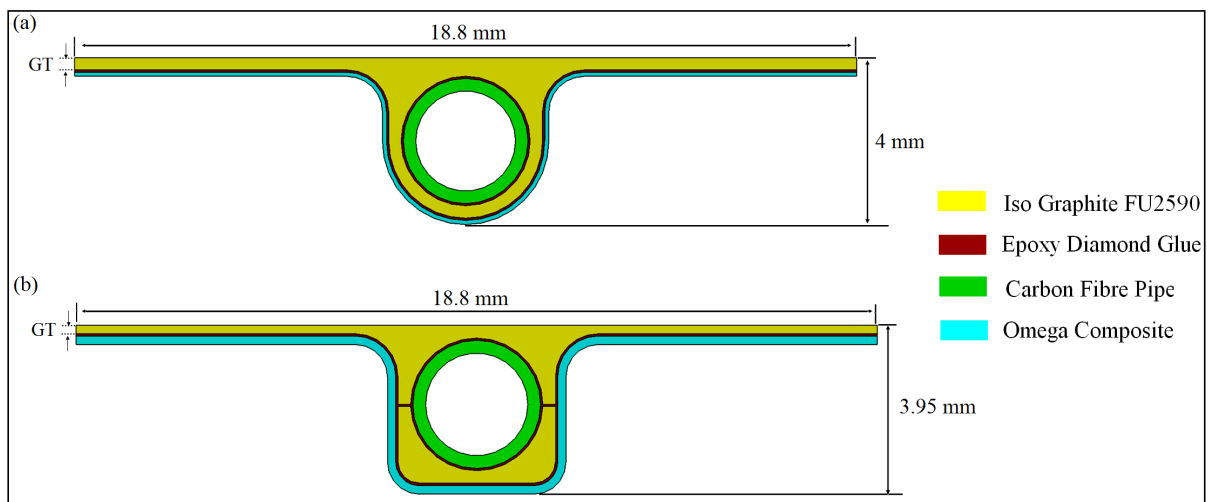

FIGURE 73: Development of the Iso-Graphite stave with a round (a) and a rect-
angular (b) style of the graphite

In both the design, the DP filled carbon fibre pipe was glued between the graphite. An Omega was glued to the graphite in order to add stiffness to the stave. In these two designs, the wing

thickness (GT) of the graphite varied between $0.3\,\text{mm}$ and $0.2\,\text{mm}$ respectively (Table 26). In the same way, the thickness of the Omega varied between $0.1\,\text{mm}$ and $0.2\,\text{mm}$ respectively (Table 26). Finite element modelling was carried out for both these designs. It was observed from the FEM, that the thermal and thermomechanical behaviour of the stave was within the requirement. However, both these designs were scrapped due to considerable manufacturing difficulties. It was learnt that it would be difficult to mill the fragile graphite material with a round and a rectangular style with a horizontal split.

Part	Material	Lay up	Thickness	
			Iso Graphite Round	**Iso Graphite Horizontal Split**
Iso-Graphite	Graphite FU2590		$0.3\,\text{mm}$	$0.2\,\text{mm}$
Omega	T300/Epoxy	[0/90/0]	$0.1\,\text{mm}$	$0.2\,\text{mm}$
CF Pipe	T300 / Epoxy Diamond(6 vol %)	$[\pm45/\overline{0}]_s$	$0.3\,\text{mm}$ (WT)	$0.3\,\text{mm}$ (WT)
Glue	Epoxy-Diamond		$0.05\,\text{mm}$	$0.05\,\text{mm}$

TABLE 26: Details of the design specifications of the Iso-Graphite Round and Horizontal Split

5.3.2 Iso-Graphite Vertical Split

The Iso-Graphite Vertical Split as shown in Figure 74 was developed with a vertical separation with smooth corners in order to avoid stress concentrations and also to reduce the manufacturing difficulties. The wing thickness of the graphite (GT) and the wall thickness (WT) of the pipe were both reduced to $0.2\,\text{mm}$ (Figure 74). After consulting with Barthels-Feldhoff® GmbH, it was learnt that the carbon fibre (standard modulus T300 fibre) pipe could be braided with an orientation of $\pm45°$ and with a wall thickness of $0.2\,\text{mm}$. These details were updated in the model (Figure 74).
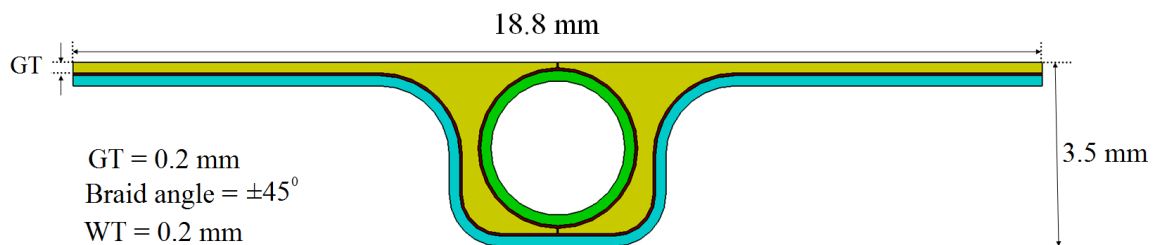

FIGURE 74: Development of the Iso-Graphite Vertical Split stave design

5.3.2.1 FEM Results

In addition to thermal and thermomechanical FEM, eigenvalue analysis were carried out to predict the natural frequencies and the mode shapes of the design. The heat transfer behaviour

was much improved, where the maximum temperature was reduced to $9\,^\circ\text{C}$ (with diamond powder in the pipe). A comparison for the enhancement of the heat transfer behaviour without and with diamond powder in the carbon fibre pipe is shown in Figure 75.
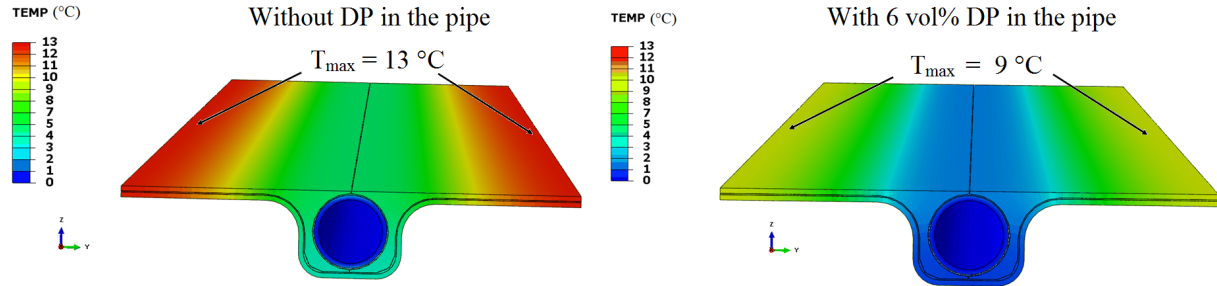

FIGURE 75: Comparison of the heat transfer behaviour with and without diamond powder (DP) for the Iso-Graphite Vertical Split stave

The deformations by the thermal cool down and by pressure was $68\,\mu\text{m}$ and $11\,\mu\text{m}$ respectively (Table 27). Eigenvalue analysis for the first six natural frequencies and the mode shapes of the stave design was carried out. It was observed that the first natural frequency of the design was $122.19\,\text{Hz}$ (Table 27).

Realistically, no major manufacturing difficulties are expected towards the production of this stave design. Considering the material budget and the requirement to achieve a low thermal figure of merit ($\approx 5\,^\circ\text{C cm}^2\,\text{W}^{-1}$), an investigation was carried out by varying the wing thickness of the graphite (GT).

5.3.2.1.1 Parametric Modifications

A parametric modification was performed by varying the wing thickness of the graphite (GT) from $0.2\,\text{mm}$ to $0.3\,\text{mm}$, $0.4\,\text{mm}$ and $0.5\,\text{mm}$ respectively (Figure 76). Finite element modelling was carried out for predicting the structural, thermal and thermomechanical behaviour of the stave.
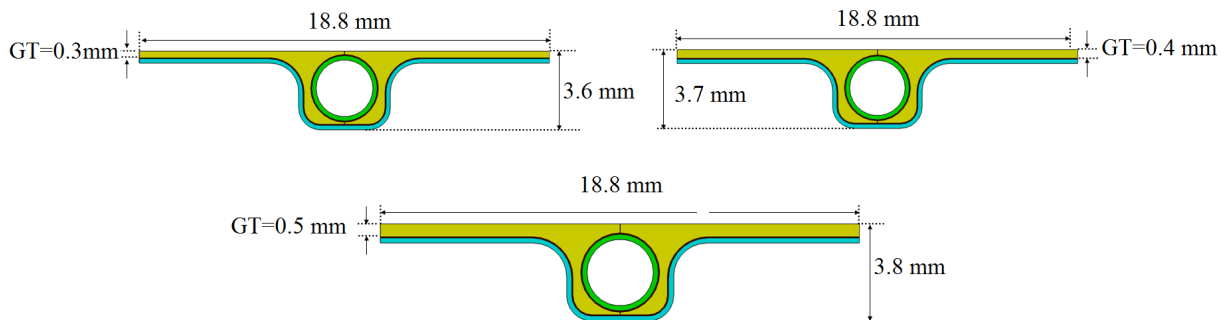

FIGURE 76: Parametric modifications of the Iso-Graphite Vertical Split stave design with different wing thickness of the graphite (GT)

A comparison of the heat transfer for the stave design with and without the parametric modifications are shown in Figure 77 and in Table 27. It could be seen for the design with the graphite wing thickness (GT) of $0.5\,$mm, the heat transfer behaviour was further improved and the maximum temperature was reduced to $5\,°$C with a thermal figure of merit of $7\,°$C cm^2 W^{-1}.
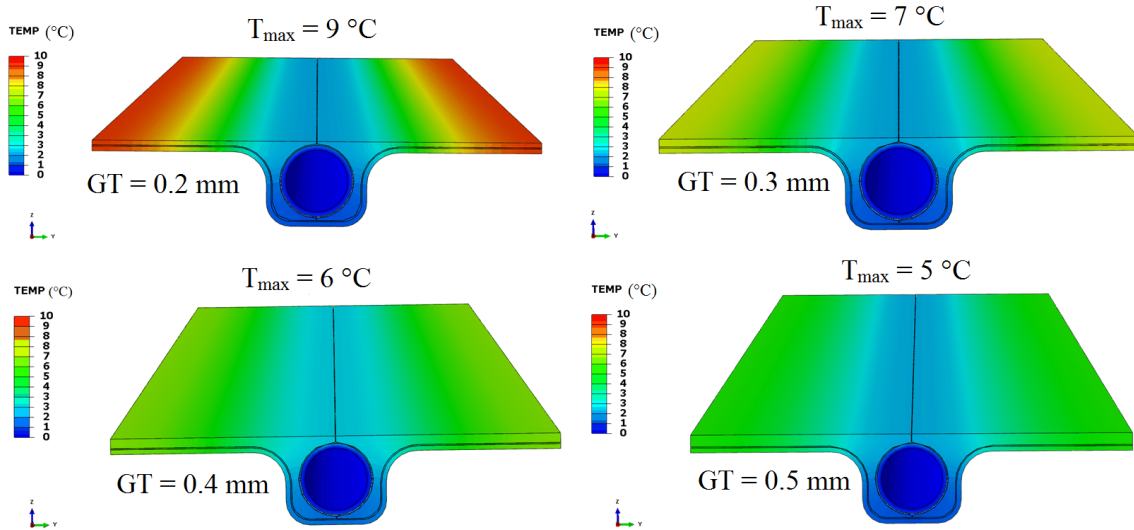

FIGURE 77: Comparison of the FEM heat transfer results after the parametric modifications, showing a reduction in the thermal figure of merit of the stave by modifying the graphite wing thickness (GT)

GT	Maximum Temperature	Thermal Figure of Merit	Thermal Cool Down	Pressure Deformation	Gravity Sag	Mode 1 Frequency
(mm)	(°C)	(°C cm^2 W^{-1})	(µm)	(µm)	(µm)	(Hz)
0.2	9	12.9	68	11	19	122.19
0.3	7	10	45	5	20	117.91
0.4	6	8.6	41	4	22	112.65
0.5	5	7	46	3	24	108.75
Requirement	< 10.5	< 15	< 100	< 100	< 100	> 50

TABLE 27: Comparison of the overall FEM parametric modification results of the Iso-Graphite Vertical Split stave

By increasing the GT, the deformations by the thermomechanical loading was significantly reduced (Table 27), as the stiffness of the structure increases with the increase in thickness. Considering the overall results, the Iso-Graphite stave with the GT of $0.5\,$mm could be a better option as the maximum temperature and the thermal figure of merit are quite minimal, the thermomechanical behaviour are also enhanced and the increase in the total (number) radiation length of the stave (Figure 78) could compromise for the total improved performance. A

comparison shown in Figure 78 explains the relationship between the total number of radiation length (X/X_0) and the thermal figure of merit. This is done by considering the carbon fibre pipe filled without and with the diamond powder. It could be seen in Figure 78, that the thermal figure of merit of the stave (after parametric modifications) has been reduced at the compromise of the total number of radiation length (X/X_0). The comparisons with and without diamond powder in the pipe (Figures 78,79 and Table 28) are shown in order to observe an improvement in the heat transfer behaviour. It would be interesting to note that, when having the GT of $0.5\,\mathrm{mm}$ and without DP in the pipe, the thermal figure of merit of the stave was $12\,^\circ\mathrm{C\,cm^2\,W^{-1}}$. At the same GT $(0.5\,\mathrm{mm})$ but with the DP filled carbon fibre pipe, the thermal figure of merit of the stave reduced to $7\,^\circ\mathrm{C\,cm^2\,W^{-1}}$ (Figure 78, 79). This shows an improvement by about $5\,^\circ\mathrm{C\,cm^2\,W^{-1}}$ with DP in the carbon fibre pipe.
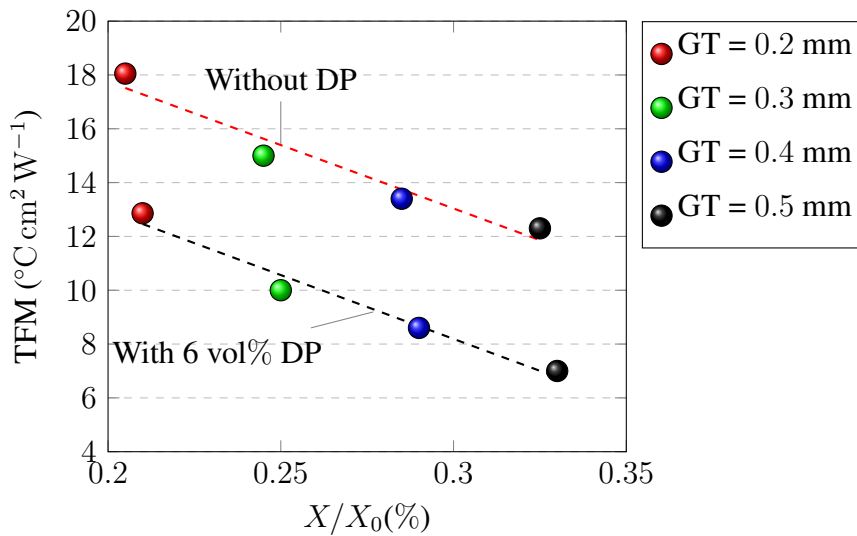
FIGURE 78: Comparison of the total number of radiation length (X/X_0) with the thermal figure of merit (TFM) without and with diamond powder (DP) in the carbon fibre pipe by varying the wing thickness of the graphite (GT)

GT	Thermal Figure of Merit		X/X_0	
	Without DP	With DP	Without DP	With DP
mm	$(^\circ\mathrm{C\,cm^2\,W^{-1}})$	$(^\circ\mathrm{C\,cm^2\,W^{-1}})$	(%)	(%)
0.2	12.86	18.05	0.205	0.21
0.3	10	15	0.245	0.25
0.4	8.6	13.4	0.285	0.29
0.5	7	12.3	0.325	0.33
Requirement	<15	<15	<0.5	<0.5

TABLE 28: Comparison of the thermal figure of merit and the X/X_0 without and with DP in the pipe
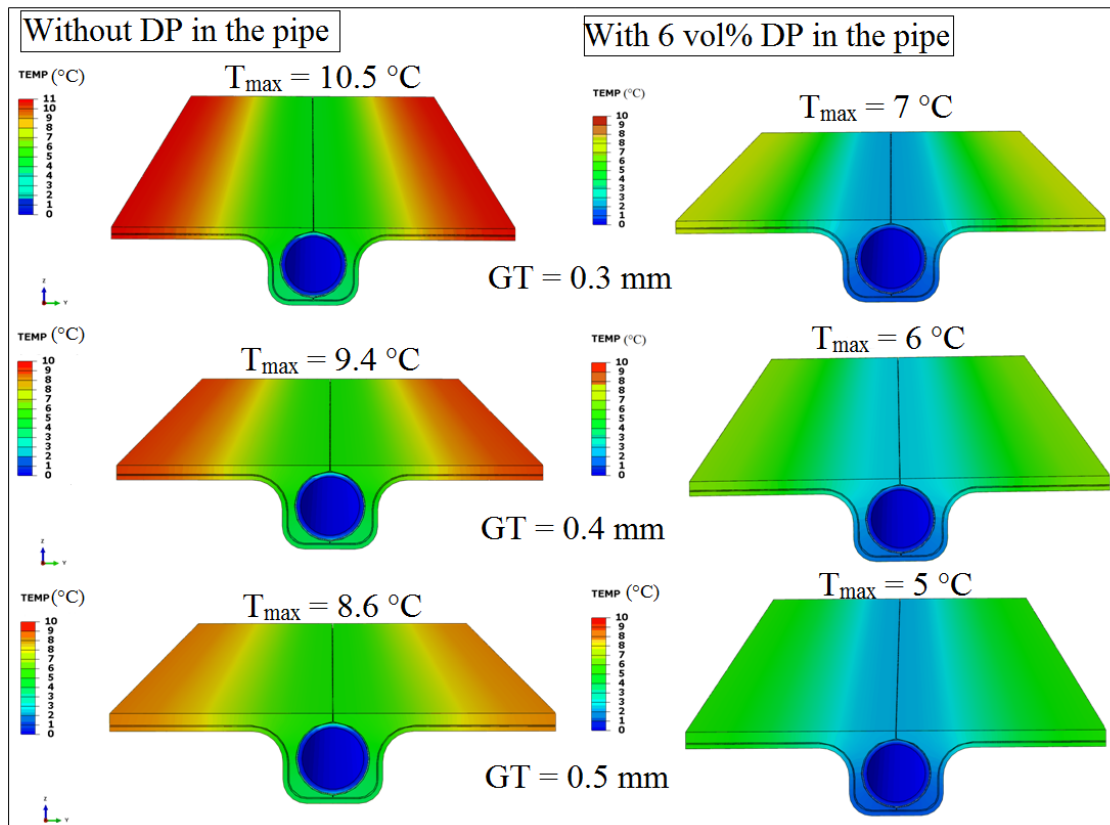
FIGURE 79: Comparison of the heat transfer FEM results without and with 6 vol% of diamond powder in carbon fibre pipe by varying the GT

Overall, no significant manufacturing difficulties are foreseen for the production of the Iso-Graphite Vertical Split stave. This design is quite adjustable according to the requirements of each detector layer. Moreover, the FEM results show that the most demanding requirements can be met. In particular a thermal figure of merit of $7\,^{\circ}\text{C}\,\text{cm}^2\,\text{W}^{-1}$ along with the total number of radiation length of $0.33\,\%$ are the highlights of this design.

5.4   Stiffener Stave

The stiffener stave design was developed with an objective to utilise the cooling through multiple pipes. With this approach, the heat transfer behaviour could be improved by several folds without using additional conductive materials like graphite or foam within the structure.

5.4.1   Initial Designs

5.4.1.1   Two Pipes Stiffener

The Two Pipes Stiffener was developed (Figure 80) as a tubular structure that could be braided with the high modulus (YS90A) carbon fibre with a thickness of $0.15\,\text{mm}$. The design consisted of five inner chambers and they were of ellipsoidal shape. Two of these chambers were considered as cooling pipes. The space in the other inner chambers could be used, for example like placing electronic cables. The sections between the chambers will act as a stiffener in order to reduce the deformation due to thermomechanical loading. Heat transfer FEM result (Figure 81) showed the maximum temperature of $7.8\,^\circ\text{C}$ with a thermal figure of merit of $11.1\,^\circ\text{C}\,\text{cm}^2\,\text{W}^{-1}$. Other FEM results are shown in Table 29, where one could observe a higher stiffness of the stave due the high modulus YS90A composite. It was found from the FEM results that, due to ellipsoidal shape of the pipe, the deformation by pressure was bit higher.
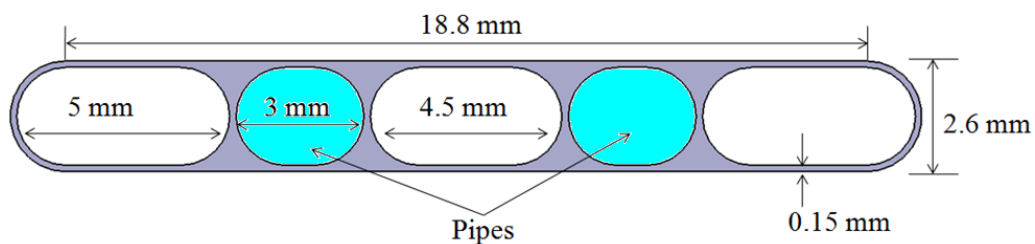

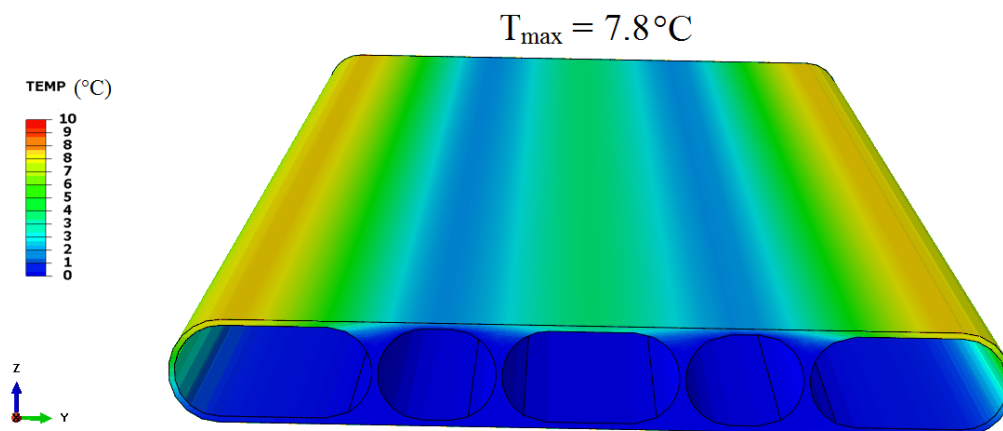FIGURE 80: Development of the Stiffener stave with two ellipsoidal pipes

FIGURE 81: Heat transfer FEM of Two Pipes Stiffener stave

5.4.1.2 Three Pipes Stiffener

The Three Pipes Stiffener design was developed with circular chambers of diameter of $2.2\,\mathrm{mm}$ (Figure 82). Three cooling pipes were considered in order to reduce the maximum temperature. Parametric modifications were performed in order to select which of the three inner chambers would be the cooling pipes. The FEM results (Figure 81) showed that the maximum temperature was substantially reduced to $3.56\,^{\circ}\mathrm{C}$ with a thermal figure of merit of $5.1\,^{\circ}\mathrm{C}\,\mathrm{cm}^2\,\mathrm{W}^{-1}$. The deformation by pressure was further reduced (Table 29).
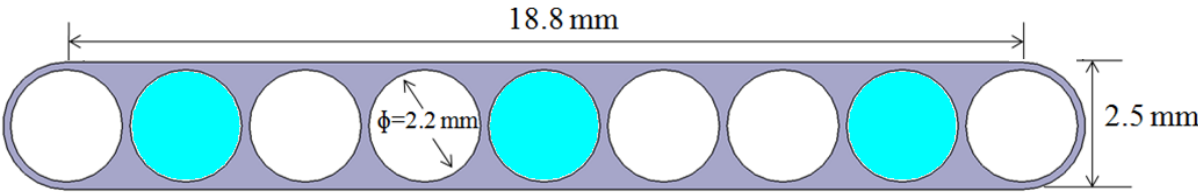
FIGURE 82: Development of Three Pipes Stiffener stave
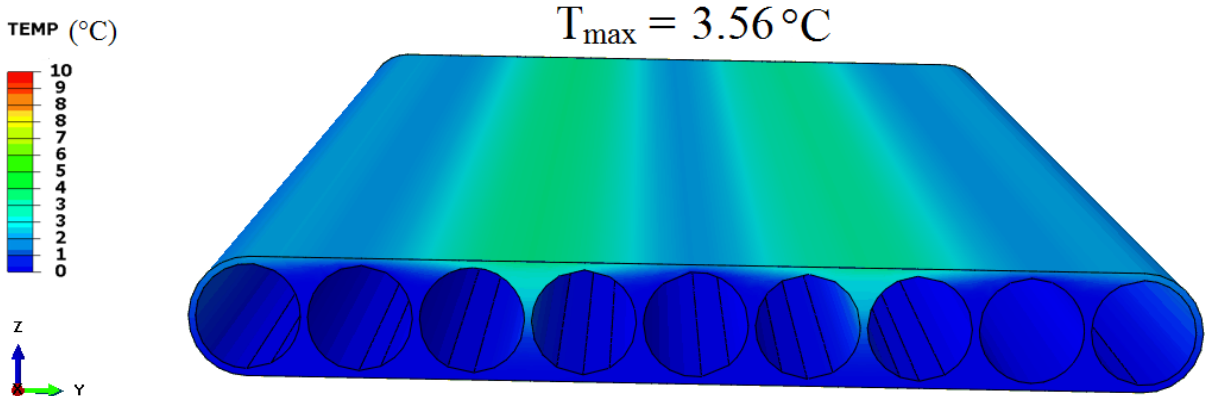
FIGURE 83: Heat transfer FEM of Three Pipes Stiffener stave with a thermal figure of merit of $5.1\,^{\circ}\mathrm{C}\,\mathrm{cm}^2\,\mathrm{W}^{-1}$

Manufacturing Difficulties:

After discussing with the experts at Barthels-Feldoff® GmbH, it was learnt that after considering the thickness ($0.15\,\mathrm{mm}$) and the height ($2.5\,\mathrm{mm}$) of the stave, the Two and Three Pipes Stiffener would need to be scrapped due to manufacturing difficulties. It would be impossible to braid the high modulus YS90A fibre as a continuous structure even with 1K (1000) fibre filaments as it would be quite fragile to handle.

5.4.2   Nine Pipes Stiffener

To overcome the manufacturing problems of the previous designs (Two and Three Pipes Stiffener), Nine Pipes Stiffener was developed with nine cooling pipes which could be individually braided with the standard modulus T300 fibre with an orientation of $\pm45°$ (Figure 84). Since the T300 fibre's are not highly conductive when compared to the high modulus (YS90A) carbon fibres, multiple cooling pipes must be used in order to improve the thermal behaviour. The design was developed in such a way that the nine braided pipes with an outer diameter of $2\,\mathrm{mm}$ and an inner diameter of $1.6\,\mathrm{mm}$ would be assembled close together. By this way, a close contact between the fibres will improve the heat transfer behaviour. In order to add stiffness to the stave, the YS90A unidirectional fibres would be placed between the pipes so that it can act as a stiffener. Finally, a vacuum assisted impregnation process could be carried out with the epoxy-diamond powder (6 vol%) in order to finish the stave production (Figure 84).
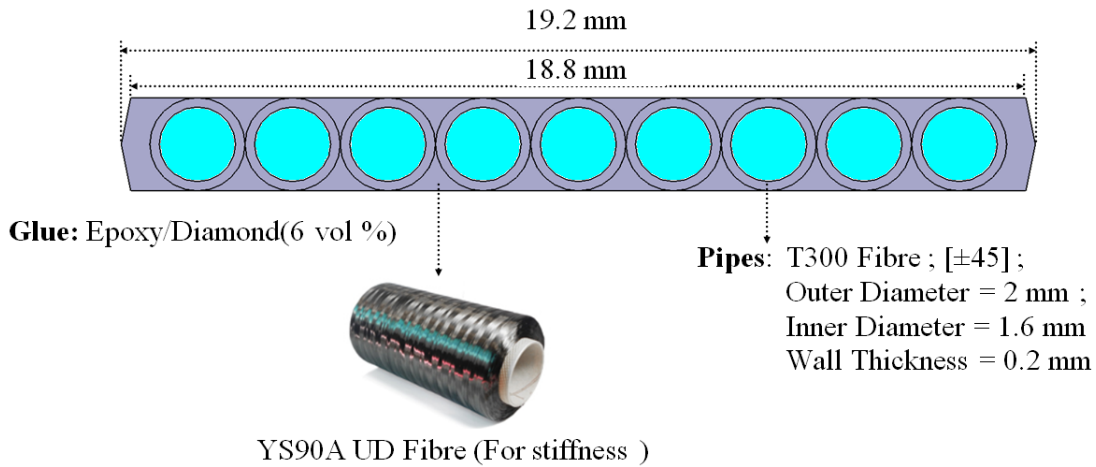
FIGURE 84: Development of Nine Pipes Stiffener stave design

Finite element modelling was performed and the analysis showed that the maximum temperature was reduced to $5.3\,°\mathrm{C}$ (Figure 85). The natural frequency and the deformations due to the structural and thermal loadings were within the requirement (Table 29). Even though the FEM results were promising, this design had to be scrapped as it was learnt that, Barthels-Feldoff® GmbH could not produce a braid with an outer diameter of $2\,\mathrm{mm}$. The design had to be modified and these are explained in the next design.
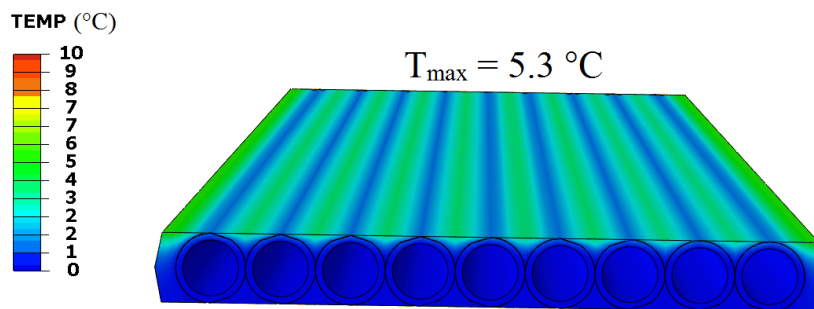
FIGURE 85: Heat transfer FEM showing a maximum temperature of $5.3\,°\mathrm{C}$

5.4.3 Eleven Pipes Stiffener

New design with eleven cooling pipes (Figure 86) was developed with a total stave width of
$20.35\,\mathrm{mm}$. As specified in the previous design, the eleven pipes were assembled in close contact
and the YS90A unidirectional fibres between them would increase the stiffness of the stave.

20.35 mm

18.5 mm

Glue: Epoxy/Diamond (6 vol%)

Pipes: T300 Fibre ; [±45] ;
Outer Diameter = 1.85 mm ;
Inner Diameter = 1.6 mm;
Wall Thickness = 0.125 mm

YS90A UD Fibre (For stiffness)
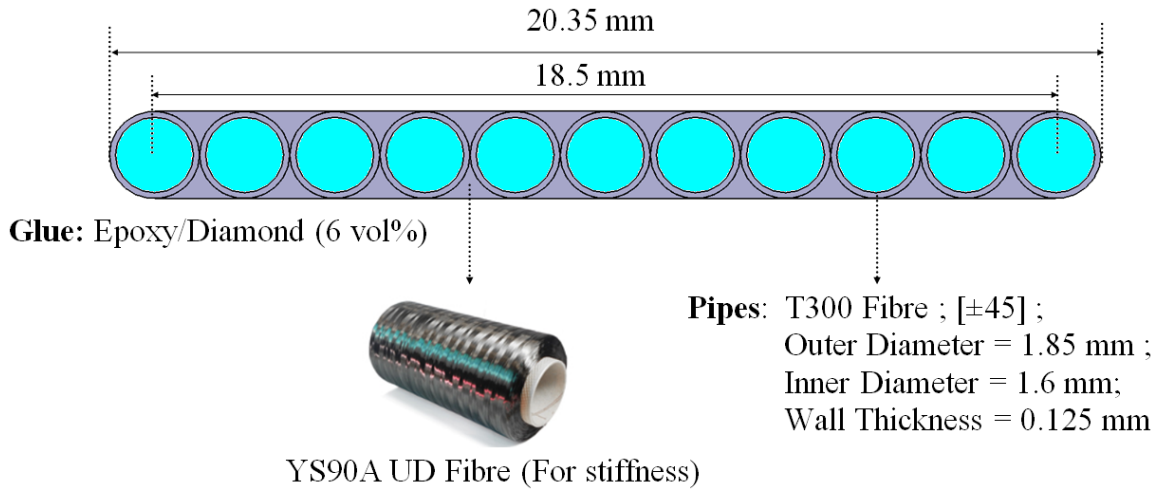
FIGURE 86: Development of the Eleven Pipe Stiffener stave with eleven cooling
pipes

Finite element results showed the significant reduction of the maximum temperature to $3.9\,^\circ\mathrm{C}$
(Figure 87) with a thermal figure of merit of $5.6\,^\circ\mathrm{C}\,\mathrm{cm}^2\,\mathrm{W}^{-1}$ (Table 29) and these reductions
are due to large volume of cooling within the structure. The deformation by gravity increased
to $65\,\mu\mathrm{m}$ and the deformation by thermal cool down and the pressure was $14\,\mu\mathrm{m}$ and $10\,\mu\mathrm{m}$
respectively (Table 29). The increase in the deformation by the gravity loading are due to the
reduction of the thickness and the height of the structure. It should be noted that the braided
composites have a low axial stiffness than the on-axis composites. When the thickness is re-
duced, the stability of the structure naturally reduces. However the resulting deformation by the
gravity loading is within the specification limit.

TEMP (°C)

$\mathrm{T_{max}} = 3.9\,^\circ\mathrm{C}$

FIGURE 87: FEM result showing an improvement in the heat transfer behaviour
of the stiffener stave with 11 pipes. The maximum temperature was only $3.9\,^\circ\mathrm{C}$

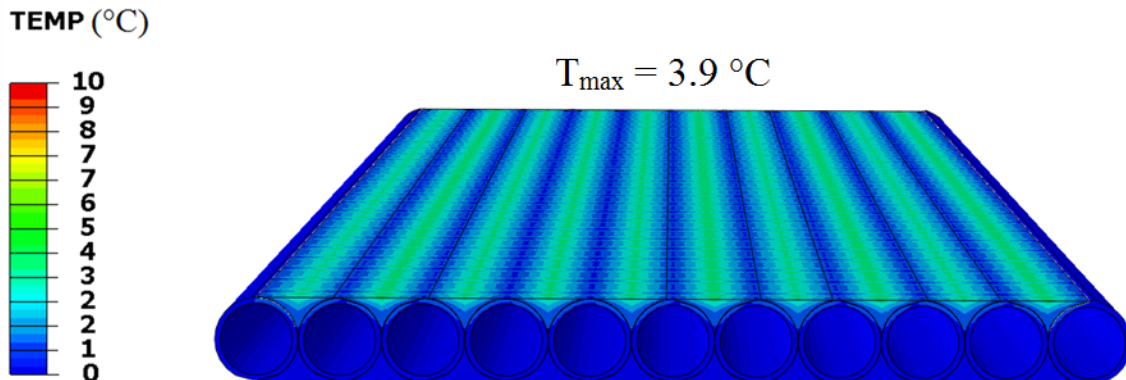| No. of Pipes	Maximum Temperature	Thermal Figure of Merit	Thermal Cool Down	Pressure Deformation	Gravity Sag	Mode 1 Frequency
	(°C)	($°C\,cm^2\,W^{-1}$)	(µm)	(µm)	(µm)	Hz
2	7.8	11.1	4	41	8	
3	3.56	5.1	3	4	9	
9	5.3	7.6	13	7	21	124.4
11	3.9	5.6	14	10	65	71
Requirement	< 10.5	< 15	< 100	< 100	< 100	> 50

TABLE 29: FEM results of the Stiffener stave with different cooling pipes

Figure 88 shows an investigation to achieve an optimal thermal figure of merit (TFM) for the Eleven Pipe Stiffener stave. The basic idea, is to see a relation between the TFM and the X/X_0 by varying the amount of cooling. The contribution of the CO_2 inside the pipe was considered while calculating the X/X_0. Five, six and eleven pipes were considered for cooling. The cooling in five and six pipes were applied symmetrically. From Figures 88 and 89 it could be observed that, with the increase in the number of pipes (filled with CO_2) , the TFM reduces at the expense of the total number of radiation length of the stave. Table 30 shows, how the X/X_0 of the stave changes with the number of pipes filled with CO_2. The heat transfer behaviour of the Eleven Pipes Stiffener stave with the cooling in five and six cooling pipes are shown in Figure 89. It could be observed that the maximum temperature is very high with the cooling in five and six pipes. An optimal behaviour could only be achieved with the cooling in all eleven pipes.
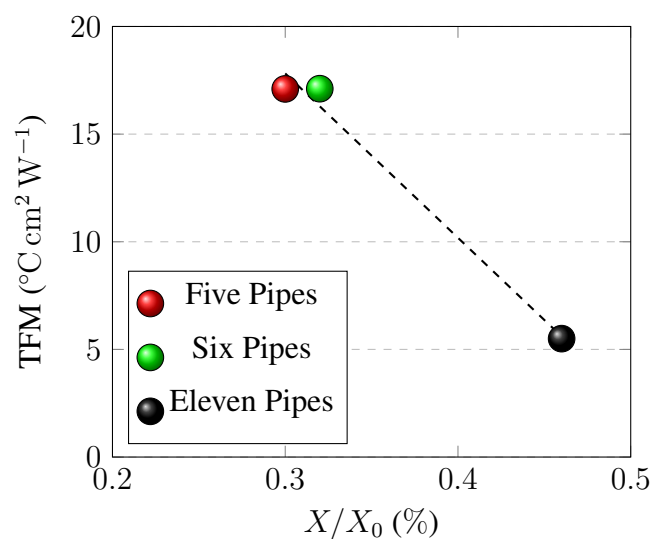
FIGURE 88: Comparison of the TFM with the X/X_0 of the Eleven Pipe Stiffener stave

No. of Pipes for Cooling in the Eleven Pipes Stiffener Stave	Thermal Figure of Merit	X/X_0	
		Without CO_2	With CO_2
	$(^\circ C\,cm^2\,W^{-1})$	(%)	(%)
5	17.1	0.164	0.3
6	17.11	0.164	0.32
11	5.5	0.164	0.46
Requirement	<15		<0.5

TABLE 30: Comparison of the thermal figure of merit and the X/X_0 without and with CO_2 in the pipe
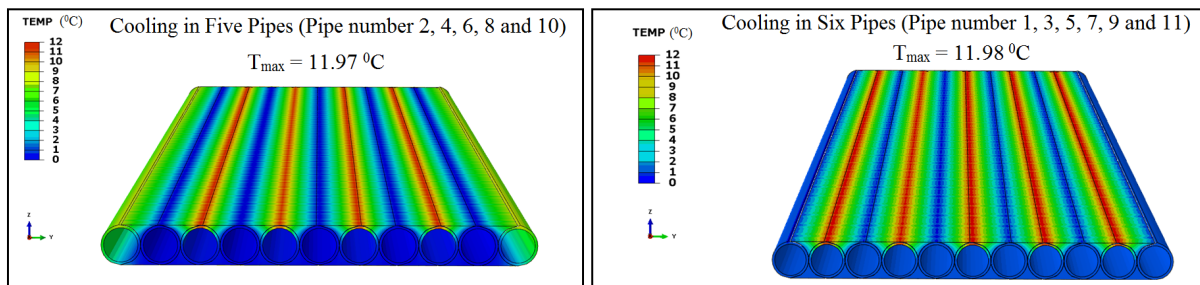
FIGURE 89: FEM heat transfer behaviour with cooling in five and six pipes

A comparison of the heat transfer behaviour without and with diamond powder in the pipe when applying the cooling in all pipes are shown in Figure 90. The maximum temperature without diamond powder in the pipe is $6.3\,^\circ C$ and with diamond powder it is $3.9\,^\circ C$. This would suggest the influence of diamond powder towards the heat transfer.
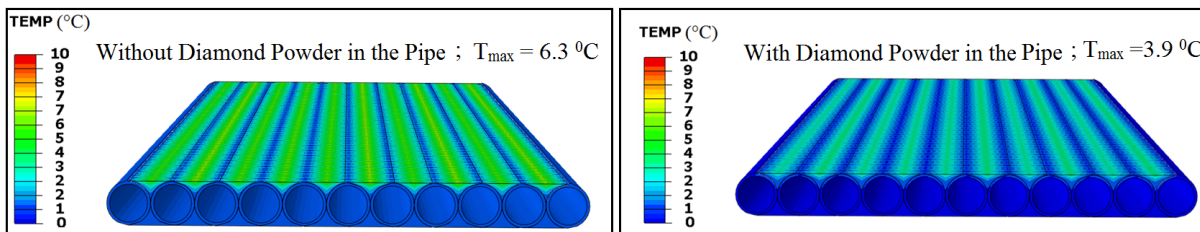
FIGURE 90: Heat transfer behaviour with and without DP in the pipe

5.5 An Overview of Preferred Stave Designs

A comparison of the best version of the Fishbone, the Iso-Graphite and the Stiffner stave's FEM results are shown in Tables 31 and 32.

In the Fishbone Stave 2, an Omega was considered as an additional cooling fibre plate. This helped to improve the thermal figure of merit (TFM) of the Fishbone Stave 2 when compared to that of the Fishbone Stave 1 and its optimisation technique. The results also showed that the deformations by the structural and the thermomechanical loadings were within the requirements (Table 32). However, the complexities regarding the Fishbone stave's manufacturing possibilities have been addressed before.

| Design	No. of Pipes	Thermal Figure of Merit ($^\circ\mathrm{C\,cm^2\,W^{-1}}$)	X/X_0 (%)
Fishbone Stave 2	1	8.05	0.36
Iso-Graphite Vertical Split (GT=0.5 mm)	1	7	0.33
Eleven Pipes Stiffener Stave	11	5.6	0.46
Requirement		< 15	< 0.5

TABLE 31: Comparison of TFM vs X/X_0 of the Fishbone, the Iso-Graphite and the Stiffener Stave designs

In the Iso-Graphite Stave, the graphite material improved the therml behaviour of the stave. Several parametric modifications were carried out in relation to the TFM vs X/X_0 by varying the wing thickness (GT) of the graphite. In particular, the Iso-Graphite Vertical Split with a GT of $0.5\,\mathrm{mm}$ is the preferred design among the other Iso-Graphite Stave designs. The thicker graphite enhances the heat transfer in order to achieve a lower thermal figure of merit (Table 31). The mode 1 natural frequency and the deformations due to the structural and thermomechanical loadings were well within the requirements (Table 31, 32). Overall, this design is quite robust, that it can satisfy any challenging requirements of other barrel layers (like L1, L2, L3 and L4).

The Stiffener Stave is a novel concept where, the multiple pipes filled with diamond powder forms a composite laminate. In this way, this design negates the requirement for different conductive materials. The Eleven Pipes Stiffener Stave provides the best solution among the other stave designs in terms of the TFM (Table 31, 32). The design is quite flexible, where the number of pipes filled with CO_2 can be varied in order to achieve the required TFM (Table 31). Structural and the thermomechanical FEM results were also within the requirement limit.

After this study, the Eleven Pipes Stiffener Stave and the Iso-Graphite Vertical Split (GT =0.5 mm) are the preferred designs. The development of a prototype based on these designs are discussed in the next section.

FEM Results				
Design	Maximum Temperature	Thermal Cool Down	Gravity Sag	Natural Frequency (Mode 1)
	(°C)	(μm)	(μm)	(Hz)
Fishbone Stave 2	5.8	56	10	131.86
Iso-Graphite Vertical Split (GT=0.5 mm)	5	46	24	108.75
Eleven Pipes Stiffener Stave	3.9	14	65	71
Requirement	< 10.5	< 100	< 100	> 50

TABLE 32: Comparison of the FEM results of the Fishbone, the Iso-Graphite and the Stiffener stave designs

5.6 Development of Prototypes

5.6.1 Iso-Graphite Stave

The prototyping process was carried out for the Iso-Graphite stave with and without the diamond powder in the carbon fibre pipe. The final drawing of the Iso-Graphite stave for the development of the prototype are shown in Figure 91.
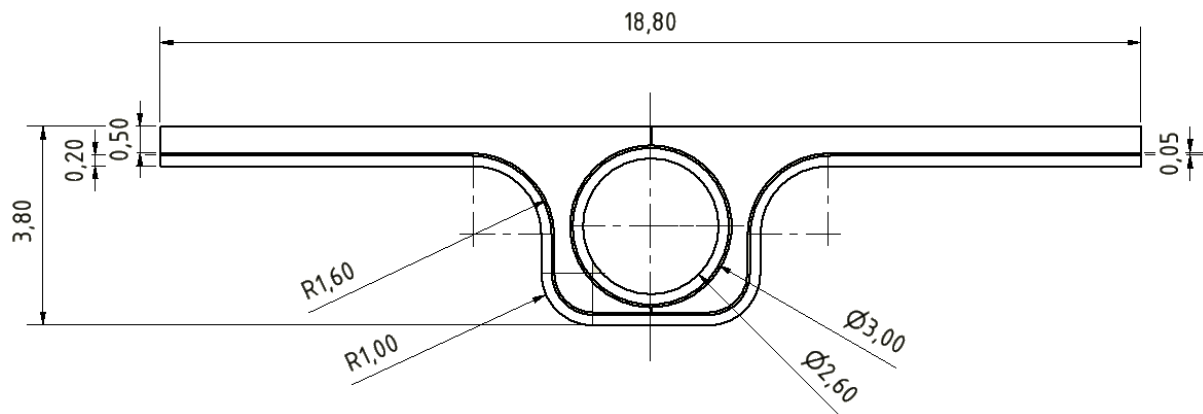

FIGURE 91: Generated associative drafting from 3D mechanical parts of the Iso-Graphite Vertical Split stave designed in Catia V5 (All dimensions are in mm)

In order to build the stave prototype, the tools were developed for producing the pipes, omega and for the stave final milling and assembly. The stave production process (Figure 92) began with the milling of the Iso-Graphite bulk which were supplied by Schunk Kohlenstofftechnik GmbH and three separate parts of the graphite were milled each upto a length of $250\,\mathrm{mm}$. In order to produce the carbon fibre pipe, standard modulus T300 carbon fibre braid (orientation of ±45) were supplied by Barthels-Feldoff® GmbH. The braiding process was carried out with a teflon (Polytetrafluoroethylene PTFE) pipe with a diameter of $2.4\,\mathrm{mm}$ which resulted with a wall thickness of $0.3\,\mathrm{mm}$. Vacuum assisted resin infusion without the diamond powder was performed (at the Institute of Composite Materials (IVW), Kaiserslautern). The braid was then cured in an autoclave at a static pressure of $24\,\mathrm{bar}$ close to 9 hours. An Omega was produced (at IVW, Kaiserslautern) with the prepreg carbon fibre with a lay up of [0/90/0] and was also cured in an autoclave. The stave parts (milled Iso-Graphite, the Pipe and an Omega) were then glued together with the epoxy-diamond powder glue. Upon curing, the stave final milling process was carried out with the aluminium vacuum tool where the excess remaining of the Iso-Graphite was milled in order to have a thickness of $0.5\,\mathrm{mm}$ (Figure 92). Finally, the fittings were connected to both the ends of the pipes in order perform the thermal measurements.

The second prototype of the Iso-Graphite stave was developed with diamond powder filled carbon fibre pipe. The diamond powder equivalent to a content of $13\,\%$ by volume fraction within the matrix ($\approx 6\,\%$ by volume fraction within the composite) was mixed in to the epoxy resin.

Initial milling of the Iso-Graphite   Production of the carbon fibre pipe   Production of Omega

Fittings for the thermal measurement

Iso-Graphite stave prototype after the final milling process

Stave final milling process with the aluminium vacuum tool
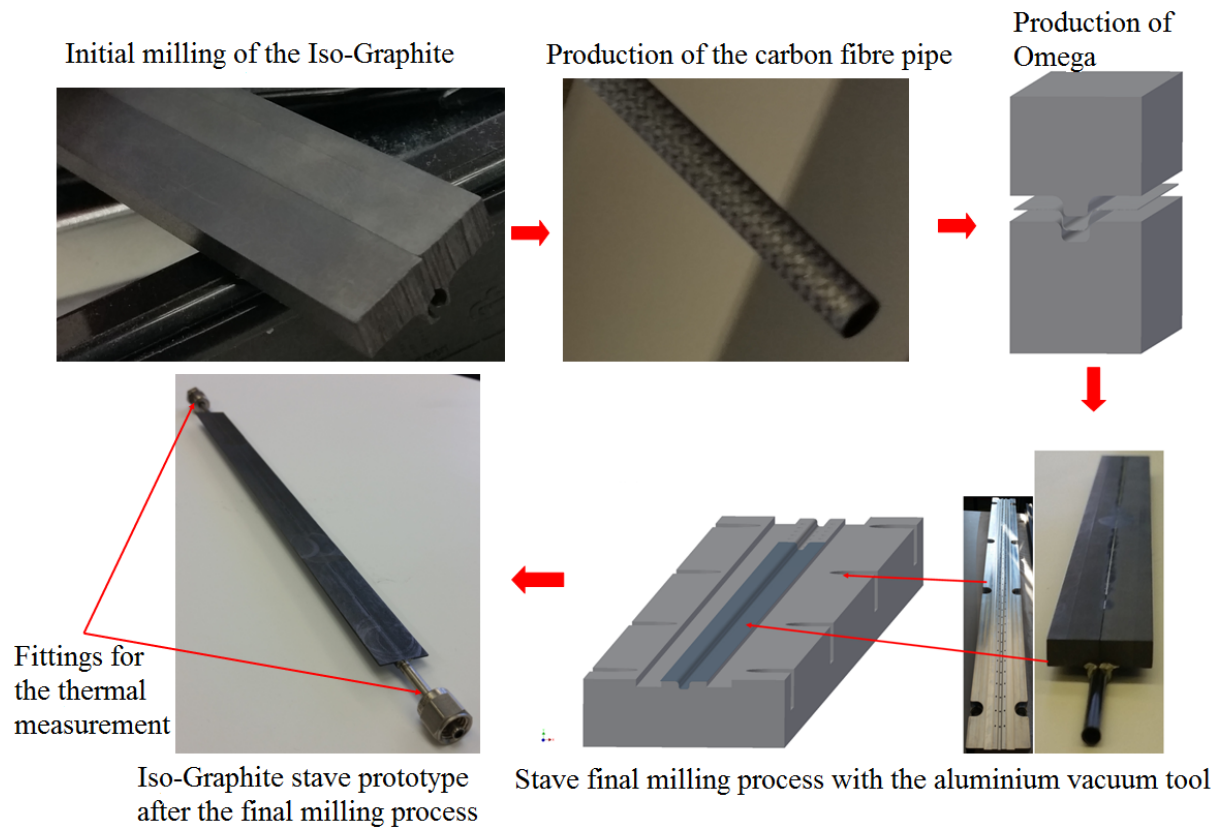
FIGURE 92: Iso-Graphite Vertical Split stave prototype production process

Vacuum assisted resin infusion technique (Figure 93) was then carried out, after which the carbon fibre pipe laminate was cured in an autoclave (at same pressure as explained before). After the curing process, the excess epoxy-diamond powder resin was scrapped off and the teflon pipe within the braid was also pulled out. The stave was then assembled and milled (Figure 93).

Vacuum assisted resin infusion

Epoxy diamond powder glue (excess)

Diamond powder filled carbon fibre pipe

Iso-Graphite stave prototype with the diamond powder pipe (after assembly)

FIGURE 93: Production process and the assembly of the Iso-Graphite stave prototype with diamond powder filled carbon fibre pipe

Researchers at Nikhef (The National Institute for Subatomic Physics, Amsterdam) have reported that the epoxy resin does not function well with the liquid CO_2. This is related to a problem of chemical compability. The researchers have also observed the problem of matrix cracking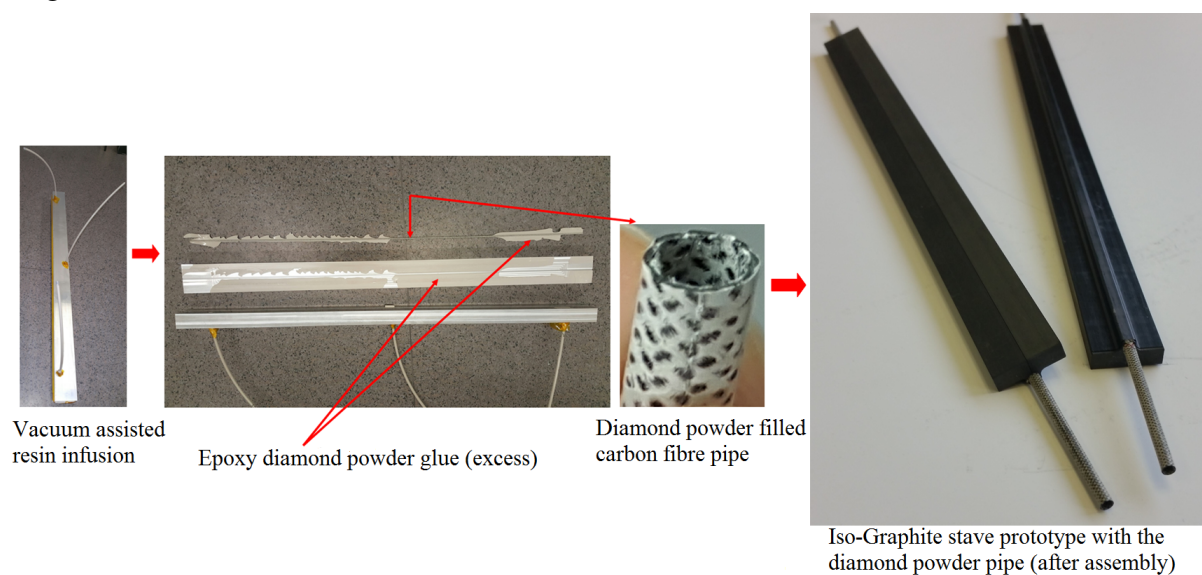 in the carbon fibre pipe while testing for pressure and leak rate with liquid CO_2 inside the pipe. Even though further experiments were not performed and this problem is not fully understood, in order to overcome the problem of the matrix cracking and the high viscosity of the epoxy resin (filled with DP), another pipe was developed with the cyanate ester resin filled the diamond powder (Figure 94).

When compared to the epoxy resin, the cyanate ester resin has several advantages like,

1. high Glass Transition Temperature (T_g), easy pre-cure at moderate temperature ($125 - 135\,°C$)[¶].

2. a low viscosity at the room temperature before curing [86].

3. low moisture absorption, high thermal stability [87].

4. radiation resistant [87], tough/resistant to microcracking caused by thermal cycling [87].

The standard modulus T300 braid was used and the same content ($13\,\%$ by volume fraction within the matrix) of the diamond powder was mixed in the cyanate ester resin (after it was pre-cured) and the vacuum assisted resin infusion was performed after which it was cured in an autoclave.

FIGURE 94: Development of the carbon fibre pipe filled with diamond powder-cyanate ester resin

The pipes (CF-epoxy, CF-epoxy filled with DP, CF-cyanate ester filled with DP) were tested for the pressure tightness at $150\,\mathrm{bar}$. This test was performed to qualify the pipe against the effect of the pressure and test was successful as all the pipes were able to withstand the pressure of $150\,\mathrm{bar}$. The second test was conducted to measure the leak tightness of the pipe with the helium and the pipes showed a leak rate $< 1\mathrm{E}{-}7\,\mathrm{atm\,cm^3\,s^{-1}}$

[¶]Cyanate ester matrix, http://www.saati.com/images/composites/prepregs/ce662.pdf

5.6.2   Stiffener Stave

Development of the tools for the prototype

The designs for producing the aluminium tools for the stiffener stave prototype were developed as shown in Figure 95. The carbon fibre braid would be placed in the bottom tool after which the high modulus carbon fibres would be placed between the pipe and the same process would be carried out on the other side after the the tool would be sealed to undergo vacuum assisted resin infusion (with the diamond powder filled resin) along with the curing in an autoclave. The fittings (Figure 96) for the stave prototype was developed with CF-PEEK material which would be like an end block through the flow of the liquid CO_2 inside the pipe could be controlled.

Vacuum assisted resin infusion
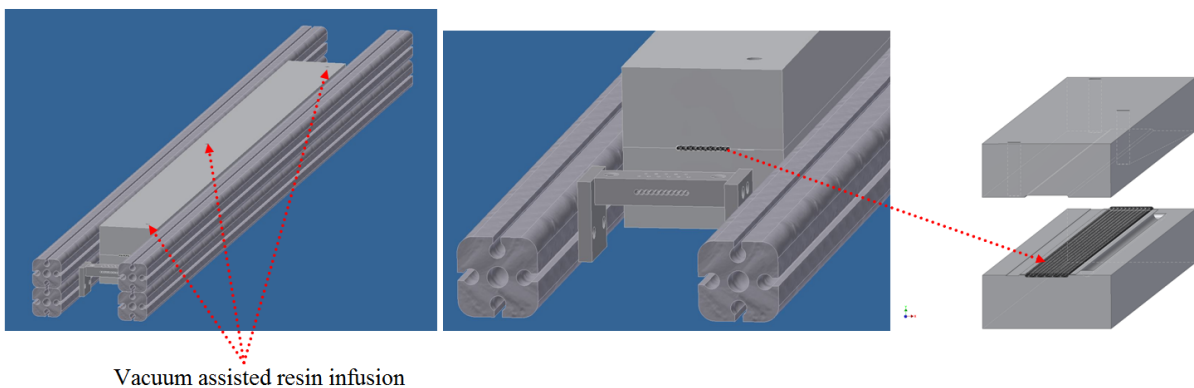
FIGURE 95: Development of the design for an aluminium tool for the vacuum
assisted resin infusion
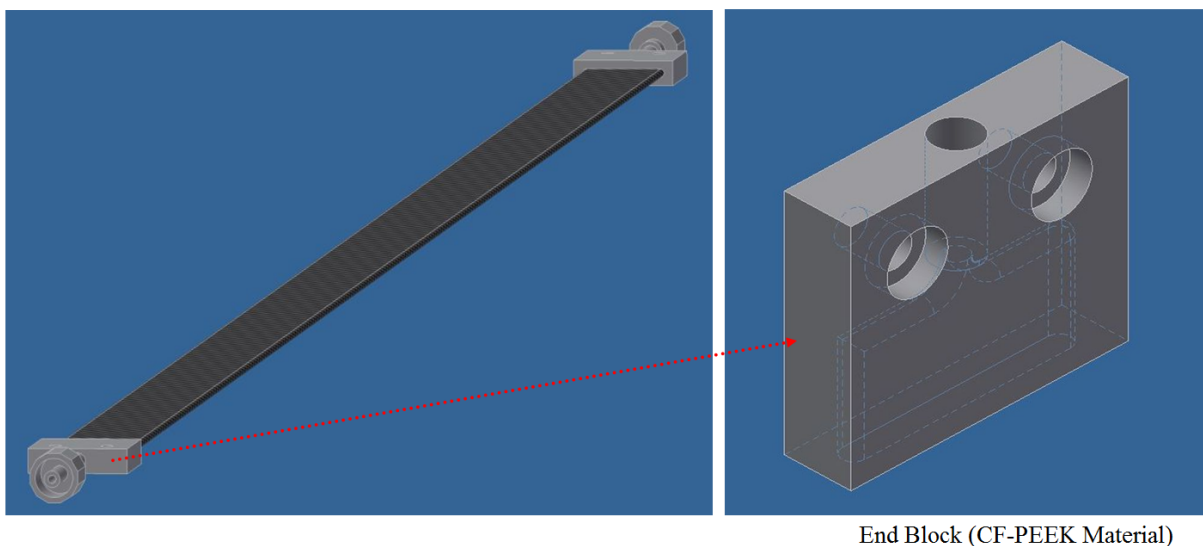

End Block (CF-PEEK Material)

FIGURE 96: Development of the design for the fittings for the prototype with
CF-PEEK material

6   Development of the Double Iso-Graphite Stave for the Innermost Detector Layers

6.1 Changes in the specification

The requirement for the conductive thermal figure of merit (TFM) was updated for each layer based on the types of sensor (Table 33). It was decided, that staves of the innermost detector layers could be mounted with 3D sensors as they dissipate less power when compared to that of planar sensors [84]. The staves of the outermost layers could be mounted with planar sensors (quad modules of about $40{\times}40$ mm^2).

Detector Layers	Conductive Thermal Figure of Merit ($^\circ$C cm^2 W^{-1})
Innermost Layer L0	11.22 (With 3D Sensors)
Innermost Layer L1	16.08 (With 3D Sensors)
Outermost Layer L2	11.91 (With Planar Sensors)
Outermost Layer L3	14.92 (With Planar Sensors)
Outermost Layer L4	18.83 (With Planar Sensors)

TABLE 33: Updated thermal figure of merit requirement for the innermost and outermost detector layers [84]

As specified before, the development of staves in the innermost detector layers L0 and L1 is the main focus of this thesis. By August 2015, the specification for the length of the inner layer L0 stave was modified from 750 mm to 1500 mm. Since the stave has to meet the requirements (listed in Table 1) for an operation at the HL-LHC, a change in the stave length would severely reduce the stiffness. The natural frequencies would be reduced and the deformations due to the structural and thermomechanical loading would increase. A series of design modifications were carried out in order to provide a working solution that would fulfil the overall requirements.

6.2 Initial Trial

The initial trial for the Iso-Graphite Vertical Split was performed by modifying the length (L) of the stave to 1500 mm. The design (Figure 97) was not modified. Finite element modelling for predicting the feformation by the gravity loading was carried out.
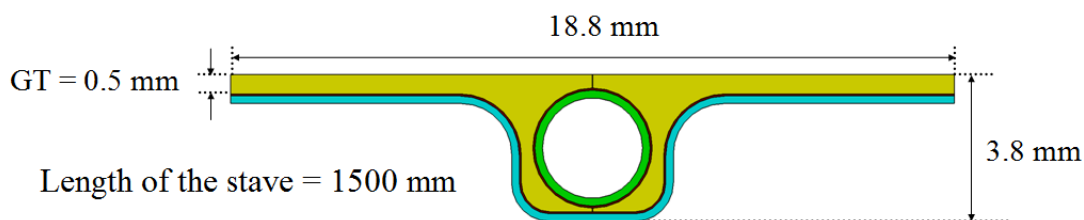

FIGURE 97: Iso-Graphite Verical Split stave with a length of 1500 mm

The boundary condition of the model was kept the same as shown in Figure 10, where both ends of the stave was fully constrained and an additional middle support allowed the stave to

slide in the longitudinal direction. Normally in mechanics, when a distributed load is applied to a structure, the deformation increases by a factor L^4. As expected, by modifying the length of the stave to $1500\,\text{mm}$, the deformation by gravity (Figure 98) increased to $366\,\mu\text{m}$, which is close to a factor L^4 when compared to the stave with a length of $750\,\text{mm}$.
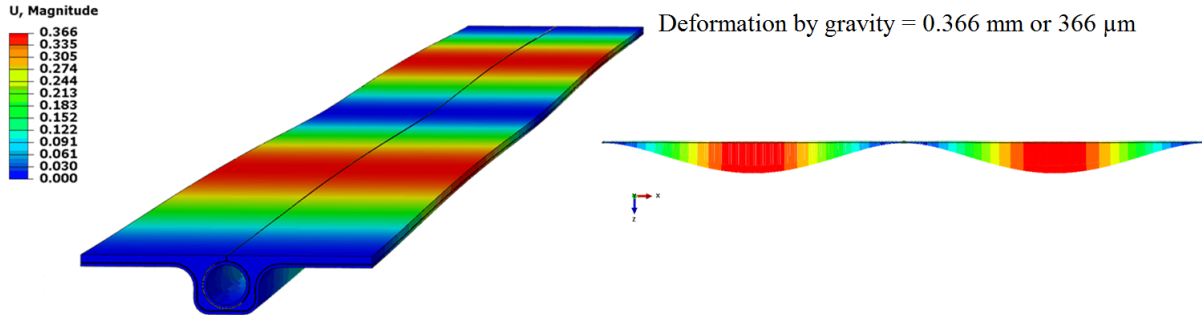
FIGURE 98: Increase in the deformation due the gravity loading with the change in the length

To get an optimal solution for the stave deformation within the specification limit, further trials were carried out by varying the number of supports and it was found that, by constraining the stave with five supports (Figure 99), the deformation by gravity reduced to $23\,\mu\text{m}$ (Figure 100).
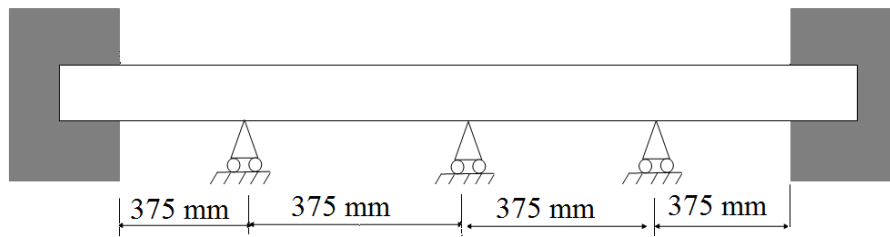
FIGURE 99: Boundary condition with two fixed constraints and three sliding constraints
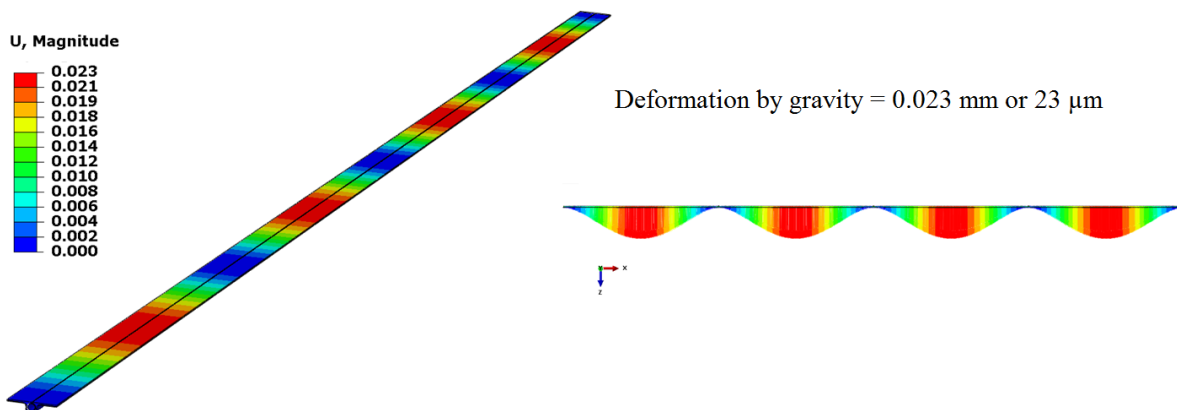
FIGURE 100: Reduction in the deformation due the gravity loading with five supports

A solution of five supports (fixations) as shown in Figure 99 provides a solution to reduce the deformation which is within the requirment. However, the five supports increases the material

budget with the increase in the total number of radiation length (X/X_0). Additional rings must be manufactured in order to provide the support which increases the complexity and the production cost. In order to increase the stiffness of the stave with a minimum increase in the material budget, different solutions are proposed in the next sections.

6.3   Supported Iso-Graphite Stave

By considering the size of the modules and the constraints as detailed in section 2.6, the inner layer L1 stave was developed with a width of $40\,\mathrm{mm}$ (Figure 101). Two cooling pipes were considered, as sufficient cooling would be required over the large surface to reduce the maximum temperature in order to achieve an optimal TFM. The design was developed in such a way that it could be manufactured as three separate parts and then could be glued together with the pipe and the omega. Heat transfer FEM (Figure 102) was performed (with the same boundary condition as detailed in Figure 7) and the maximum temperature was $6.4\,^{\circ}\mathrm{C}$ with a thermal figure of merit of $9.1\,^{\circ}\mathrm{C}\,\mathrm{cm}^2\,\mathrm{W}^{-1}$.
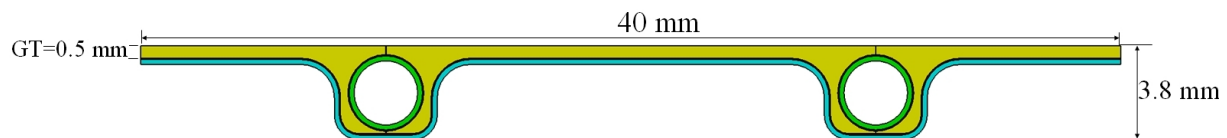
FIGURE 101: Development of the stave design for the inner detector layer L1 with two cooling pipes
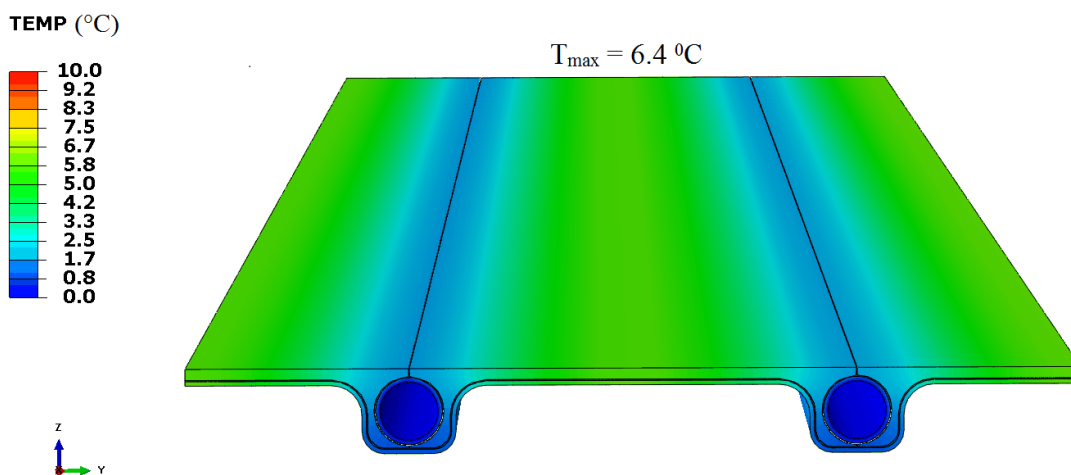
FIGURE 102: Heat Transfer FEM showing the maximum temperature on the surface of the graphite

The first thoughts for developing a new design was based on the radial positions of the detector layers L0 and L1 (Table 2) from the interaction point. The design was developed by connecting the layer L1 stave with the layer L0 stave through a composite structure of $0.3\,\mathrm{mm}$ thickness which could act as a stiffener (Figure 103). Since the composite structure was developed with an angular design, it was assumed that the structure could be produced with the standard modulus T300 fabric with an orientation of $\pm45^{\circ}$.
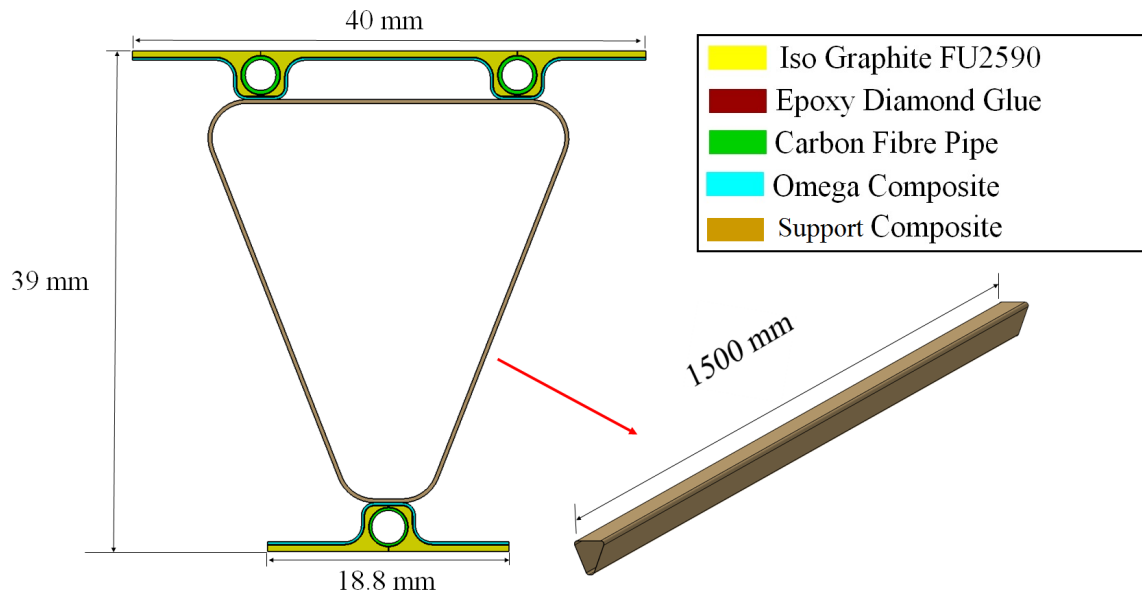
FIGURE 103: Representation of the Supported Iso-Graphite stave

Finite element modelling was performed for predicting the natural frequencies and the deformations by gravity loading, pressure and by thermal cool down. The boundary conditions were imposed by fully constraining the ends of the stave and the support composite. The finite element results showed that the stiffness of the stave was much improved as the deformations by the thermal cool down and gravity was only $51\,\mu\text{m}$ and $30\,\mu\text{m}$ respectively. The FEM result also showed, that the mode 1 frequency was $67\,\text{Hz}$. By connecting the two inner detector layer staves with the support composite improved the overall stiffness of the stave. The material budget of the stave is predicted based on the toal number of radiation length (X/X_0). The radiation length for every component of the stave (L0 and L1) was calculated based on their thickness. The X/X_0 of the stave for the two innermost layers were averaged along the width of the stave. The contribution of the support composite for both the layers were halved. The X/X_0 of the stave components that are calculated along the width are shown in Table 34, where the X/X_0 of the stave including the support composite is $0.52\,\%$ per layer. This is beyond the specification of $0.5\,\%$.

Stave parts	X/X_0 (%)
Iso-Graphite	0.22
CF pipe filled with diamond powder	0.076
Glue filled with diamond powder	0.02
Omega	0.082
Support composite	0.125
Total (per layer)	0.52

TABLE 34: Contribution of individual parts for the X/X_0 of the stave

Another problem of this design was, there was no overlap between the inner layer L0 staves. As already specified, a minimum of five pixel overlap equating to $0.25\,\text{mm}$ is required. Another

problem was that the overlapping inner layer L1 graphite are very close to the support composite. Further design modifications would be necessary to come over the overlap problem and these are reported in the next section

6.4 Double Iso-Graphite Stave

6.4.1 Design 1 and 2

The Double Iso-Graphite stave (design 1 and 2) were developed with a circular shape of the graphite with a thickness of $0.5\,\mathrm{mm}$ instead of the rectangular shape in order to avoid the manufacturing difficulties that were faced during the production of the prototypes. The two designs as shown in Figure 104 differ only in the diameter of the edge (marked in red in Figure 104), which connects the wings of the graphite.
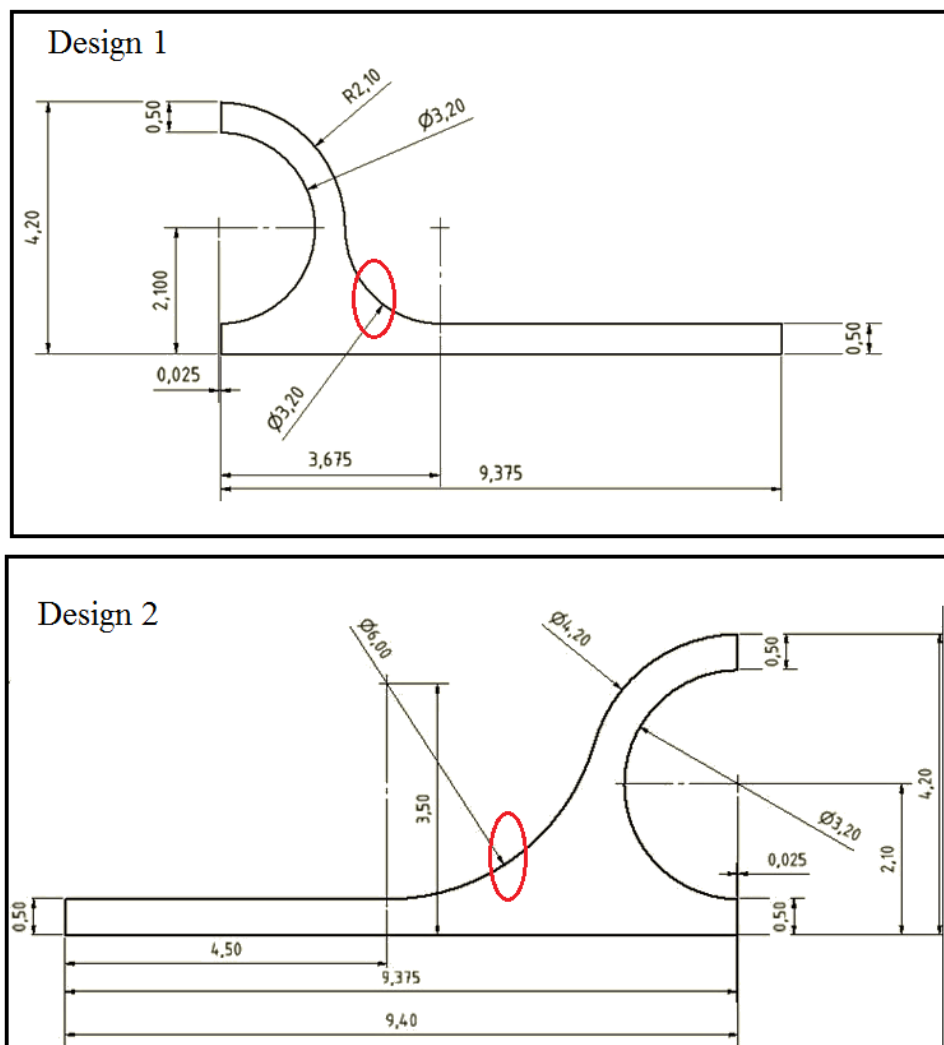

FIGURE 104: Design modification in the shape of the graphite

In both designs, two L0 graphite was glued to make a single L1 graphite with a width of $37.65\,\mathrm{mm}$ (Figure 105). In this way, the manufacturing complexities for producing different

tools for the layer L1 graphite could be drastically reduced. The total height of the stave was reduced to $38\,\mathrm{mm}$ (Figure 105). The pixel modules (electronics) with a thickness of $0.5\,\mathrm{mm}$ would be glued at the top and the bottom of the L0 and the L1 layer staves to make a total height of $39\,\mathrm{mm}$. These two designs were developed without an Omega in order to reduce the material budget.
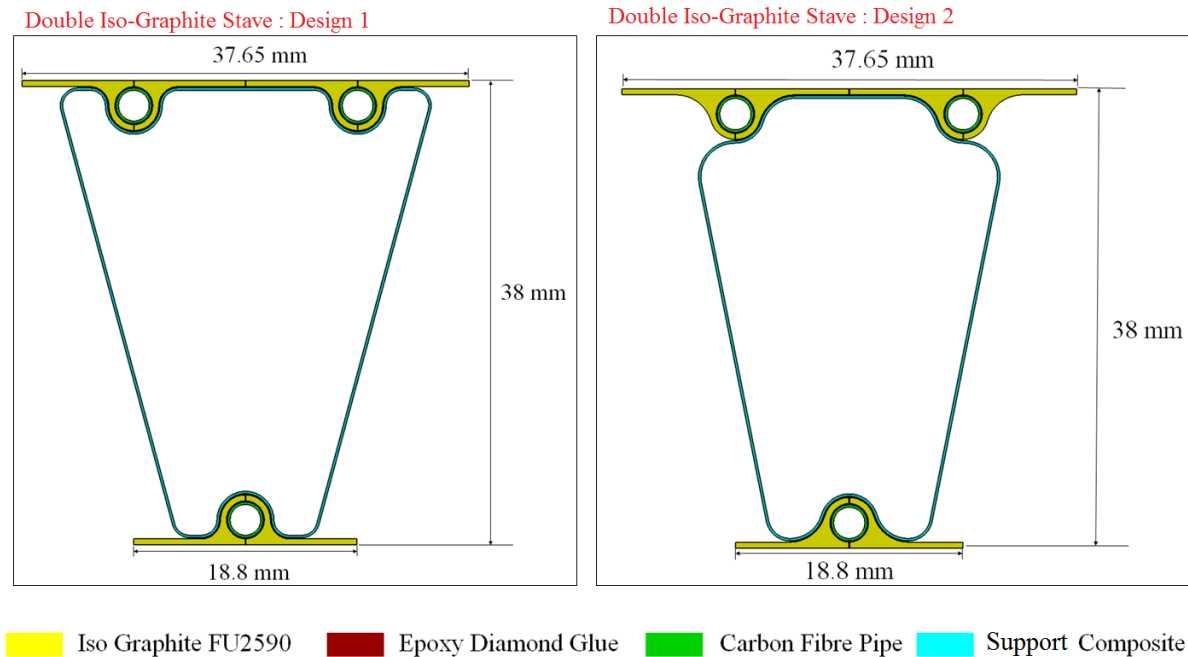
FIGURE 105: Representation of the Double Iso-Graphite stave designs 1 and 2 with the modification in the shape of the graphite and the support composite

The thickness of the support composite was reduced to $0.2\,\mathrm{mm}$ and it was directly glued to the graphite. In the Double Iso-Graphite stave design 1, the support composite was developed with a wider width (touching the wings of the graphite) (Figure 105). The FEM results (Table 35) showed, that the mode 1 natural frequency and the deformations by gravity and thermal cool down were within the specification limit. However, there was no overlap between the inner layer L0 staves when they were arranged in a layout of 14 staves with a tilt angle of $-14°$ (Figure 106). Reducing the tilt angle or increasing the number of staves would make a direct contact of the graphite material with the neighbouring support composite structure.

The problem with the overlap was solved with the Double Iso-Graphite stave design 2 (Figure 107), where the width of the support composite was reduced and the shape was designed without touching the wings of the graphite. An overlap distance of $0.35\,\mathrm{mm}$ was observed from the layout (Figure 107). One of the main drawback of this design was, that the mode 1 natural frequency was only $49.6\,\mathrm{Hz}$ (Table 35). The reason for the reduction in the stiffness towards the eigenvalue problem would be due to the lack of support towards the wings of the graphite. The fragile graphite requires a stable support in order to increase the stiffness of the stave.
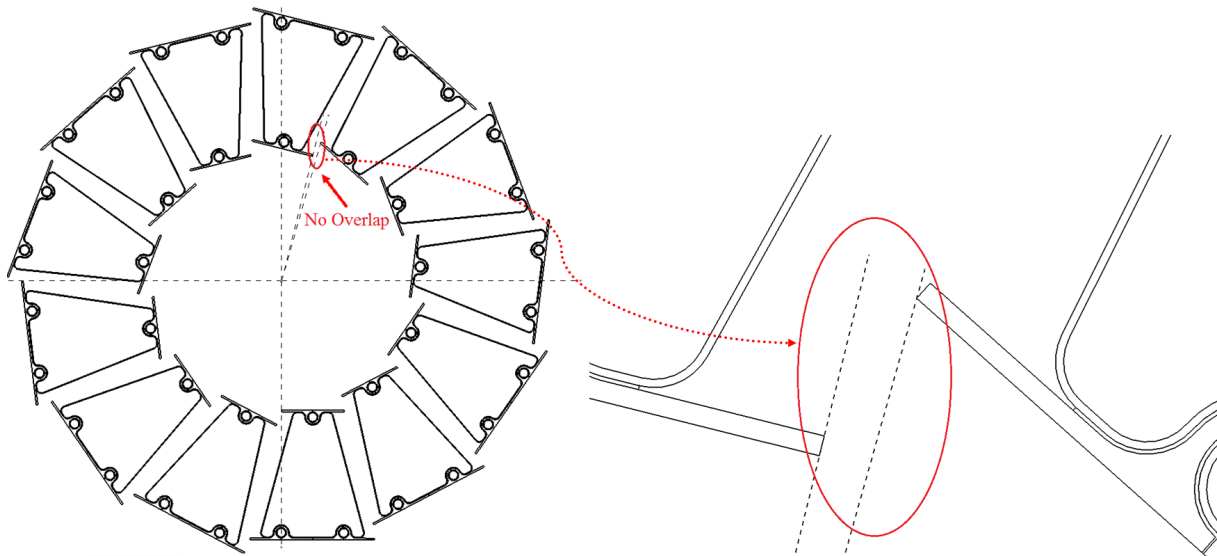
FIGURE 106: Layout of staves showing no overlap in the layer L0 staves
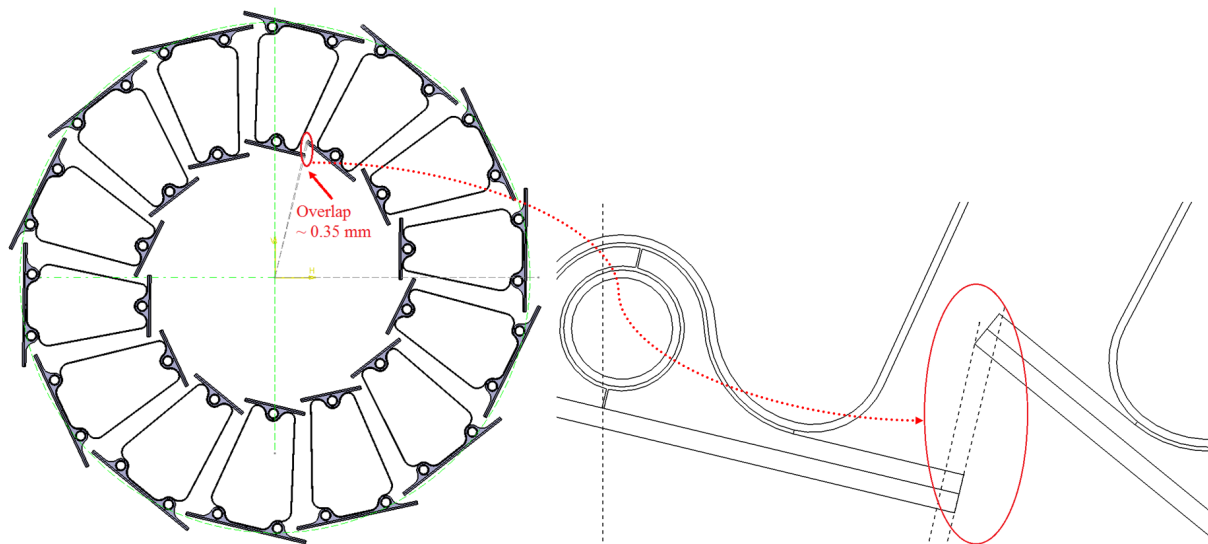
FIGURE 107: Layout of staves showing an improvement in the overlap distance

6.4.2   Design 3 and 4

Based on the requirement to improve the natural frequency without compromising the improvements in the thermomechanical FEM results and the overlap distance as reported in the previous design, the Double Iso-Graphite stave designs 3 and 4 were developed. The dimensions of the graphite as shown in the design 2 (Figure 104) was applied. The support of the composite (Figure 108) was developed with a non-symmetrical shape. One end of the support composite was designed with a wider width so that it could be glued directly to the wings of the graphite. The wider width with a smoother edge angle was developed considering the production techniques as the support composite has to be removed from the tool after curing in an autoclave. The other (left) end of the support composite's width was reduced without having any contact to the

wings of the graphite (Figure 108) so that the overlapping graphite would not have any contact
with the neighbouring support composite structure.
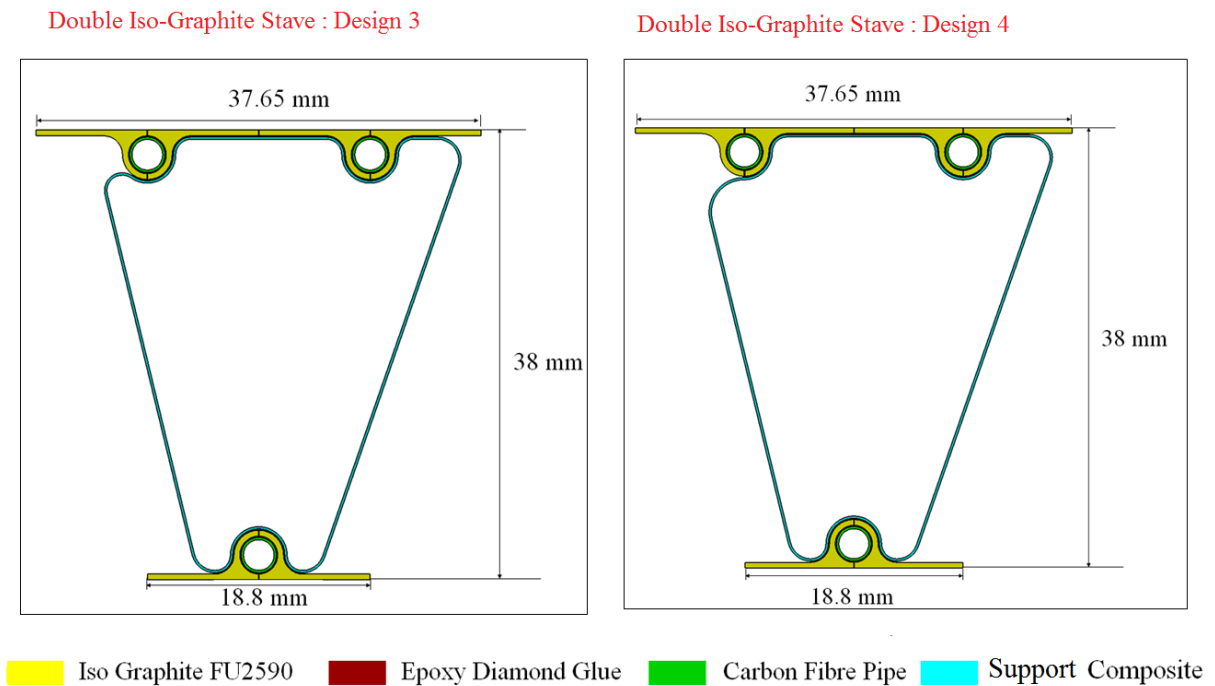
FIGURE 108: Representation of the Double Iso-Graphite stave (design 3 and 4)
with a non-symmetric shape of the support composite

The radius of the left end of the support composite was modified in the design 4 (Figure 108,
109) in order to completely mitigate the problem of contact with the overlapping graphite. The
layout (Figure 109) of 14 stave's (design 4) were arranged with the radial positions of $39\,\mathrm{mm}$(L0
Radius) and $78\,\mathrm{mm}$ (L1 Radius) respectively.
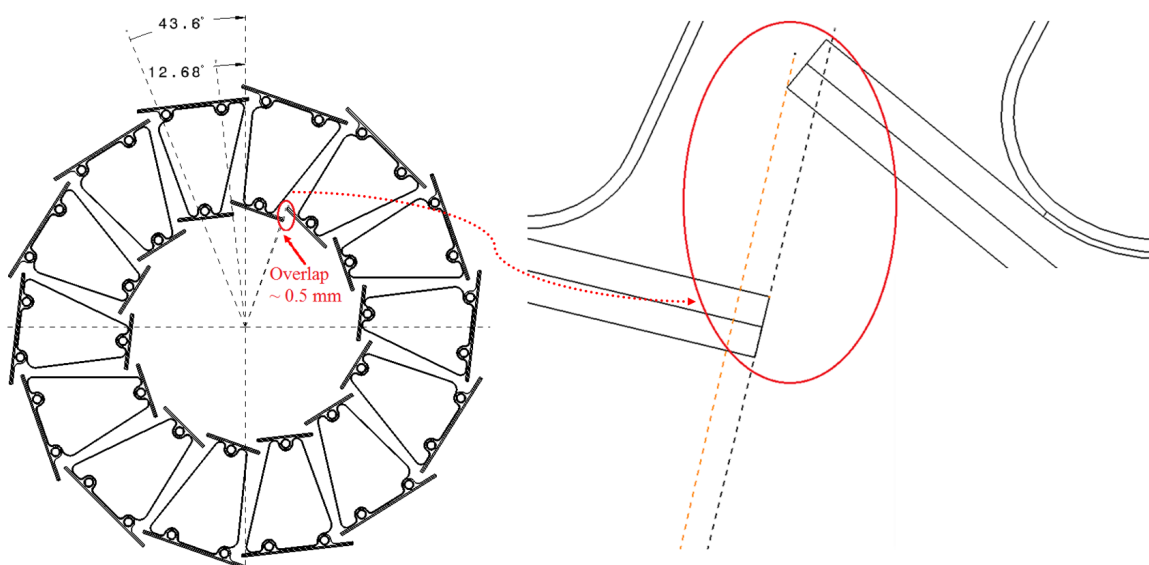
FIGURE 109: Layout of 14 staves with a tilt angle $-13.5°$ and an overlap distance
of $0.5\,\mathrm{mm}$ for the Double Iso-Graphite stave design 4

The Lorentz angle (tilt angle) was modified from $-14°$ to $-13.5°$ due to which the overlap distance increased to $0.5\,\mathrm{mm}$. As already specified, an adequate overlap distance would be required to compensate for the Lorentz angle (drift angle) in the magnetic field of the ATLAS detector. Heat transfer FEM results for the staves of both layers showed, that the maximum temperature (on the surface of the graphite) was only $5.6\,°\mathrm{C}$ with a thermal figure of merit of $8\,°\mathrm{C}\,\mathrm{cm}^2\,\mathrm{W}^{-1}$ (Table 35, Figure 110). This thermal figure of merit is well within the requirement as shown in Table 33. Since the staves on both the layers experiences the same amount of the power over the surface with an equal amount of cooling results both the staves to have the same maximum temperature. This design showed a lower thermal figure of merit when compared to the design as shown in Figure 102, is due to the difference in the width of the stave.
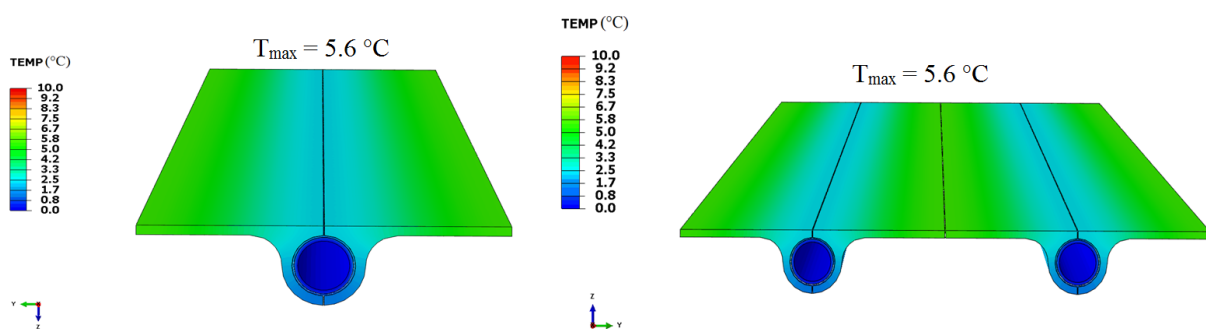
FIGURE 110: Heat Transfer FEM showing the maximum temperature of $5.6\,°\mathrm{C}$
for staves in both layers

In previous designs, FEM boundary conditions were imposed by fully constraining the ends of the stave and the support composite. From the production perspective, it was learnt that it would be difficult to clamp the graphite as it is quite brittle to handle. Considering this difficulty, the boundary conditions for predicting the natural frequency, deformation by gravity and the thermal cool down were applied by fully constraining the ends of the support composite only (Figure 111).
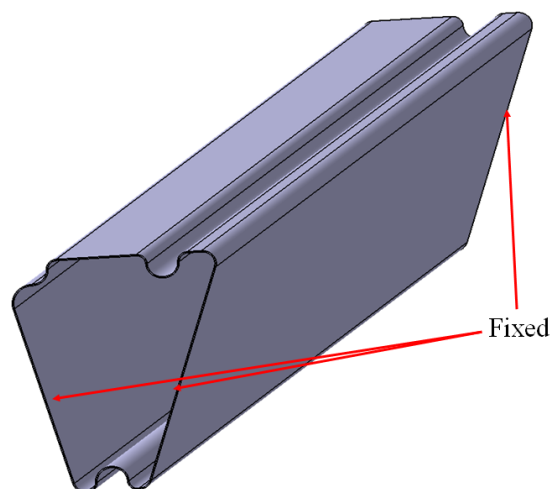
FIGURE 111: Representation of the boundary condition by fixing the ends of the
support composite only

With the improved design of the support composite, the mode 1 natural frequency of the stave increased to $55.66\,\mathrm{Hz}$ and $55.15\,\mathrm{Hz}$ for the designs 3 and 4 (Table 35). The deformation by the thermal cool down of the stave for the designs 3 and 4 was $52\,\mu\mathrm{m}$ and $54\,\mu\mathrm{m}$. As the stave was fully constrained only at the ends of the support composite, the maximum deflection of the stave under lateral loads remained at the middle of the stave as the bending moment varies along the length of the stave (Figure 112). The deformations by the pressure and gravity loadings were almost the same for both designs (Table 35).

The rate of particles crossing the inner detector layers is expected to be higher at the HL-LHC. The exposure to radiation is also expected to be higher for the staves in the innermost layers. This is the reason why the stave has to be developed within a minimal material budget and also must be stiff and stable in order to maximise the physics performance.
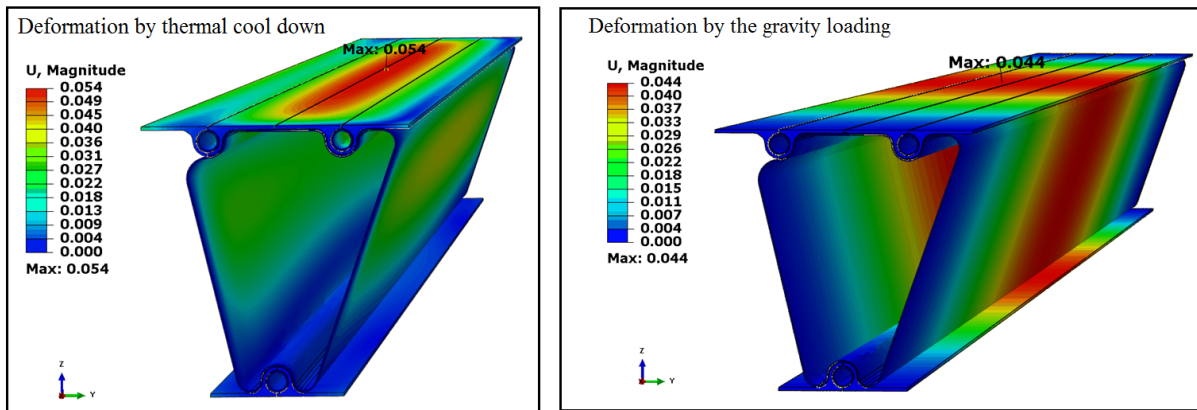
FIGURE 112: FEM results for the deformations by thermal cool down and gravity loading

FEM Results

Double Iso-Graphite stave	Maximum Temperature	Thermal Figure of Merit	Thermal Cool Down	Pressure Deformation	Gravity Sag	Mode 1 Frequency
	(°C)	($\mathrm{°C\,cm^2\,W^{-1}}$)	(µm)	(µm)	(µm)	(Hz)
Design 1	5.6	8	69	8	39	65.44
Design 2	5.6	8	30	10	45	49.6
Design 3	5.6	8	52	12	44	55.66
Design 4	5.6	8	54	12	44	55.15
Requirement	< 10.5	< 15	< 100	< 100	< 100	> 50

TABLE 35: FEM results of the Double Iso-Graphite stave designs 1,2, 3 and 4

6.4.3 Comparison of the X/X_0 between the Double Iso-Graphite (design 4) and IBL Stave

A comparison between the X/X_0 between the IBL bare stave and the Double Iso-Graphite stave design 4 are shown in the Table 36. The IBL stave has the total radiation length of 0.62% while the Double Iso-Graphite stave design 4 has the total number of radiation length of 0.4% (per layer). This leads to an improvement by a factor 1.55 and this improvement would be quite important as the stave would be exposed to high radiation environment when the detector is operational under the HL-LHC. One of the main objectives of this thesis was to develop an optimal design with an enhanced performance along with a minimum material budget and by considering the results of the total radiation length, FEM and the layout along with the overlap distance enables to suggest that the Double Iso-Graphite stave design 4 is a favourable design for the innermost barrel layer.

X/X_0	Double Iso-Graphite Stave (design 4)	IBL (bare) Stave	X/X_0
0.22%	Graphite	Foam	0.0721%
0.076%	CF pipe filled with DP (6 vol%)	Titanium pipe	0.0821%
0.02%	Glue filled with DP	pipe glue layer	0.0335%
0.0825%	Support Composite	Omega	0.068%
		Omega glue layer	0.1103%
		Face Plate	0.0641%
		Face Plate glue layer	0.1040%
		EOS	0.0714%
		EOS glue layer	0.0130%
		Central PEEK support	0.0021%
0.4%	Total (per layer)	Total	0.62%

TABLE 36: Comparison of X/X_0 between the IBL stave and the Double Iso-Graphite stave design 4

6.4.4 Development of the cut-out's on the support composite

The development of cuts-out's on the support composite would help to reduce the X/X_0 by reducting the material. The initial cut-out's as shown in Figure 113 was developed with five chambers along with the shape of an equilateral triangle as it would help to connect the cables from the sensor electronics to the other end of the detector. As the support composite would be developed with an off-axis ($\pm 45°$) fabric, the shape of this cut-out would prevent the maximum damage to the fibres in the fibre direction. The mass of the support composite without cut-out's was measured (CATIA® V5) to be $53\,\mathrm{g}$ while after initial cut-out's it was further reduced to $48\,\mathrm{g}$. The eigenvalue analysis was carried out and the mode 1 natural frequency was predicted to be $53.5\,\mathrm{Hz}$ (Figure 113). The mode 1 natural frequency before the initial cut-out was $55.15\,\mathrm{Hz}$ which leads to a reduction in the stiffness of about $3\,\%$.

Mass of the support composite $= 53$ grams

Mass of the support composite after cut-outs $= 48$ grams

Mode 1 natural frequency $= 53.5$ Hz

Requirement : > 50 Hz
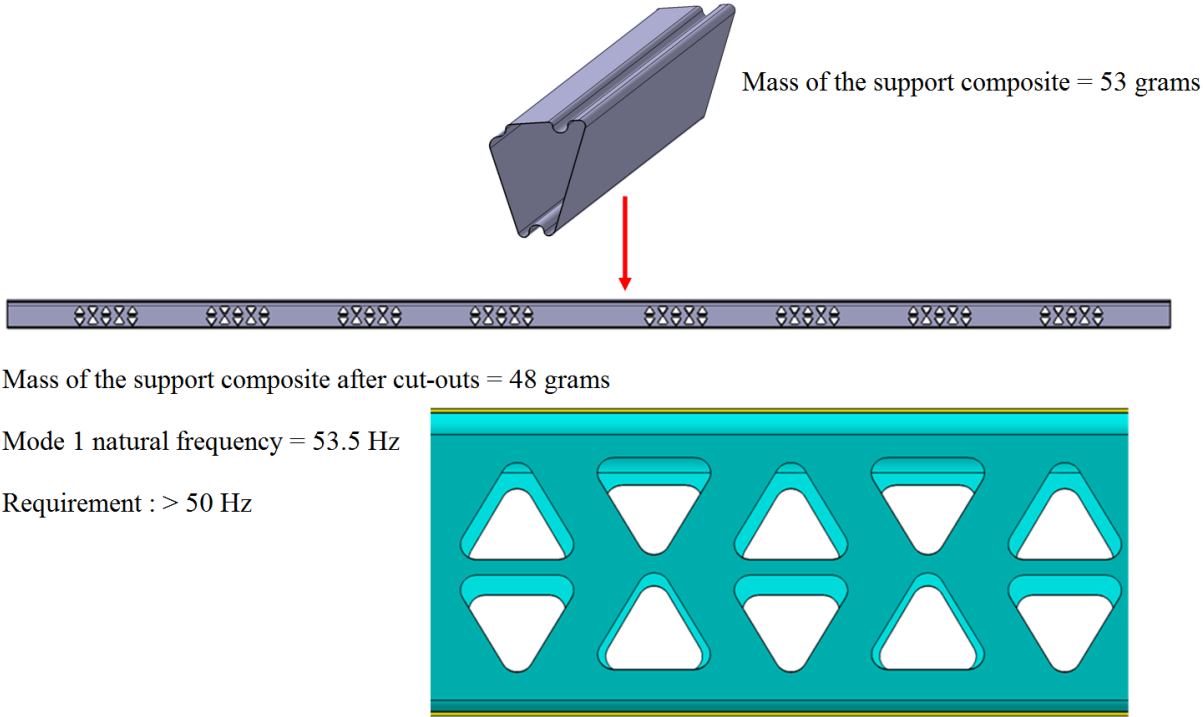
FIGURE 113: Development of the initial cut-out's on the support composite showing the reduction of the mass with an acceptable reduction in the stiffness

To understand the stability in relation to cut-outs, the number of cuts-out's were increased to seven chambers as shown in Figure 114 and the mass of the support composite reduced to $46\,\mathrm{g}$ while the mode 1 natural frequency reduced to $48\,\mathrm{Hz}$ which is below the specification limit along with the reduction in the stiffness of about $13\,\%$.

In near future, an optimisation technique would be required to be carried out by varying the number and shape of chambers in order to get an optimal shape and limit for the number of cut-out's.

Mass of the support composite = 53 grams

Mass of the support composite after cut-outs = 46 grams

Mode 1 natural frequency = 48 Hz
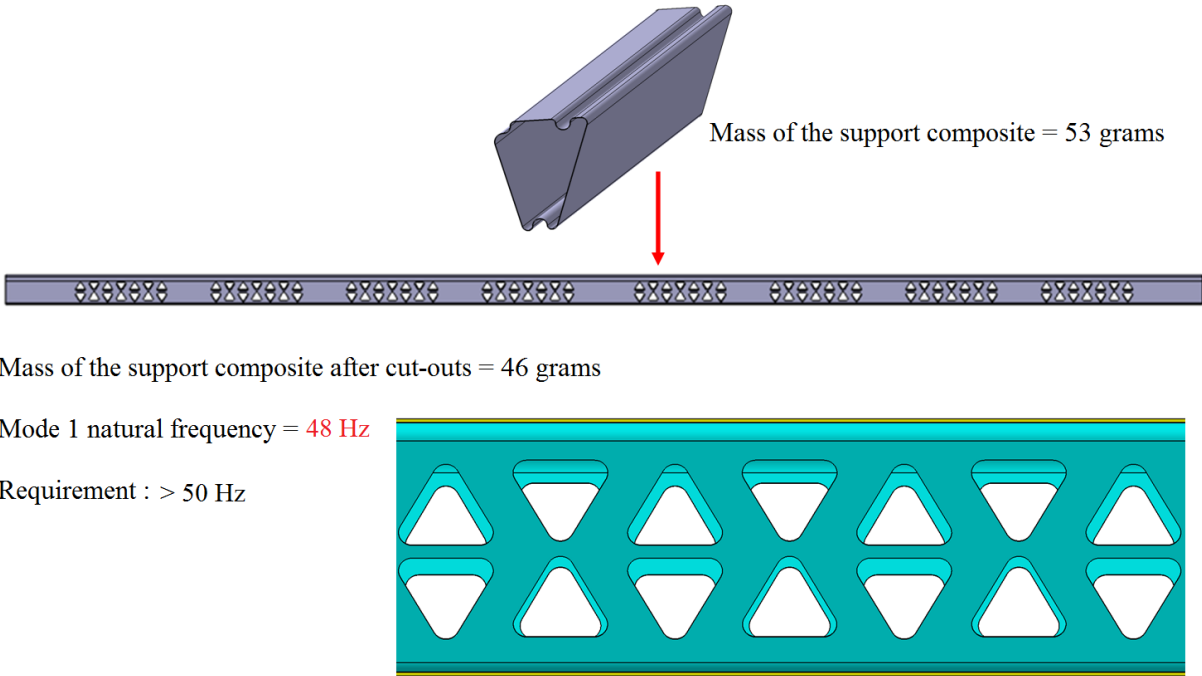
Requirement : > 50 Hz

FIGURE 114: An increment in the number of cut-out's on the support composite reduced the mass and the stiffness of the stave below the requirement

7 Conclusions

The present research demonstrated the development of the local support structures (stave) of the pixel detector for the upgrade (ITK) of the ATLAS experiment at CERN. This chapter presents the overall conclusions and contributions from the investigation.

7.1 Out of plane thermal conductivity ($K_\perp$)

In this investigation, the role of the diamond powder (DP) in enhancing the out of plane thermal conductivity of the standard modulus T300 and the high modulus YS90A woven composites were examined by FEM and thermal measurements. Finite Element Modelling (FEM) based on the micromechanics approach was carried out in order to generate the microstructures.

The results predicted by the FEM showed the lack of improvement in the out of plane thermal conductivity at lower diamond powder content as the distance between the inter-filler (diamond powder-diamond powder) and filler-fibre distance were larger at lower diamond powder content and the isolated diamond powder particles did not show any significant effects towards a thermal conductivity improvement and it also resulted in a lack of formation of conductive paths.

FEM investigations with the higher diamond powder contents showed the formation of the conductive path through the interaction between the fibre and the filler which improved the thermal transport. The results showed that the thermal conductivity of the composites depends significantly on the fibre and diamond powder filler volume fraction.

Experimental results from the thermal measurements found that the out of plane thermal conductivity ($K_\perp$) of the standard modulus composite increased by a factor of 2.3 with 14% volume fraction of diamond powder in the composite while the the out of plane thermal conductivity of the high modulus composite increased by a factor of 2.8 with 12% volume fraction of diamond powder in the composite. Good consistency between the measurements and the FEM results was observed.

7.2 The elastic and failure behaviour of diamond powder filled composites

Numerical homogenisation technique was applied to predict the elastic properties of diamond powder enhanced matrix. A micromechanical unit cell model was developed in order to predict the elastic properties of diamond powder filled woven fabric composites. Numerical investigations were performed in order to examine the role of diamond powder towards the on-axis tensile and flexure behaviour of the T300 and YS90A woven composites This was carried out through a progressive damage modelling technique. The influence of diamond powder towards the tensile strength, flexural strength and modulus of the T300 composite was quite minimal.

Static tensile and flexural testing was carried out on the high modulus YS90A composite coupons filled without and with 6% and 12% volume fractions of diamond powder in the composite.

Fabrication of the high modulus YS90A composite coupons through the matrix modification technique with the diamond powder increased the viscosity of the resin which led to a non-homogeneous dispersion of diamond powder in the composite. This led to a reduction in the elastic properties of the YS90A composite when subjected to an on-axis tensile testing.

Finite element modelling for the YS90A composite was carried out with OHT coupons in order to investigate the effect of stress concentrations in the composite when subjected to tensile loading. The reduction in the elastic modulus was observed with the OHT FEM results.

7.3   Development of new stave designs

The improved thermal and the mechanical properties of the diamond powder filled carbon fibre composites were applied to the cooling pipe through which three different designs of the local support structure namely "Fishbone stave", Iso-Graphite stave" and "Stiffener stave" were developed. The preferred designs were, the Iso-Graphite and the Stiffener Stave. The initial designs were developed with a length of $750\,\mathrm{mm}$.

7.3.1   Iso-Graphite Stave

The Iso-Graphite stave design showed the possibility to take away the maximum heat from the sensor electronics. A total of six designs were developed. Iso-Graphite Vertical Split proved to a realistic design in terms of the production. Parametric modifications were performed by increasing the thickness of the graphite from $0.2\,\mathrm{mm}$ - $0.5\,\mathrm{mm}$ in order to find an optimal FEM thermal and thermomechanical behaviour based on the thickness of the graphite. It was found that the design with the graphite thickness of $0.5\,\mathrm{mm}$ provided a robust solution with a minimum material budget, where the thermal figure of merit reduced to $7\,\mathrm{°C\,cm^2\,W^{-1}}$. The thermomechanical deformation results were within the specification limit and the X/X$_0$ of the stave was only $0.33\,\%$. It was observed that a reduction in the thermal figure of merit of the stave increased the X/X_0.

The prototypes of the Iso-Graphite stave were developed without and with diamond powder (6 vol%) in the carbon fibre pipe. Another pipe was developed with the cyanate ester resin. Three pipes were tested for a pressure up to $150\,\mathrm{bar}$ and all the pipes were able to withstand that pressure. The thermal measurements on stave prototypes should be carried out at CERN.

7.3.2   Stiffener Stave

A Stiffener stave was developed with an idea to use a single stiff and stable structure with an adequate amount of cooling in order to have a better thermal behaviour. A total of 7 designs were developed. Initial designs were developed with two or three pipes and the shapes were varied from ellipsoidal to spherical which improved the deformation due the pressure. It was then learnt that the high modulus YS90A fibres could not be be braided. Eleven Pipes Stiffener

stave was developed with an outer diameter of $1.8\,\mathrm{mm}$ and an inner diameter of $1.6\,\mathrm{mm}$. It was learnt from the heat transfer FEM that, the close contact between the fibres (diamond filled) in the pipe could improve the heat transfer and the maximum temperature (on the surface of the stave) was only $3.9\,^{\circ}\mathrm{C}$. An improvement in stiffness was observed from the thermomechanical FEM results. The highlights of this design, are the heat transfer behaviour and a reduced material budget. The total X/X_0 of the stave was only $0.164\,\%$ (excluding the CO_2 inside the pipe) and $0.46\,\%$ (including the CO_2 inside the pipe).

7.3.3 Double Iso-Graphite Stave

The design of the Iso-Graphite stave was modified by connecting the inner layer L0 stave with the layer L1 stave through a support composite. The Layer L1 stave was developed with two pipes in order to have sufficient cooling over a wider width. It was found that the Double Iso-Graphite (design 4) provided an optimal solution where, the support composite was developed with a non symmetric shape with a thickness of $0.2\,\mathrm{mm}$. FEM results showed that the structural, thermal thermomechanical behaviour of the stave was well within the requirement. The total X/X_0 was only $0.4\,\%$ (per layer), where as the IBL (bare) stave has a X/X_0 of $0.62\,\%$.

8 Outlook

The following are the suggestions for continuing the research:

1. Higher precision fabrication techniques to overcome the problem of a non-homogeneous dispersion of diamond powder in the composite must be explored and investigated.

2. Experimental testing must be carried out to examine the inter-facial shear strength and stiffness of the diamond powder filled woven composites.

3. Different constitutive laws considering through the thickness mechanical properties as well as strain rate effects in the diamond powder filled composite are required and need to be developed which could be implemented through an explicit rather than implicit FEA modeling scheme.

4. A prototype with a length of $1000\,\mathrm{mm}$ for the inner layer of the Iso-Graphite stave support structure must be produced. The Iso-Graphite stave design for the other barrel layers namely L3, L4 and L5 must be developed (along with any optimisation technique if it is required)

5. The stiffener stave with a length of $1500\,\mathrm{mm}$ for all the five layers along with the FEM must be developed. Necessary prototypes must also be produced

6. Thermal and the mechanical(3 Point Bending, Vibration) measurements must be performed on the prototypes in order to measure the thermal figure of merit, natural frequencies and the stiffness of the stave and also to validate the FEM models (any change in the boundary condition must be updated)

Bibliography

[1] R Morris. *The Edges of Science: Crossing the Boundary from Physics to Metaphysics*. New Jersey: Prentice Hall, 1990.

[2] A Das and T Ferbel. "Introduction to Nuclear and Particle Physics (2nd Edition)". In: Singapore: World Scientific Publishing Co. Pte. Ltd, 2003, pp. 1–395.

[3] G Bertone, D Hooper, and J Silk. "Particle Dark Matter: Evidence, Candidates and Constraints". In: *Physics Reports* 405 (2005), pp. 279–390.

[4] A Breskin, V Ruediger. *The CERN Large Hadron Collider : Accelerator and Experiments*. LHC Machine, Alice, and Atlas. CERN, 2009, pp. 1–405.

[5] ATLAS Collaboration. "Evidence for the spin-0 nature of the Higgs boson using ATLAS data". In: *Physics Letters B* 726 (2013), pp. 120–144.

[6] L3 Collaboration. "Standard model Higgs boson with the L3 experiment at LEP". In: *Physics Letters B* 517 (2001), pp. 319–331.

[7] ATLAS Collaboration. "The ATLAS Experiment at the CERN Large Hadron Collider". In: *Journal of Instrumentation* 3 S08003 (2008), p. 437.

[8] ATLAS Collaboration. "ATLAS Insertable B-Layer Technical Design Report". In: *CERN-LHCC-2010-013. ATLAS-TDR-19* (2010).

[9] A Miucci. "The ATLAS Insertable B-Layer project". In: *Journal of Instrumentation* 9 C02018 (2014), p. 2.

[10] ATLAS Collaboration. "The ATLAS Pixel Insertable B-Layer (IBL)". In: *Nuclear Instruments and Methods in Physics Research Section A: Accelerators, Spectrometers, Detectors and Associated Equipment* 650 (2010), pp. 45–49.

[11] E Vigolas. *Overlap Condition to determine the layers R/Phi parameters of the ATLAS Inner Tracker Upgrade Layout*. Internal Report. CERN.

[12] S Coelli, M Monti. *IBL STAVE THERMAL PERFORMANCE*. ATLAS Project Document No: ATU-SYS-EA-0007. INFN Milano, 2012.

[13] T Stefaan. "Experimental Techniques in Nuclear and Particle Physics". In: *Interactions of Particles in Matter*. 2009, pp. 23–53.

[14] M Gupta. *Calculation of radiation length in materials*. ATLAS Project Document No: PH-EP-Tech-Note-2010-013. CERN, 2010.

[15] D Giugni. *ITK Pixel Local Support Design Parameter*. ATLAS Project Document No: ATU-SYS-ES-0029. CERN, 2016.

[16] EP Scott and JV Beck. "Estimation of Thermal Properties in Epoxy Matrix/Carbon Fiber Composite Materials". In: *Journal of Composite Materials* 26 (1992), pp. 132–149.

[17] A Dixit, HS Mali. "Modelling techniques for predicting the mechanical properties of woven-fabric textile composites: A review". In: *Journal of Mechanics of Composite Materials* 49 (2013), pp. 1–20.

[18] S Eslam, K Usama, RT Mahmoud. "Improved Strength and Toughness of Carbon Woven Fabric Composites with Functionalized MWCNTs". In: *Materials* 7 (2014), pp. 4640–4657.

[19] H Ahmad, AD Crocombe, and PA Smith. "Physically based finite element strength prediction in notched woven laminates under quasi-static loading". In: *Plastics, Rubber and Composites* 42 (2012), pp. 93–100.

[20] M Sharon. "Graphene". In: *An introduction to the fundamentals and industrial applications*. New Jersey and Massachusetts: John Wiley & Sons, Inc. and Scrivener Publishing LLC, 2015, pp. 1–277.

[21] MFL De Volder, SH Tawfick, RH Baughman, AJ Hart. "Carbon nanotubes: Present and future commerical applications". In: *Science* 339 (2013), pp. 535–539.

[22] C Scoville, R Cole, J Hogg, O Farooque, and A Russell. *Carbon Nanotubes*. University of Washington, 2008.

[23] Gurit Holding AG. *Guide to Composites*. GTC-5-0113. Gurit, pp. 1–71.

[24] United States Department of Transportation, Federal Aviation Administration, Airman Testing Standards Branch. "Advanced Composite Materials (Chapter 7)". In: *The Aviation Maintenance Technician Handbook - Airframe (FAA-H-8083-31)*. 2012, pp. 1–58.

[25] H Xiaosong. "Fabrication and Properties of Carbon Fibers". In: *Materials* 2 (2009), pp. 2369–2403.

[26] A Yutaka. "Pitch based carbon fiber with low modulus and high heat conduction". In: *Nippon Graphite Fiber Corportation, Nippon Steel Technical Report Number 8* (2001), pp. 12–17.

[27] IC Lewis. "Chemistry of carbonization". In: *Carbon* 20 (2003), pp. 519–529.

[28] LS Singer. "Carbon fibres from mesophase pitch". In: *Fuel* 60 (1981), pp. 839–847.

[29] PK Mallick. *Fiber-Reinforced Composites-Materials, Manufacturing, and Design*. New York: Marcel Dekker Inc., 1993.

[30] J Hong, DW Park, and SE Shim. "A Review on Thermal Conductivity of Polymer Composites Using Carbon-Based Fillers : Carbon Nanotubes and Carbon Fibers". In: *Carbon Letters* 11 (2010), pp. 347–356.

[31] SH Song, KH Park, BH Kim, YW Choi, GH Jun, DJ Lee, BS Kong, KW Paik, and S Jeon. "Enhanced Thermal Conductivity of Epoxy-Graphene Composites by Using Non-Oxidized Graphene Flakes with Non-Covalent Functionalization". In: *Advanced Materials* 25 (2013), pp. 732–737.

[32] H Fusao, K Hiroyuki, and T Yoshitaka. "Synthesis of a polymer composite with networked α-alumina fiber and evaluation of its thermal conductivity". In: *Journal of the Ceramic Society of Japan* 119 (2011), pp. 601–604.

[33] Biercuk MJ, Llaguno MC, Radosavljevic M, Hyun JK, and Johnson AT. "Carbon Nanotube Composites for Thermal Management". In: *Applied Physics Letters* 80 (2002), pp. 2767–2769.

[34] SA Gordeye, FJ Macedo, JA Ferrerira, FWJ van Hattum, and CA Bernardo. "Transport Properties of Polymer-Vapor Grown Carbon Fiber Composites". In: *Physica B: Condensed Matter* 279 (2000), pp. 33–36.

[35] HO Pierson. *Hand book of Carbon, Graphite, Diamond and fullerenes Properties, Processing and Applications*. Noyes: William Andrew Publishing, 1993.

[36] S Yang, K Lozano, A Lomeli, HD Foltz, and R Jones. "Electromagnetic interference shielding effectiveness of carbon nanofiber/LCP composites". In: *Composites Part A: Applied Science and Manufacturing* 36 (2005), 691697.

[37] RD Patton, CU Pittman Jr, L Wang, and JR Hill. "Vapor grown carbon fiber composites with epoxy and poly(phenylene sulfide) matrices". In: *Composites Part A: Applied Science and Manufacturing* 30 (1999), pp. 1081–1091.

[38] Y Xing, W Cao, W Li, H Chen, M Wang, H Wei, D Hu, M Chen, and Q Li. "Carbon Nanotube/Cu Nanowires/Epoxy Composite Mats with Improved Thermal and Electrical Conductivity". In: *Journal of Nanoscience and Nanotechnology* 15 (2015), pp. 3265–3270.

[39] H Huang, CH Liu, Y Wu, and S Fan. "Aligned Carbon Nanotube Films for Thermal Management". In: *Advanced Materials* 17 (2005), pp. 1652–1656.

[40] JH Koo. *Polymer Nanocomposites: Processing, Characterization, and Applications*. New York: McGraw-Hill, 2006.

[41] KS Novoselov, AK Geim, SV Morozov, D Jiang, Y Zhang, SV Dubonos, IV Grigorieva, and AA Firsov. "Electric field effect in atomically thin carbon films". In: *Science* 306 (2004), pp. 666–669.

[42] C Lee, XD Wei, JW Kysar, and J Hone. "Measurement of the elastic properties and intrinsic strength of monolayer graphene". In: *Science* 321 (2008), pp. 385–388.

[43] AA Balandin, S Ghosh, WZ Bao, I Calizo, D Teweldebrhan, F Miao, and CN Lau. "Superior thermal conductivity of single-layer graphene". In: *Nano Letters* 8 (2008), pp. 902–907.

[44] YW Zhu, S Murali, MD Stoller, KJ Ganesh, WW Cai, PJ Ferreira, A Pirkle, RM Wallace, KA Cychosz, M Thommes, D Su, EA Stach, and RS Ruoff. "Carbon based super capacitors produced by activation of graphene". In: *Science* 332 (2011), pp. 1537–1541.

[45] T Nezakati, BG Cousins, and AM Seifalian. "Toxicology of chemically modified graphenebased materials for medical application". In: *Archives of Toxicology* 88 (2014), pp. 1987–2012.

[46] MW Hyer. "Analysis of failure of fiber reinforced polymer laminates". In: New York: McGraw-Hill, 1997, pp. 349–357.

[47] M Knops. "Stress analysis of fibre-reinforced composite materials". In: New York: Springer, 2008, pp. 2–12.

[48] S Eslam, AH Marwan, RT Mahmoud. "On and off-axis tension behavior of fibre reinforced polymer composites incorporating multi-walled carbon nanotubes". In: *Journal of Composite Materials* 46 (2011), pp. 1661–1675.

[49] L Iannucc. "Dynamic delamination modelling using interface elements". In: *Computers and Structures* 84 (2006), pp. 1029–1048.

[50] V Agubra, P Owuor, M Hosur. "Influence of nanoclay dispersion methods on the mechanical behaviour of E-Glass/Epoxy nanocomposites". In: *Nanomaterials* 2 (2013), pp. 550–563.

[51] JA King, DR Klimek, I Miskioglu, GM Odegard. "Mechanical properties of graphene nanoplatelet epoxy composites". In: *Journal of Applied Polymer Science* 128 (2013), 42174223.

[52] S Iijima. "Helical Microtubules of graphitic carbon". In: *Nature* 354 (1991), pp. 56–58.

[53] MK Hossain, M Hossain, MV Hosur, S Jeelani. "Flexural and compression response of woven E-glass/polyester-CNF nanophased composites". In: *Composites Part A* 42 (2011), pp. 1774–1782.

[54] J Qiu, C Zhang, B Wang, R Liang. "Carbon nanotube integrated multifunctional multiscale composites". In: *Nanotechnology* 18 (2007), pp. 1–11.

[55] BP Amoco Chemicals. *Typical Properties for Thornel Carbon Fibres- Standard Products*. Material Data. BP Amoco Chemicals, pp. 1–2.

[56] T Tian. *Anisotropic Thermal Property Measurement of Carbon-fiber/Epoxy Composite Materials*. PhD Thesis. University of Nebraska - Lincoln, 2011, pp. 1–155.

[57]   V Romanov, SV Lomov, Y Swolfs, S Orlova, L Gorbatikh, and I Verpoest. "Statistical analysis of real and simulated fibre arrangements in unidirectional composites". In: *Composites Science and Technology* 87 (2013), pp. 126–134.

[58]   CT Sun, RS Vaidya. "Prediction of composite properties from a representative volume element". In: *Composites Science and Technology* 56 (1996), pp. 171–179.

[59]   AR Maligno, NA Warrior, AC Long. "Effects of inter-fiber spacing on damage evolution in unidirectional (UD) fiber-reinforced composites". In: *European Journal of Mechanics - A/Solids* 28 (2009), pp. 768–776.

[60]   L Yang, Y Yan, Z Ran, Y Liu. "A new method for generating random fiber distributions for fiber reinforced composites". In: *Composites Science and Technology* 76 (2013), pp. 14–20.

[61]   M Romanowicz. "Numerical homogenization of fiber reinforced composites with complex microstructural features". In: *Journal of Theoretical And Applied Mechanics* 51 (2013), pp. 883–890.

[62]   R Hill. "Elastic properties of reinforced solids: Some theoretical principles". In: *Journal of the Mechanics and Physics of Solids* 11 (1963), pp. 357–372.

[63]   M Srinivasan, P Maettig, KW Glitza, B Sanny, A Schumacher, M Duhovic, and J Schuster. "Out of Plane Thermal Conductivity of Carbon Fiber Reinforced Composite Filled with Diamond Powder". In: *Open Journal of Composite Materials* 6 (2016), pp. 41–57. DOI: http://dx.doi.org/10.4236/ojcm.2016.62005.

[64]   M Srinivasan, P Maettig, KW Glitza, B Sanny, and A Schumacher. "Multiscale calculation for increasing the thermal conductivity of carbon fiber composite with diamond powder". In: Proceedings of XLII International Summer School Conference - Advanced Problems in Mechanics (APM 2014), pp. 481–490. DOI: 10.13140/RG.2.1.5035.8169.

[65]   AR Melro, PP Camanho, ST Pinho. "Generation of random distribution of fibers in long-fiber reinforced composites". In: *Composites Science and Technology* 68 (2008), pp. 2092–2102.

[66]   N.N. "Standard test method for thermal conductivity of solids by means of the guarded-comparative-longitudinal heat flow technique ASTM E 1225-04". In: (2013).

[67]   MJ Laubitz. *Axial Heat Flow Methods of Measuring Thermal Conductivity: Compendium of Thermophysical Property Measurement Methods Volume 1*. New York and London: Plenum Press, 1984.

[68]   J Schuster, D Heider, K Sharp, and M Glowania. "Thermal conductivities of three-dimensionally woven fabric composites". In: *Composites Science and Technology* 68 (2008), pp. 2085–2091.

[69]   J Schuster, D Heider, K Sharp, and M Glowania. "Measuring and modeling of thermal conductivities of three-dimensionally woven fabric composites". In: *Mechanics of Composite Materials* 45 (2009), pp. 165–174.

[70]   ST Tu, WZ Cai, Y Yin, and X Ling. "Numerical Simulation of Saturation Behavior of Physical Properties in Composites with Randomly Distributed Second-phase". In: *Journal of Composite Materials* 39 (2005), pp. 617–631.

[71]   W Wu, J Owino, A Al-Ostaz, and L Cai. "Applying Periodic Boundary Conditions in Finite Element Analysis". In: *SIMULIA Community Conference* (2014), pp. 707–719.

[72]   O van der Sluis, PJG Schreurs, WAM Brekelmans, HEH Meijer. "Overall behaviour of heterogeneous elastoviscoplastic materials: effect of microstructural modelling". In: *Mechanics of Materials* 32 (2000), pp. 449–462.

[73]   L Shuguang, A Wongsto. "Unit cells for micromechanical analyses of particle-reinforced composites". In: *Mechanics of Materials* 36 (2004), pp. 543–572.

[74]   S Daggumati, W Van Paepegem, J Degrieck, J Xu, SV Lomov, and I Verpoest. "Local damage in a 5-harness satin weave composite under static tension: Part II - Meso-FE modelling". In: *Composites Science and Technology* 70 (2010), pp. 1934–1941.

[75]   Y Arai. *Pitch-based carbon fiber with low modulus and high conduction*. Nippon Steel Technical Report No. 84. Nippon Graphite Fiber Corporation, 2001, pp. 12–17.

[76]   JP Hou, C Ruiz. "Measurement of the properties of woven CFRP T300/914 at different strain rates". In: *Composites Science and Technology* 60 (2000), pp. 2829–2834.

[77]   H Ullah, AR Harland, T Lucas, D Price, VV Silberschmidt. "Finite-element modelling of bending of CFRP laminates: Multiple delaminations". In: *Computational Materials Science* 52 (2012), pp. 147–156.

[78]   Z Hashin, A Rotem. "A Fatigue Failure Criterion for Fiber-Reinforced Composite Materials". In: *Journal of Composite Materials* 7 (1973), pp. 448–464.

[79]   Dassault Systemes Simulia Corp. *Abaqus Analysis User's Manual, Version 6.12*. Providence, RI: Dassault Systemes, 2012.

[80]   Y Gao, L Liu, and Z Zhang. "Mechanical performance of nano-CaCO3 filled polystyrene composites". In: *Acta Mechanica Solida Sinica* 22 (2009), 555–562.

[81]   MK Hossain, ME Hossain, MV Hosur, and S Jeelani. "Flexural and compression response of woven E-glass/polyester-CNF nanophased composites". In: *Composites: Part A* 42 (2011), 1774–1782.

[82]   I Ozsoy, A Demirkol, A Mimaroglu, U Huseyin, and D Zafer. "The influence of micro- and no-filler content on the mechanical properties of epoxy composites". In: *Journal of Mechanical Engineering* 61 (2015), 601–609.

[83] SA Rakha, RR Khan, AA Khurram, A Fayyaz, M Zakaullah, and A Munir. "Mechanical Properties of Epoxy Composites with Low Content of Diamond Particles". In: *Journal of Applied Polymer Science* 127 (2013), pp. 4079–4085.

[84] D Giugni. *ITK Local Support and Integration - Draft Report*. ATLAS Project Document. CERN, 2016. URL: {https://indico.cern.ch/event/546753/}.

[85] T Etter, M Papakyriacou, P Schulz, PJ Uggowitzer. "Physical properties of graphite /aluminium composites produced by gas pressure infiltration method". In: *Carbon* 41 (2003), pp. 1017–1024.

[86] KA Ament, MR Kessler, and M Akinc. "Cyanate ester-alumina nanoparticle suspensions: Effect of alumina concentration on viscosity and cure behavior". In: *Polymer Engineering & Science* 51 (2011), pp. 1409–1417.

[87] BJ Frame. "Characterization and Process Development of Cyanate Ester Resin Composites". In: *The Society for the Advancement of Material and Process Engineering, SAMPE* 44 (1999), pp. 2081–2094.

Appendix A

Thermal conductivity equation for an unknown sample

The following derivations were done by Prof. Jens Schuster and his colleagues at the Institute of Polymer Technology at the University of Applied Sciences, Kaiserslautern (Pirmasens). Some information can also be found in [69].

The measuring cell (Figure 115) is situated on a cool plate providing heat sink to maintain a constant bottom temperature by means of air convection. The heating power is calculated according to the possible maximum and minimum temperatures. Due to the design and material constraints, the maximum temperature should not exceed $70\,^\circ$C. The bottom temperature is permanently kept at $20\,^\circ$C by a cool plate (Figure 115). The height of the two bars ΔZ including the sample is about $250\,$mm.
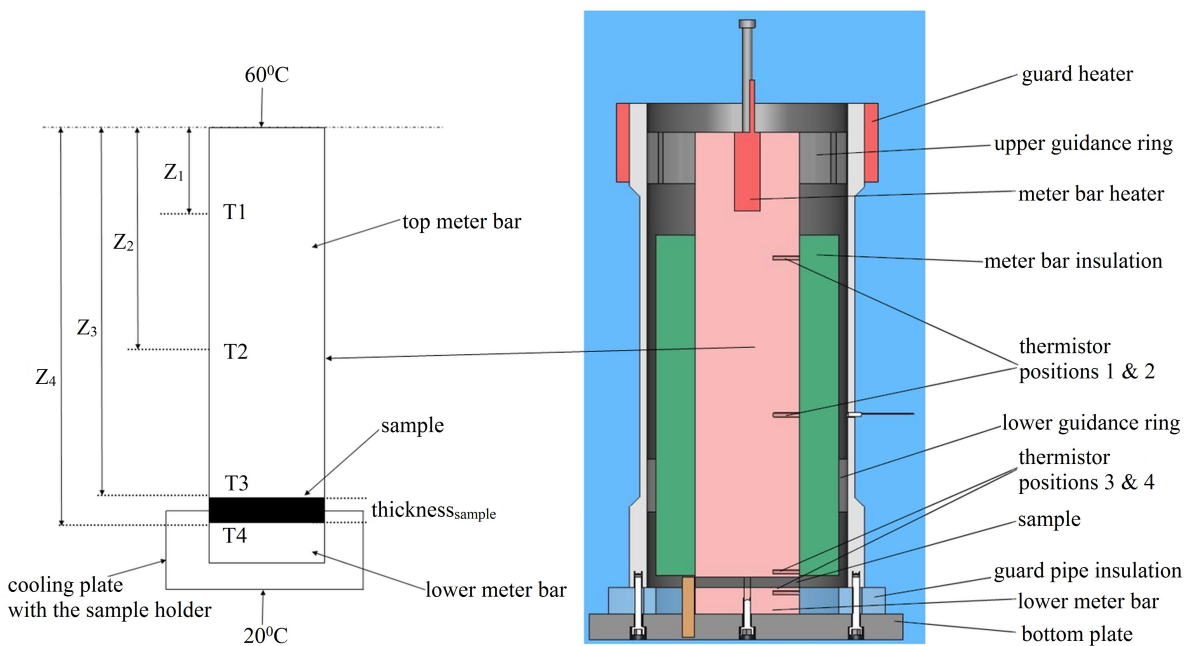

FIGURE 115: Measurement Setup with the Sample [63]

The thermal conductivity K_{bar} along the bars is assumed as $16.2\,\mathrm{W\,m^{-1}\,K^{-1}}$ and the active heater surface is about $3500\,\mathrm{mm^2}$. The heating power is calculated as shown in Equation A.1.

$$Q = K_{bar}\,A_{heater}\,\frac{\Delta T}{\Delta Z} \tag{A.1}$$

From Figure 115, a steady heat flux without losses due to the the guard heater in the top and lower meter bar is assumed as follows:

$$q_{top} = K_{bar}\,\frac{T_2 - T_1}{Z_2 - Z_1} \tag{A.2}$$

$$q_{lower} = K_{bar} \frac{T_4 - T_3}{Z_4 - Z_3} \tag{A.3}$$

The same heat fluxpass through the measuring zone which allows the following expression

$$q_{top} \approx q_{lower} \approx q_{measure} \tag{A.4}$$

In addition, the relationship between the thermal conductivities of the meter bars, the sample, and the thermal resistances of the interfaces R_{Int} are shown in Equation A.5.

$$R_{Int}^* = \left(\frac{Z_3 - Z_2}{K_{bar}} + \frac{Z_4 - Z_3}{K_{sample}} + R_{Int} \right) \tag{A.5}$$

R_{Int}^* has to be determined during a measurement with a reference sample and these are shown in Equation A.6

$$R_{Int}^* = \left(\frac{T_4 - T_3}{T_2 - T_1} \frac{Z_2 - Z_1}{K_{bar}} - \frac{thickness_{sample}}{K_{sample}} \right) \tag{A.6}$$

Finally, the thermal conductivity ($K_{sample} = K_{\perp Test}$) of an unknown calibrated sample is derived as

$$K_{sample} = \frac{thickness_{sample}}{\frac{T_4 - T_3}{T_2 - T_1} * \frac{Z_2 - Z_1}{K_{bar}} - R_{Int}^*} \tag{A.7}$$

Curriculum Vitae

Personal Details

Firstname, Lastname	Mukundan Srinivasan
Date of Birth	23.03.1986
Place of Birth	Chennai, India
Marital Status	Married

Education

Bachelor of Engineering **Mechanical Engineering**
08/2003 - 04/2007   Anna University, Chennai - India

Master of Science   **Automotive Engineering**
10/2007 - 02/2009   Birmingham City University, United Kingdom

Work Experience

Researcher   **Project**: Development of Lightweight Support Structure for the
University of Wuppertal   ATLAS Detector at the Large Hadron Collider
01/2013 - Till Date

Research Assistant   **Project**: Virtual Characterisation of Lamination Defects in a
IMDEA Materials   Wind Turbine Spar Cap
Madrid, Spain
12/2011 - 12/2012

Research Assistant   **Project**: Evaluation of the Fatigue Strength of Ti-6Al-4V
Politecnico Di Torino, Italy Notched Specimens
09/2010-09/2011

Research Assistant   **Project**: Dynamic Analysis of Viscoelastic Materials
Instituto Superior Tecnico,
Lisbon, Portugal
09/2009-11/2009

Lebenslauf

Persönliche Angaben

Vorname, Nachname	Mukundan Srinivasan
Geburtsdatum	23.03.1986
Geburtsort	Chennai, Indien
Familienstand	verheiratet

Ausbildungen

Bachelor of Engineering
08/2003 - 04/2007

Maschinenbau
Anna Universität, Chennai - Indien

Master of Science
10/2007 - 02/2009

Fahrzeugtechnik
Universität Birmingham City, Großbritannien

Berufserfahrungen

Wiss. Mitarbeiter
Bergische Universität
Wuppertal
01/2013-heute

Thema: Entwicklung von Leichtbauträgstrukturen für
den ATLAS Pixeldetektor am CERN

Forschungsassistant
IMDEA Materials
Madrid, Spanien

Thema: Verbundstoffen mit Laminierungsdefekten im
Holmgurt einer Windturbine

Forschungsassistant
Politecnico Di Torino, Italien
09/2010-09/2011

Thema: Bewertung der Ermüdungsfestigkeit von Ti-6Al-4V
gekerbten Prüfkörpern

Forschungsassistant
Instituto Superior Tecnico,
Lissabon, Portugal
09/2009-11/2009

Thema: Dynamische Analyse von viskoelastischen Materialien